Power Determination and Hydrino Product Characterization of Ultra-low Field Ignition of Hydrated Silver Shots

R. Mills[1,2], Y. Lu[1], R. Frazer[1]

[1]Brilliant Light Power, Inc., 493 Old Trenton Road, Cranbury, NJ 08512, USA

[2] Corresponding author

Abstract: Hydrated silver shots comprising a source of H and HOH catalyst were ignited by passing a low voltage, high current through the shot to produce explosive plasma that emitted brilliant light predominantly in the short-wavelength 10 to 300 nm region. Based on Stark broadening, the initially optically thick essentially 100% ionized plasma expanded at sound speed or greater and thinned to emit EUV and UV light. The peak power of 20 MW was measured using absolute spectroscopy over the 22.8-647 nm region wherein the optical emission energy was 250 times the applied energy. Synchronized high-speed video and spectroscopic recording of the plasma emission and the measurement of the applied ignition power over time showed that plasma persisted even after the ignition power decayed to zero. Continuous megawatt-level power was recorded on a hydrino reactor wherein continuous brilliant plasma was maintained by HOH and H produced from water-entrained injected molten silver matrix. The molten fuel produced the same EUV spectrum as the shots, but converted to 5700K blackbody radiation of about 1 m^2 surface area with a positive feedback cycle of silver vaporization and absorption of the hydrino reaction emission with the plasma becoming increasingly optically thick. The calorimetrically measured power of a typical 80 mg, 10 microliter shot ignition released by the nascent HOH catalyzed transition of H to hydrino state $H_2(1/4)$ was 400,000 W. Based on the shockwave propagation velocity and the corresponding pressure, the high-current ignition of water in a silver matrix was measured to produce a shock wave that was equivalent to about 10 times more moles of gunpowder. The catalysis reaction product $H_2\left(1/4\right)$ was identified by Raman spectroscopy, photoluminescence emission spectroscopy, X-ray photoelectron spectroscopy, and MAS ^1H NMR.

1 Introduction

Atomic hydrogen is predicted to form fractional Rydberg energy states $H(1/p)$ called "hydrino atoms" wherein $n = \frac{1}{2}, \frac{1}{3}, \frac{1}{4}, ..., \frac{1}{p}$ ($p \le 137$ is an integer) replaces the well-known parameter $n = \text{integer}$ in the Rydberg equation for hydrogen excited states. The transition of H to a stable hydrino state $H\left[\frac{a_H}{p = m+1}\right]$ having a binding energy of $p^2 \cdot 13.6\ eV$ occurs by a nonradiative resonance energy transfer of $m \cdot 27.2\ eV$ (m is an integer) to a matched energy acceptor [1]. The nascent H_2O molecule (not hydrogen bonded in solid, liquid, or gaseous state) may serve as a catalyst by accepting 81.6 eV (m = 3) to form an intermediate that decays with the emission of a continuum band with a short wavelength cutoff of 10.1 nm and energy of 122.4 eV [1-7]. The continuum radiation band at 10.1 nm and going to longer wavelengths for theoretically predicted transitions of H to lower-energy, so called "hydrino" state H(1/4), was observed only arising from pulsed pinch gas discharges comprising some hydrogen first at BlackLight Power, Inc. (BLP) and reproduced at the Harvard Center for Astrophysics (CfA) by P. Cheimets and P. Daigneau [6, 7]. The source was determined to be due to the HOH catalyzed transition of H to the lower-energy hydrogen or hydrino state H(1/4) [7].

Solid fuels that form HOH catalyst and H showed multiple times the maximum theoretical energy [8]. Excess heats from solid fuels reactions were measured using water-flow calorimetry and these results have been independently confirmed by differential scanning calorimetry (DSC) runs at testing laboratories. The predicted molecular hydrino $H_2(1/4)$ was identified as a product of power producing cells, CIHT cells and thermal cells, by techniques such as MAS ^1H NMR, electron-beam excitation emission spectroscopy, Raman spectroscopy, Raman spectroscopy with surface enhanced Raman scattering (SERS), time-of-flight secondary ion mass spectroscopy (ToF-SIMS), electrospray ionization time-of-flight mass spectroscopy (ESI-ToFMS), Fourier transform infrared (FTIR) spectroscopy, X-ray photoelectron spectroscopy (XPS), and photoluminescence emission spectroscopy [8-11].

Based on the catalyst mechanism, high current was predicted to facilitate a rapid hydrino transition rate (higher kinetics) by recombining charges that cause an inhibiting space charge build up from the ionization of the HOH catalyst. The application of a high current to a conductive matrix having a source of catalyst such as HOH to react with supplied H was shown to form a low-voltage arc current to dissipate space charge from the hydrino reaction to support high kinetics [7,9]. It was shown previously that the kinetics of catalysis of H to H(1/4) by HOH catalyst was explosive when a high current such as 10,000-25,000 A was flowed through a solid fuel [7,9] comprising a source of H and HOH embedded in a highly conductive matrix. The resulting brilliant light-emitting expanding plasma was predicted to emit EUV continuum radiation emission with short wavelength cutoffs and energies of $m^2 \cdot 13.6\ \text{eV}\ \left(\frac{91.2}{m^2}\ \text{nm}\right)$ when it was expanded into a vacuum chamber such that its atmospheric pressure was dissipated sufficiently to overcome the optical thickness. Such a light source at once overcame any alternative mechanism of the EUV continuum emission such as being due to a high electric field creating highly-charged ions since the voltage of the ignition current source had an applied AC peak voltage of under 15 V. Moreover, chemical reactions are not capable of more than a few eVs,

whereas, the continuum radiation extended to 122.4 eV. Due to the optical thickness of elements in the plasma, ion emission lines were observed as expected on a continuum radiation background due to continuum absorption and reemission as ion spectral lines. Based on a spectroscopically measured Stark line broadening, during a phase of the ignition event, the H_2O-based fuel ignition produced brilliant light-emitting plasma, an essentially fully ionized gaseous physical state of the fuel comprising essentially positive ions and free electrons. The blackbody temperature the ignition plasma was as high as that of the Sun, 5700 K. The explosive plasma was shown to expand at sound speed or greater to become optically thin with a transparency to short wavelength light to 10.1 nm (122.4 eV), about 10 times the maximum photon energy possible from the ignition source's applied voltage and having measured optical emission energy of 250 times the applied energy. Considering the elimination of field acceleration energy as well as a chemical source, the mechanism of the selective high-energy continuum radiation with a 122.4 eV cutoff was assigned to the H to H(1/4) hydrino transition catalyzed by HOH.

In addition to HOH, as predicted, mH atoms acting as a catalyst was previously evidenced by the observation of EUV radiation from a solid fuel comprising a highly conductive material and a source of hydrogen such as a hydrocarbon through which a low voltage, high current was flowed [7]. Ion emission lines were also observed as expected on a continuum radiation background due to continuum absorption and reemission as spectral lines as in the case of HOH catalyst. The same mechanism applies to H pinch plasma emission and to astrophysical H plasma sources [7]. Specifically, mH catalyst was identified to be active in astronomical sources such as the Sun, stars, and interstellar medium wherein the characteristics of hydrino product match those of the dark matter of the universe [7]. The EUV continuum results offer resolution to many otherwise inexplicable celestial observations with (a) the energy and radiation from the hydrino transitions being the source of extraordinary temperatures and power regarding the solar corona problem, the cause of sunspots and other solar activity, and why the Sun emits X-rays [4,7], (b) the hydrino-transition radiation being the radiation source heating the WHIM and behind the observation that diffuse Hα emission is ubiquitous throughout the Galaxy requiring widespread sources of flux shortward of 912 Å, and (c) the identity of dark matter being hydrinos [7].

In this study, HOH catalyst was further shown to give EUV radiation of the same nature by igniting hydrated silver shots comprising a source of H and HOH catalyst by passing a low voltage, high current through the shot to produce explosive plasma that emitted brilliant light predominantly in the short-wavelength 10 to 300 nm region. The power and energy of the light released from the shot ignition event were determined using absolute spectroscopy over the 22.8-647 nm region using a grazing incidence EUV spectrometer (GIS), normal incidence EUV spectrometer (NIS), and a ultraviolet-visible (UV-Vis) spectrometer wherein the UV-Vis spectrometer was absolutely calibrated using a NIST traceable tungsten lamp and a NIST traceable deuterium lamp. The intensity calibration was extended to the EUV wavelengths by spectral overlap with calibrated regions and the spectral responses of the spectrometers. Molten silver was dripped into ignition electrodes to form silver vapor plasma that became increasingly optically thick to the hydrino EUV radiation wherein the EUV absorption further vaporized the silver that in turn increased the EUV radiation absorption in a positive feedback loop to create a 5700 K blackbody radiator. The EUV spectrum of the optically thin plasma of the

hydrated molten silver and the blackbody temperature of the optically thick silver vapor over time were measured with a normal incidence EUV spectrometer and a UV-Vis spectrometer, respectively. The optical power was confirmed using a commercial bomb calorimeter. The potential of a novel detonation mechanism whereby the extraordinary power released as extreme ultraviolet radiation couples with air to form a shockwave was tested by sound propagation velocity and pressure measurements. Furthermore, the predicted molecular hydrino $H_2(1/4)$ was identified as a product of the hydrated silver ignition by Raman spectroscopy, photoluminescence emission spectroscopy, X-ray photoelectron spectroscopy, and MAS ^1H NMR.

2 Experimental Method

Spherical silver shots containing H_2O were prepared by melting silver sheet in the presence of bulk water using a tungsten inert gas (TIG) welder. Silver foil (0.5 mm thick Alpha Aesar 99.99%) was cut into squares weighing about 80 mg each. Each piece was placed in a 3 mm deep half spherical depression in a 3 cm thick graphite sheet that was filled with distilled water. In the absence of argon shield gas, a TIG welder (Miller Syncrowave 250, Serial No. KK001661) was operated in air at 30 A and 12 V to melt each silver foil piece to cause small amounts of water to be encapsulated in the resulting spherical shot. Silver-H_2O shots weighing between 67 mg and 85 mg were selected for spectroscopic studies. Alternatively, silver shots of about 1.5 mm radius, weighing about 80-90 mg were formed by dripping molten silver through a 1 mm diameter dripper into distilled water maintained at room temperature. The shots were retrieved and agitated to remove excess water, but were not dried. In both cases, the water content was determined by weighing about 10 g of shot, before and after melting in the glove box to remove the water content which as determined to be about 1 mol% H20. Spectroscopic, optical and thermal power, and analytical studies were performed on the shots. The performances of the shots made by the two methods were comparable. In addition, spectroscopy and plasma characterization of molten silver with water injected or added in the form of an ambient atmosphere were performed to compare with the results from the shots.

2.1 Absolute Power Spectrum of Ignited Hydrated Silver Shots

Schematics of the light source comprising hydrated silver shot ignited with a spot welder, the intensity reducing, evacuated light conduit, each of the three spectrometers to cover the spectral wavelength range of 10 nm to 815 nm, and the deuterium and W-halogen calibration lamps are shown in Figures 1A-K. The absolute spectral irradiance calibration was performed on a UV-Vis Mightex system spectrometer using a NIST traceable deuterium lamp and a NIST traceable quartz tungsten halogen lamp to cover the region 200-2400 nm [12]. The Mightex system comprised (i) a Horiba MicroHR f/3.9 imaging spectrometer (Model: MHR-MS; Horiba 140 mm Czerny-Turner spectrograph) with a fixed slit width of 25 μm and a fixed height of 1 mm, a single grating mount (Model: MHR-SGM), and a 150 g/mm ruled grating blazed at 500 nm (Model: 510-49-X36), (ii) a Mightex buffered and triggerable USB 2.0 CCD linescan camera (Model: TCE-1024-UF) with 1024 pixels of 14 x 14 um size per pixel, spectral range from 200 to 1000 nm, 8 bit ADC at 25 kFPS, and 40 µs minimum exposure time, and (iii) a MgF_2 window (7 mm diameter, 2 mm thickness) on the entrance to the spectrometer and a fused silica window on the entrance of the camera. Calibration spectra for both lamps were acquired

based on the instructions provided by the lamp manufacturers. A calibrated 30 W deuterium lamp (Gooch & Housego, model OL UV-40, S/N 1028, having a calibration date of August 25, 2016, a certification date of August 29, 2016, and 7 working hours with a calibration lifetime of 50 hours) comprising a NIST traceable standard spectral irradiance source was used to calibrate the wavelength region 200-400 nm. The deuterium lamp was powered by a Gooch & Housego OL 46D deuterium power supply 300 mA +/- 0.1%. The distance from deuterium lamp flat window to spectrometer slit was 30 cm. The Mightex camera acquisition software was set to acquire 10 spectra, each having an exposure time of 650 ms. The data of the 10 spectra was added to form one spectrum with total exposure time of 6.5 s. Dark spectra were acquired with same settings as those for deuterium lamp spectra.

The deuterium lamp determined instrument response function of the Mightex absolute irradiance calibration was extended to 2400 nm using a 1000 W calibrated quartz tungsten lamp (QTH) (Newport, model 63350) comprising a NIST traceable standard source over wavelength 250-2400 nm. Tungsten lamp spectra were acquired at a distance of 50 cm between lamp center and the spectrometer slit. The Mightex camera acquisition software was set to acquire 10 spectra, each having an exposure time of 8 ms. The data of the 10 spectra was added to form one spectrum with total exposure time of 80 ms. Dark spectra were acquired with same settings as those for QTH lamp spectra.

The spectrometer instrument response function C_p was obtained by the formula:

$$C_p = SI\frac{\left(ATdL\right)}{\left(S-D\right)} \tag{1}$$

where SI is the lamp standard irradiance data, A is the spectrometer entrance slit area given by the product of the slit height and width, T is exposure time, dL is the wavelength interval between two adjacent data points, S is the lamp spectrum intensity counts, and D is the dark counts.

The shots were singly fired in a vacuum chamber (14.6 cm diameter X 28 cm length) with a windowless connection to the vacuum tube (3.5 cm ID) that was either connected to the GIS, the NIS (EUV wavelengths), or a MgF_2 window (7 mm diameter, 2 mm thickness) that was incident to the entrance optics of the NIS (UV-Vis wavelengths) or the Mightex spectrometer. The chamber and tube were evacuated to 1 X 10^{-3} Torr (NIS and UV-Vis) or 5 X 10^{-4} Torr (GIS) as different spectral regions were acquired. When the MgF_2 window was absent, the EUV spectrometers were differential pumped to 1 X 10^{-6} Torr in order to record the EUV wavelengths. Each shot was confined between the two copper electrodes of a spot welder (Taylor-Winfield model ND-24-75 spot welder, 75 KVA, 15 PSI applied electrode pressure, pressure time setting 20, heat time setting 1 cycle, 1 pulse count, interrupted, impulse mode, heat control 100%, tap 8) wherein the electrodes penetrated the vacuum chamber at vacuum-sealed, electrically insulating penetrations. The horizontal plane of the sample was aligned with the optics of each spectrometer as confirmed by an alignment laser. Each sample was subjected to a short burst of low voltage, high current electrical energy. The applied 60 Hz AC voltage was less than 15 V and the peak current was about 23,000-25,000 A. The high current caused the sample to ignite as brilliant light-emitting expanding plasma of near atmospheric pressure. To cause the plasma to become optically thin such that EUV light could emerge, the ignition occurred in the 4.7 liter vacuum chamber that housed the ignited sample.

The shot light emission was introduced to a UV-Vis Mightex system spectrometer for spectral measurement of the wavelength region 200-815.4 nm that was calibrated with a NIST traceable deuterium lamp and a NIST traceable quartz tungsten halogen lamp. The Mightex was triggered by a 30 us duration 5V signal generated by an Agilent 33220A 20 MHz Arbitrary Waveform Generator when a gating signal generated by a Picoscope 5442B digital oscilloscope was issued when current began to flow above a threshold in the welder as measured by a Rogowski current probe (Model: PEM LFR15/150/700). The parameters during acquisition and data processing for the UV-Vis Mightex system spectrometer were: the Horiba spectrometer center was 500 nm, the slit width was 25 μm, the slit height was 1 mm, the exposure time was 40 us, the frame rate was 25,000 frames/s (FPS) wherein 2000 frames were acquired over an 80 ms acquisition time, the evacuated path distance from the silver shot to the MgF_2 window was 2.11 m, the light exited the window to travel 0.08 m in air to the Mightex slits such that the total distance from the shot to the slits was 2.19 m, and the absolute irradiance integration range was 200-815.4 nm. The spectra were wavelength calibrated using emission lines generated by a mercury argon wavelength calibration source (Model: Ocean Optics HG-1) in the 200-800 nm wavelength range.

The shot light emission was introduced to a normal incident EUV spectrometer for spectral measurement of the wavelength region covered by the monochromator of 30-650 nm. The spectrometer was a McPherson 0.2 meter monochromator (Model 302, Seya-Namioka type) equipped with a 300 g/mm Al-MgF_2 coated grating. The EUV light was detected by the Andor iDus CCD camera. The slits were set at less than 1 μm. The vacuum inside the monochromator was maintained below 1 X 10^{-6} Torr by a turbo pump. The evacuated distance from the shot to the slits was 1.9 m. The calibration of the spectral intensity was obtained by matching the intensity in regions of wavelength overlap (208 to 647 nm) with the spectrum of a UV-Vis spectrometer that was calibrated with a NIST traceable deuterium lamp and a NIST traceable quartz tungsten halogen lamp.

The EUV spectrum (5-65 nm) was recorded using a McPherson grazing incidence EUV spectrometer (Model 248/310G) equipped with a 600 g/mm gold coated grating. The angle of incidence was 87°. The wavelength resolution with an entrance slit width of 200 μm was about 0.3 nm at the CCD center and 0.7 nm at the limits of the CCD wavelength range window of 50 nm. A 150 nm thick aluminum filter (Luxel Corporation) was placed between the grating and CCD detector and a 650 nm aluminum filter was placed in front of the entrance slit to block the visible light and to prevent damage to the spectrometer from the blast debris. The transmittance of the Al filter has a transmission window between 17 nm to 80 nm as shown in Figures 2A-B [13]. To measure to the 10.1 nm short wavelength cutoff of the H(1/4) transition continuum radiation while selectively blocking visible light, a 150 nm thick Zr filter (Luxel Corporation) was placed in the light path between the grating and CCD detector. The transmittance of the Zr filter has a transmission window in the region of 10 nm as shown in Figure 2C [13]. The evacuated distance from the shot to the slits was 1.69 m. The EUV light was detected by a CCD detector (Andor iDus) cooled to -60 °C. The CCD detector was centered at 25 nm and 55 nm to cover the wavelength region of 0-65 nm. Known oxygen and nitrogen ion lines observed in a high voltage pulse discharge spectrum were used to calibrate the wavelengths of the 0 to 65 nm region prior to recording the shot blast spectrum.

As discussed in Section 3.1, matching the intensities at overlapping spectral wavelengths was used to join the corrected spectra wherein the Mightex UV-Vis spectral results were used to scale the GIS-NIS combined spectrum to achieve a match in the spectral overlap region. The integrated power of the Mightex spectrum was determined over the wavelength region 208-647 nm. The GIS-NIS spectrum was scaled such that the integrate power in the 208-647 nm region matched that of the Mightex spectrum. The total power over the full wavelength range of 22.8-647 nm was integrated on the combined spectrum.

Specifically, the GIS spectra were corrected for the Al and Zr filter [13] curves shown in Figure 2A-C as well as for the grating efficiency. The NIS data was corrected by the MgF_2 window attenuation using data with and without the widow. The NIS spectra were further corrected by the reflectance curve of the Al-MgF_2 coated grating. The UV-Vis spectrum recorded over 200 nm to 815 nm region with the Mightex UV-Vis spectrometer using the MgF_2 window was corrected for the MgF_2 window transmission curve by dividing the data by the transmission efficiency of the window, and the spectrum was absolutely calibrated. The combined GIS and NIS count intensity spectra following filter, grating, and CCD quantum efficiency corrections was converted to energy density by multiplying the counts as a function of wavelength by the conversion factor $\frac{hc}{\lambda}$. The combined GIS and NIS energy density spectrum was power calibrated against the absolutely calibrated UV-Vis spectrum. The UV-Vis spectral results were used to scale the GIS-NIS combined spectrum to achieve a match in the spectral overlap region. The integrated power of the Mightex spectrum was determined over the wavelength region 208-647 nm. The GIS-NIS spectrum was scaled such that the integrate power in the 208-647 nm region matched that of the Mightex spectrum. The total power over the full wavelength range of 22.8-647 nm was integrated on the combined spectrum.

The splicing or stitching of the absolutely calibrated Mightex spectrum to the NIS and GIS spectra as a means to absolutely calibrate the EUV wavelength regions was confirmed by comparing the response of the Mightex and NIS to an intense deuterium lamp. Spectra were acquired on Mightex and NIS spectrometers using a Hamamatsu L7293 D_2 lamp having an MgF_2 window wherein the absolute irradiance of the L7293 D_2 lamp powered by a Hamamatsu C1518, 2.5 V power supply was obtained by using the Mightex spectral response as the absolute calibration standard over the region of wavelengths common to both spectrometers. The Mightex spectrum was acquired using the same system parameters as used for the determination of the optical power. The NIS spectrum was acquired in vacuum using a 1.6 cm Swagelok connector with Teflon ferrule. The NIS spectrum was acquired using the same system parameters as used for the determination of the optical power except that the distance from deuterium lamp housing aperture to spectrometer slit was 31.7 cm rather than 32.7 cm.

The current and voltage traces as a function of time were recorded at a time resolution of 56 ns via 60 MHz digital oscilloscope (Picotech, Picoscope 5442B) using a voltage and current probe. The voltage was measured by a 25 MHz 70 V 10:1 differential voltage probe (Picotech, model TA041) accurate to +/-2% and the current was measured with a Rogowski coil (PEM, LFR 15/150/700) that was accurate to +/-0.3%. The relationship of the light emission to the current and voltage of the ignition power source was studied to determine the real power into the shot. Specifically, other effects such as reactance of the ignition circuit due to

the effect of the blast and the nature of an observed voltage spike that was very substantially more than the maximum rated ignition source voltage was studied using an EUV photodiode and an independent, laboratory grounded antenna placed 20 cm from the shot. The latter experiment resolved the nature of the abnormal voltage spike by determining it to be due to plasma driven electromagnetic pulse (Section 3.1).

The temporal evolution of plasma light emitted by the shot was measured with a photodiode (Thorlabs, model SM05PD1A) having a spectral range of 350-1100 nm, a peak sensitive wavelength of 980 nm, an active area of 13 mm^2, a rise/fall time of 10 ns, and a junction capacitance of 24 pF at 20 V. The signal was processed using an amplifier (Opto Diode model PA 100) with no gain and a 10 V bias and recorded with a 60 MHz scope (Pico Technology, Picoscope 5442B) at a scan interval of 25 ns. The measuring distance was 100 cm.

An independent, laboratory grounded antenna comprising a 2.5 cm diameter copper disc coated with a 1 mm thick Teflon tape coating, mounted on a plastic support was placed at distances of 10 cm and 20 cm from the shot inside of the blast vacuum chamber, and the voltage was recorded using the differential voltage probe.

To reduce the effect of an observed electromagnetic pulse created by the blast, the applied voltage across the shot and the corresponding applied power and energy were measured on the shot-loaded ignition circuit external to the chamber by recording the total circuit current and the current of a circuit parallel to the shot of known constant resistance. The voltage applied to the shot was the same as the parallel voltage across the shunt that was given by the product of the measured shunt current and shunt resistance. The shot current was given by the difference in the measured total current and the shunt current. The applied shot power was given by the product of the shot voltage and shot current. The very reproducible applied shot energy was given by the integral of the applied shot power. The analysis is given in Section 3.1.

The shunt comprised a copper strip having resistance of 1.21 $m\Omega$. It was selected such that the majority of the current flowed through the shot such that the shunt resistance remained constant wherein the constancy of the resistance was confirmed by measuring the resistance before and after the blast with a precision micro-ohmmeter. Both currents were measured using two identical Rogowski coils (Model CWT600LF with a 700 mm cable; accurate to 0.3%) that were matched and calibrated using the Acme 75 KVA welder that served as the AC power supply with both sensing the identical current.

2.2 Balmer α Line Broadening Measurements

The width of the 656.3 nm Balmer α line emitted from plasmas of ignited hydrated silver shots was recorded to determine the electron density. The plasma emission was fiber-optically coupled to a Jobin Yvon Horiba 1250 M spectrometer through a high quality UV (200-800 nm) fiber-optic cable. The spectrometer had a 1250 mm focal length with a 2400 g/mm grating and a detector comprising a Symphony model, liquid-nitrogen cooled, back illuminated 2048 × 512 CCD array with an element size of 13.5 μm × 13.5 μm. The spectrometer resolution was 0.37 Å determined by using the deuterium lamp with the entrance and exit slits set to 20 μm. Due to the broader acquisition range and the shift of the spectrum due to the Stark effect, the Balmer α line width was also recorded with an Ocean Optics visible spectrometer. The visible spectrum over the wavelength region of 350 nm to 1000 nm was recorded during the blast event using an Ocean Optics visible

spectrometer coupled with a fiber optic cable (Ocean Optics Jaz, with ILx511b detector, OFLV-3 filter, L2 lens, 5 μm slit, 350–1000 nm). The resolution determined by using the 632.8 nm HeNe laser line was 12.9 Å.

2.3 High speed video, current, voltage, and spectroscopic measurement of ignited hydrated silver shots

The plasma emission of the of hydrated silver shots was synchronously video and spectroscopically recorded at 17,791 frames per second and at 40 μs time resolution with the corresponding voltage and current waveforms as a function of time to determine the relationship of the optical power output from the ignited shot and the input power under an Ar/H_2(5%) atmosphere. The camera used was a Color Edgertronic. The current and voltage traces as a function of time were recorded at a time resolution of 56 ns by the 60 MHz digital oscilloscope (Picotech, Picoscope 5442B) using a voltage and current probe with the Picotech differential voltage probe and the Rogowski coil. Plasma power having an extraordinarily high temperature blackbody radiation with no electrical input power and no chemical reaction possible proves the existence of a new energy source as further shown by EUV spectroscopy (Sec. 3.1) and analytical characterization of the plasma product to be the due to the reaction H to H(1/4) [1,8-11] (Sec. 3.7).

2.4 Spectrum of Continuous Molten Silver Injection to Compare with that of Ignited Hydrated Silver Shots

The UV emission of the plasma produced in a vacuum chamber by continuous injection of hydrated molten silver was recorded in order to compare the emission with that from the ignition of single shots as given in Section 3.1. Specifically, the UV spectral emission was recorded while continuously dripping hydrated molten silver into tungsten electrodes powered by capacitors to deliver a low voltage, high ignition current. The light source shown in Figures 3A-F comprised a T-shaped vacuum chamber housing a 2.54 cm diameter, 100 cm^3 quartz dripper with 1 mm nozzle hole that dripped molten silver into the 3 mm gap between W electrodes of an electrode assembly angled at 45° relative to the vertical axis of the dripper. Water vapor was supplied to the dripping silver through a nozzle at the ignition site. The water vapor pressure was estimated to comprise 1 Torr locally and 10 mTorr in the chamber. The electrode assembly comprised an electromagnetic (EM) pump to force the silver through by a Lorentz force. The Lorentz force was created by the inter-electrode current and the crossed magnetic field provided by magnets. The magnets of the EM pump comprises 3.8 cm x 3.8 cm x 3.8 cm neodymium permanent magnets at opposite ends of a channel 5 cm long channel lined by an upper W plates that formed a funnel to lower W plates oriented along the vertical axis to form a 3 mm wide electrode gap into which the molten silver dripped (Figure 3F). The 3 mm thick upper funnel W electrodes were mounted 0.5 cm thick copper plates planed at a 45° angle to form the funnel to the lower channel of 5 mm high, 2 cm long, 3.1 mm thick W electrodes. The silver was melted by an 8 kW RMS maximum power inductively couple heater (30-80 kHz, WH-VI-16, Zhengzhou Gou's Electromagnetic Induction Heating Equipment Co. Ltd). The water cooled, radio frequency (RF) antenna comprised 6.35 mm ID copper tubing that penetrated the vacuum chamber at RF feed throughs mounted in a 2.54 cm thick Plexiglas plate fasted to a flange. The antenna was coiled around the silver dripper. The source of electrical power for ignition when the molten silver dripped into the electrodes to complete the electrical circuit comprised two parallel pairs of 4 capacitors in series (Maxwell

Technologies K2 Ultracapacitor 2.85V/3400F) to provide about 11.4 V/6800 F and about 4 kA to 10 kA. The current was carried from the capacitor bank to the electrodes by 2 cm diameter copper bus bars that penetrated the vacuum chamber with feed throughs. The EUV spectrum was recorded with a trigger current of 3 kA.

The spectrometer was a normal incidence McPherson 0.2 meter monochromator (Model 302, Seya-Namioka type) equipped with a 300 g/mm Al-MgF_2 coated grating. The EUV light was detected by the Andor iDus 420 CCD camera. The slits were set at ~100 μm. The vacuum inside the monochromator was maintained below 1 x 10^{-6} Torr by a turbo pump. The evacuated distance from the shot to the slits was 57.2 cm. The light passed through a MgF_2 window that cut the radiation below 120 nm. The scan time was 2 ms.

Using an experimental setup similar to that shown in Figures 3A-F, but housed in a glove box, molten silver was also continuously dripped into the tungsten electrode assembly that was oriented perpendicularly to the silver drip direction and run under an Ar/H_2(3%) atmosphere with addition of 1 Torr ambient water vapor rather than addition of 1 mol% water in the molten silver. In this case, the plasma was operated long enough in duration to permit the silver to boil to form optically thick plasma that absorbed the EUV and UV light. The emission was introduced to a UV-Vis Mightex system spectrometer for spectral measurement of the wavelength region 200-815.4 nm. The spectrometer was mounted under the electrode assembly at a distance of 40 cm along an axis at 45° from the vertical electrode centerline. The entrance slit was 2 mm wide by 1 mm high, the exposure time was 40 μs, the windows were sapphire (2 mm thick) to the spectrometer system, MgF_2 (7 mm diameter, 2 mm thickness) on the entrance to the spectrometer, and a fused silica on the entrance of the camera.

2.5 Bomb Calorimetry of Ignited Hydrated Silver Shots

The energy balances were measured on the 60-80 mg hydrated silver shots. The copper electrodes without hydrated silver shot served as the calibration control to determine the calorimeter heat capacity. The cell gas comprised Ar/H_2(3%) at one atmosphere wherein the cell was purged for 5 minutes at a flow rate of 4800 sccm.

The setup of the Parr 1341 calorimeter used for the energy balance determination (Figure 4) comprised an unmodified calorimeter jacket (21) and calorimeter cover (1) (combined Parr part number A1100DD) [14]. A thermistor with a temperature resolution of 0.001 ^oC (2) (Parr part number 1168E2) passed through the calorimeter cover and was secured such that it read the water temperature in line with the bomb assembly at a distance of 2.54 cm from the bottom of the water bucket (19). The custom made, 0.051 cm thick stainless steel oval bucket weighed 417.8 g and had a small diameter of 12.7 cm inches, a large diameter of 18.4 cm, and a height of 10.2 cm. The water bucket held 1225±.01 g of deionized water along with the custom calorimeter bomb assembly. A stirring assembly (6) comprised a stirrer pulley (Parr part number 37C2), a stirrer bearing assembly (Parr part number A27A), and stirrer shaft with impeller (11) (Parr part number A30A3). It was mounted on the calorimeter cover and was connected to the motor assembly (Parr part number A50MEB) by a motor pulley (8) (Parr part number 36M4) by a stirrer drive belt (7) (Parr part number 37M2) driven by the motor (9). The motor assembly was attached to the calorimeter externally by an L-bracket motor connector (10) to prevent the heat output of the motor from affecting the calorimetric measurements. Two 1.6 cm OD silver-plated, hollow copper electrodes (3) passed through customized holes in the calorimeter cover and further

passed through a Teflon position stabilizing block and then connected to the main conductors of an ACME 75 kVA resistance welder. The 0.32 cm thick stainless steel custom cylindrical bomb cell (14) had a 7.62 cm diameter and 2.54 cm height with a 12.4 cm flange that was 0.64 cm thick. The electrodes penetrated the flange lid through electrode feed-throughs (13) with Teflon insulating ferrule seals (15) that provided electrical isolation and a hermetic seal. Power was transmitted to the hydrated silver shot (18) with or without the 1.3 cm diameter 0.48 cm thick copper fastener swivel (17) by the 3.0 cm long, 0.95 cm diameter copper sample-fastening bolts (16) which were threaded through the base of the electrodes. The hydrated silver shot was contained between the fastener swivels by tightening the sample fastening bolts to a torque of approximately 1.81 Nm as measured by a high accuracy flat beam torque wrench resulting in approximately 1112 N force to the sample as measured by a piezoresistive force sensor (Measurement Specialties, FC2311-0000-0250-L). Efficient heat transfer was enabled by heat fins (12) installed on the electrodes immediately above the electrode feed-throughs that ensured minimal heat loss through the electrodes and out of the closed system. The bucket stand (20) elevated the bomb cell to the top of the calorimeter to minimize the dimensions and quantities of materials necessary to operate the Parr 1341 calorimeter and improve the accuracy of the measurements.

Each hydrated silver shot was ignited with an applied peak 60 Hz voltage of less than 15 V and a peak current of about 22,000 A. The input power was recorded through a custom interface receiving input from the positive probe connector (4) and negative probe connector (5). The voltage was measured by a data acquisition system (DAS) comprising a PC with a National Instruments USB-6210 data acquisition module and Labview VI. The current was also measured by the same DAS using a Rogowski coil (Model LFR15/150/700) that was accurate to $\pm$0.3% as the signal source. V and I input data were obtained at 83 KS/s and a voltage attenuator was used to bring analog input voltage to within the +/-10V range of the USB-6210.

The VI waveform was 60 Hz sinusoidal to the time of ignition in the second half of the sinusoidal cycle. An EMP was produced at the time point of ignition causing the voltage to be erroneous during the blast event. To reduce the effect of the observed EMP created by the blast, the applied voltage across the shot circuit and the corresponding applied power and energy were measured on the shot-loaded ignition circuit external to the calorimeter by recording the total circuit current and the current of a circuit parallel to the shot circuit of known constant resistance (Section 2.1). The voltage applied to the shot was the same as the parallel voltage across the shunt that was given by the product of the measured shunt current and shunt resistance. The shot current was given by the difference in the measured total current and the shunt current. The applied shot power was given by the product of the shot voltage and shot current. The applied shot energy was given by the integral of the applied shot power. The product of the shunt voltage and the total current total gave the calorimeter input power. The calorimeter input energy was given by the integral of the calorimeter power. The ignition circuit comprised a rigidly fixed gap filled by the shot wherein the circuit was broken during the second half of the sinusoidal cycle by the blast event. The directly measured VI product matched that of the shunt voltage and total current product to the point of the ignition. The results of the external measurements of the input energy during the blast event of 20 J were very repeatable such that the 20 J was used for the input energy during the blast that was added to the integral of the voltage and current for the non-blast portion of the VI waveform. The analysis methodology is given in Section 3.1.

2.6 Shockwave Propagation Velocity and Pressure Measurements of Novel Detonation Mechanism

Shots comprising a source of H and HOH catalyst were ignited by passing a low voltage, high current through the shot to produce explosive power, an electromagnetic pulse, and a shockwave. The shock wave propagation velocity and pressure were measured and compared to standard energetic materials gunpowder and ammonium (AN). The shots comprised (i) hydrated silver shot (70 mg/6.5 x 10^{-4} moles Ag + 6.5 x 10^{-5} moles H_2O) (ii) Ti powder (15 mg/3.1 x 10^{-4} moles) + H_2O (5 mg/2.8 X 10^{-4} moles) in an aluminum DSC pan (75 mg) (aluminum crucible 30 µl, D: 6.7 mm×3 mm (Setaram, S08/HBB37408) and aluminum cover D: 6.7 mm, stamped, tight (Setaram, S08/HBB37409), (iii) Ti powder (83 mg/1.7 x 10^{-3} moles) + H_2O (30 mg/1.7 x 10^{-3} moles) in the Al DSC pan, (iv) gunpowder (47 mg/0.563 x 10^{-3} moles) in the Al DSC pan, (v) NH_4NO_3 (58 mg/7.25 x 10^{-4} moles) in the Al DSC pan. The source of the ignition current was the Acme 75 KVA welder. As shown in Figures 5 and 6, the samples were placed between two copper electrodes connected to the spot welder buss bar with a pressure of 25 lb. The electrodes comprised 1.6 cm diameter solid copper rods with the sample ends tapered to a diameter of 8 mm to cover Al DSC pan diameter of 6.7 mm. The shockwave pressure probes comprised two NIST traceable quartz ICP blast pressure sensors (PCB Piezotronics, Model 137B23B) having a sensitivity of 100.8 mV/PSI, a measurement range of 50 PSI, a maximum pressure of 1000 PSI, a resolution of 0.01 PSI and a rise time of less than or equal to 6.5 µsec. The two probes were set at the front and side 38.1 cm from sample at the same height of the sample (1.1 m from floor). A photodiode detector was placed at 1.27 m from the sample to detect the emission light. A reflection wall was placed 23 cm from the back of the sample. The spot welder output voltage, spot welder current, the probe pressure, and the photodiode light intensity signal were measured as a function of time by picoscope triggered by spot welder output current signal. The spot welder power output peak (product of voltage and current) or an electromagnetic pulse (EMP) spike was used as the start time of the shockwave. The photodiode signals from the blast were found to have a delay compare to power output peak or the EMP signal. Pressure measurements were taken at different angular positions at a fixed radius and confirm that all sample blasts had equal intensity distribution in all directions. The shockwave speed for the sample comprising Ti powder (83 mg/1.7 x 10^{-3} moles) + H_2O (30 mg/1.7 x 10^{-3} moles) in the Al DSC pan was measured at distances of 25.4 cm, 38.1 cm, 63.5 cm, 76.2 cm.

2.7 Raman, XPS, and NMR Analytical

The molecular hydrino samples comprised an indium witness plate, a ball-milled 1:1 mol% NaOH-KCl mixture, or activated carbon placed in a sealed container under argon wherein hydrinos generated with ignition were trapped in the matrix of the indium, NaOH-KCl mixture, or activated carbon that thereby served as a molecular hydrino getter. Raman spectroscopy, and X-ray photoelectron spectroscopy (XPS), and magic angle spinning ^1H nuclear magnetic resonance spectroscopy (MAS ^1H NMR) were performed on reaction products. Starting materials not exposed to a hydrino source served as controls. The hydrino reaction product samples were prepared by exposing the getter to hydrino gas over 20 individual shot ignition events.

2.7a Raman Identification of Molecular Hydrino

Raman spectroscopy was performed on the indium metal foils and on solid ball-milled 1:1 mol% NaOH-KCl mixture samples using a Thermo Scientific DXR SmartRaman spectrometer having a 780 nm diode laser. The resolution, depending on the instrument focal length, wavelength range, and grating, was typically 1-5 cm^{-1}. Controls comprised foils and getters not exposed to hydrino gas. Raman spectra were also recorded on the on solid ball-milled 1:1 mole % NaOH-KCl mixture samples using the Horiba Jobin Yvon LabRAM Aramis Raman spectrometer with a HeCd 325 nm laser in microscope mode with a magnification of 40X.

2.7b XPS Identification of Molecular Hydrino

A series of XPS analyses were made on indium foil witness plates using a Scienta 300 XPS Spectrometer or a Kratos Analytical Axis Ultra. The fixed analyzer transmission mode and the sweep acquisition mode were used. The step energy in the survey scan was $0.5\ eV$, and the step energy in the high-resolution scan was $0.15\ eV$. In the survey scan, the time per step was 0.4 seconds, and the number of sweeps was 4. $C\ 1s$ at $284.5\ eV$ was used as the internal standard.

2.7c MAS ^1H NMR Identification of Molecular Hydrino

^1H MAS NMR was performed on solid samples using a 500 MHz Bruker instrument with spin speeds of 5 kHz, 10 kHz, and 17.5 kHz to eliminate spinning side bands that shifted with a change in spin speed. Chemical shifts were referenced to external TMS.

3 Results and Discussion

3.1 Absolute Power Spectrum of Ignited Hydrated Silver Shots

3.1.a Absolute Calibration and Power Spectrum of Ignited Hydrated Silver Shots

The Mightex UV-Vis spectrometer was wavelength calibrated using emission lines generated by a mercury argon wavelength calibration source (Model: Ocean Optics HG-1) in the 200-800 nm wavelength range (Figure 7). A 3rd order polynomial was used to generate the pixel to wavelength mapping. The absolute spectral irradiance calibration was performed on a UV-Vis Mightex system spectrometer using a NIST traceable deuterium lamp and a NIST traceable quartz tungsten halogen lamp to cover the region 200-2400 nm. The NIST traceable quartz tungsten halogen lamp spectrum acquired on the Mightex UV-Vis is shown in Figure 8 and the NIST traceable quartz tungsten halogen lamp standard spectral irradiance is shown in Figure 9. The NIST traceable Gooch & Housego deuterium lamp spectrum acquired on the Mightex UV-Vis is shown in Figure 10, and the NIST traceable Gooch & Housego deuterium lamp standard spectral irradiance is shown in Figure 11. The Mightex UV-Vis spectrometer efficiency spectrum C_p (mJ/count) versus wavelength obtained from the NIST traceable quartz tungsten halogen lamp and the NIST traceable Gooch & Housego deuterium lamp is shown in Figure 12 wherein the standard curve from the NIST traceable quartz tungsten halogen lamp covered the region 200-800 nm. The NIST traceable quartz tungsten halogen lamp intensity calibration was

extended from the visible to UV region by stitching the corresponding visible curve to the NIST traceable Gooch & Housego deuterium lamp calibration over the region of overlap as shown in Figure 13 to give the final spectrometer efficiency spectrum C_p over the 200 nm to 800 nm region shown in Figure 14.

The hydrated silver shots comprising a source of H and HOH hydrino catalyst were ignited by passing a low voltage, high current through the shot to produce explosive plasma that emitted brilliant light predominantly in the short-wavelength (10 to 300 nm) region. Superimposed Mightex UV-Vis (200-815.4 nm) spectra of the shot blast emission from five runs are shown in Figure 15. The spectra were corrected for the attenuation by the optical elements such as the MgF_2 window on the entrance to the Mightex UV-Vis spectrometer having the transmission curve shown in Figure 16. The Mightex UV-Vis (200-815.4 nm) spectrum was corrected by dividing the data by the transmission efficiency of the window (Figure 16).

The wavelength calibration of the GIS was achieved using a high-voltage discharge in air and helium microwave plasma (Figures 17A-B). The wavelength calibration of the NIS was achieved using the Ocean Optics HG-1 mercury-argon lamp (Figure 7) and helium microwave plasma (Figure 17B). The raw spectra (22-647 nm) obtained using the GIS and NIS with the CCD centered at different positions and having an MgF_2 window or Al filter depending on the wavelength region are shown in Figure 18 wherein the 5 nm to 65 nm region was recorded with the GIS. The CCD dark counts were subtracted from all spectra. Spectra were recorded on the NIS using the MgF_2 window with the CCD centered at 300, 400, and 500 nm and were recorded without a window in the case of the centering at 200 nm since otherwise the window at wavelengths below 200 nm would have attenuated the intensity. Matching the intensities at overlapping spectral wavelengths were used to join curves (Figure 19). The joined (200-640 nm) spectrum are shown in Figures 20 and 21, respectively. The NIS joined spectra were corrected for the attenuation by the MgF_2 window by dividing the data by the transmission efficiency of the window given in Figure 16. The joined window corrected NIS spectrum shown in Figure 22 was corrected for the reflectance of the NIS 300G Al-MgF_2 coated grating (Figure 16) by dividing the data by the grating reflectance curve to give the corrected combined spectrum shown in Figure 23. The grating efficiency curve was taken as flat which was confirmed by a comparison of the standard spectra and corrected recorded spectra as discussed in Section 3.1c.

The shot blast emission spectrum (20-65 nm) was recorded on the GIS with the CCD centered 55 nm using no MgF_2 window since those wavelengths were cutoff by the window (Figures 16 and 24). The GIS spectral emission was corrected for the two aluminum filters having a total attenuation path length of 0.8 μm wherein the Al filter transmission is given by Lawrence Berkley National Laboratory [13] (Figure 2B). The GIS spectrum was corrected by dividing the data by the Al filter curve (Figure 2B) to give the filter corrected spectrum shown in Figure 25. The GIS spectrum was corrected for the efficiency of the gold-coated GIS grating (Figure 26) by dividing the data by the wavelength-matched grating efficiency curve to give the corrected GIS spectrum (20-65 nm) shown in Figure 27. Matching the intensities at overlapping spectral wavelengths was used to join the corrected curves of the GIS and the NIS. The superimposed scaled and corrected NIS spectrum (50-650 nm) of Figure 23 and GIS spectrum (20-65 nm) is shown in Figures 28A-B wherein the spectra are joined at the point of spectral coincidence that occurs at about 67 nm. The joined spectrum (20-650 nm) of the GIS and NIS components (Figure 29) was corrected for the Andor camera CCD

quantum efficiency by dividing the data by the wavelength-matched quantum efficiency curve (Figure 16) to give the camera corrected GIS-NIS spectrum (20-650 nm) shown in Figure 30.

The spectral count intensity of the combined GIS and NIS spectra following Al filter, window, grating, and CCD quantum efficiency corrections given in Figure 30 was converted to energy density by multiplying the counts as a function of wavelength by the conversion factor $\frac{hc}{\lambda}$. The resulting combined GIS and NIS energy density spectrum (20-650 nm) before power calibration against the absolutely calibrated UV-Vis spectrum is shown in Figure 31. The MgF_2 window corrected blast ignition spectrum recorded by the absolutely calibrated Mightex UV-Vis spectrometer with the superimposed GIS-NIS energy density spectrum of Figure 31 matched at the region of spectral overlap is shown in Figure 32. The spectral matching between the absolutely calibrated 200-800 nm region of the Mightex UV-Vis spectrometer and the 200-650 nm region of the GIS-NIS energy density spectrum was achieved by scaling the latter such that the integrated energy over the 200-650 nm overlap region of the latter matched that of the former. The integrated emission power in the Mightex UV-Vis spectrum (200-647 nm) was 1165 kW. The total power over the full wavelength range of 22.8-647 nm was integrated on the combined spectrum. From the full wavelength calibrated and absolute intensity calibrated emission spectrum (22.8-647 nm) shown in Figure 32, the average power of the light released from the shot ignition event determined using absolute spectroscopy over the 22.8-647 nm region at 40 μs time resolution was 4616 kW wherein the total power is about 4 times the power in the UV-Vis spectral range (200-647 nm). The total integrated energy over the 1 ms blast duration was 4616 J. The peak power in the UV-Vis spectral range (200-647 nm) was 4813 kW over 40 μs duration (Figure 32) which corresponded to 19 MW over 40 μs duration for the fully recorded spectral range (22.8-647 nm). The actual power was estimated to be at least twice that recorded based on scaling unsaturated lines of the saturated power spectrum (Figure 33).

It was remarkable that the radiation was essentially all short wavelength in the EUV and UV range (Figure 32). The power density was high considering the source of the more than 4.8 MW was produced by a shot of less than 10 microliter volume. This result is even more extraordinary considering the peak power was 19 MW.

To search for the 10.1 nm short wavelength cutoff of the H(1/4) transition continuum radiation while selectively blocking visible light, a 150 nm thick Zr filter (Luxel Corporation) that has a transmission window in the region of 10 nm (Figure 2C) was placed in the light path between the grating and CCD detector. The emission spectrum of the hydrated Ag shot plasma emission using a grating that was not degraded in the short wavelengths showed strong EUV continuum having a 10.1 nm cutoff as predicted [1-7] as shown in Figure 34. Specifically, the radiation is predominantly in the high-energy region with the predicted short wavelength emission of the H(1/4) continuum radiation and the short-wavelength H(1/4) cutoff is observed at 10.1 nm.

3.1b Other Considerations regarding the Power Determination of Ignited Hydrated Silver Shots

In addition to the transmission and efficiency of the optical collection and recording components of the spectroscopy systems, a number of other factors should be considered in the power determination. The G-H NIST D_2 lamp was positioned 44.5 cm from the MgF_2 window of the Mightex spectrometer, and a 25.5 cm

length 3.43 cm ID SS tube of the same type used to the measure the optical power was repeatedly inserted and removed from a flange that mounted the pipe in the light path from the lamp to the spectrometer entrance. The intensity measured by the spectrometer did not change in response to the tube being present or absent demonstrating that the evacuated light conduit did not reflect the EUV light passing through it to have an effect on the intensity. This result is consistent with the known nature of UV and EUV light of having very poor reflectivity on SS surface.

The power from plasma driven by an axial electric field can be emitted in a dipole distribution that results in a $\cos^2\theta$ power distribution and a 1/4 total power correction from that measured at the peak intensity. However, as evidenced by high speed video, the nature of the emission in the case of the shot ignition is an explosion with a spherical wave that propagates out in all directions uniformly except where it is blocked by a physical object such as the electrodes where the power is absorbed to result in recoil of the welder arms and electrodes and molten silver coating, evulsion, and melting of the copper electrodes. The optical power determination was under determined by a plurality of mechanisms.

The NIS spectrum was only corrected for the 300G Al-MgF_2 coated grating reflectance (Figure 16) and not the efficiency as well. The efficiency was only known theoretically as provided by McPherson and was not well known especially at short wavelengths wherein significant corrections and resulting increases in intensity are expected. Taking the efficiency curve as unity provided conservative results that matched standards in the wavelength regions that had the highest blast light intensity as discussed in Section 3.1c.

Further reducing the spectral intensity, the grating had lost some efficiency in the short wavelength region due to Ag coating it. There are three additional factors that were not quantified that diminish the reported power below that actually emitted by the shot blast event: (i) The solid angle for light collection by the spectrometers is greatly reduced by electrode shadowing. It was found that if the electrodes were not beveled, essentially no light gets out. (ii) A related issue with the use of the 1.6 cm diameter electrodes, the great separation distance, and very narrow slits is that the electrodes block the light by reducing the solid angle such that sample-spectrometer alignment is critical. It was very likely that the light was recorded off angle from the sample plane at a diminished light intensity due to electrode shadowing since it is very difficult to perfectly align on axis especially given the movement with the blast event. (iii) The blast vapor and debris are optically thick until the plasma expands to become thinner. If fact, no EUV light was initially observed until a vacuum chamber was used to allow the plasma to expand to become thin enough for the EUV transparency. A substantial amount of the EUV light is absorbed when the power is the greatest in the first time increment following the blast and before transparency is achieved.

3.1c Confirmation of the Method of Spectral Stitching and Optical Element Corrections

The confirmation of the optical element correction method was performed on the NIS by recording the G-H NIST D_2 lamp spectrum on the NIS, performing the same corrections as those applied to the shot blast spectrum, and then comparing the corrected NIS G-H NIST D_2 lamp spectrum to the NIST calibration spectrum, the NIST traceable Gooch & Housego deuterium standard irradiance. The combined efficiency curve C_p comprising the total correction for the components of the transmission curve of the MgF_2 window on the

entrance to the Mightex UV-Vis and NIS spectrometers, the reflectance of the NIS 300G Al-MgF_2 coated grating, and the Andor provided CCD camera quantum efficiency curve as a function of wavelength is shown in Figure 35 wherein each component correction curve is shown in Figure 16. The G-H NIST D_2 lamp spectrum (150-450 nm) recorded on the NIS at 30 cm distance for 200 s is shown in Figure 36. The spectrum was corrected by dividing the data by the combined efficiency curve C_p (Figure 36). The optical element corrected NIS spectrum superimposed on the deuterium standard irradiance (Figure 11) is shown in Figure 37. The match is very good, confirming the optical element correction method.

The confirmation of the method of spectral stitching to obtain an absolutely calibrated spectral response over the 10 nm to 800 nm region is shown in Figures 38 to 44. The L7293 D_2 lamp has a higher irradiance than the G-H NIST D_2 lamp at the same distance as shown in Figure 38. The corresponding Mightex power spectrum of the L7293 D_2 lamp, the G-H NIST D_2 lamp, and the NIST D_2 irradiance are shown in Figure 39. The L7293 D_2 lamp NIS spectrum was corrected by using the Al-MgF_2 reflectance and CCD QE curves (Figure 16). NIS L7293 D_2 lamp spectrum (Figure 40) overlaid with the Al-MgF_2 reflectance and CCD QE corrected L7293 D_2 lamp spectrum. The corrected L7293 D_2 lamp NIS spectrum matches the calibrated Mightex spectrum over the 180-400 nm region as shown in Figure 41 and Figure 42 wherein second order lines are also seen in the NIS spectrum. The corrected L7293 D_2 lamp spectrum matches the relative irradiance of the Hamamatsu L7293 D_2 lamp provided by Hamamatsu [15] for the wavelength region above 155 nm as shown in Figure 43 and further matches the relative irradiance spectrum published by Los Alamos National Laboratory [16] for the region above 155 nm as shown in Figure 44. For the wavelength region below 155 nm, the NIS spectrum showed differences between both published relative irradiance spectra that were attributed to the differences in the D_2 lamps, as well as the experimental conditions and calibrations wherein neither were absolutely calibrated. Since the emission of the blast was primarily in a region having wavelengths longer than 100 nm with a peak at 163 nm, any absolute intensity error from the spectral correction method in the region below 100 nm contributes a corresponding insignificant error in the total power determination for the silver shot blast. Furthermore, since the grating efficiency was not well characterized, the correction method of only using the reflectance of the Al-MgF_2 coated 300 g/mm grating shown in Figure 16 causes this step to be the least certain correction. However, the excellent match between the NIS and absolutely calibrated Mightex spectra that further matched published relative irradiances shown in Figures 42-44 confirmed this method to be appropriate.

The voltage and current parameters of the ignition power source over an ignition event is shown in Figures 45. The optical power result is extraordinary if the voltage spike shown in Figure 45 can be explained and the spike does not contribute to the input power to the light emission. Even though the pulse in the voltage is recorded on the bus bars and electrodes, the current does not spike as well as expected if the pulse was due to applied power. Rather, for the initial portion, it decays with a behavior and corresponding current trace that fits the exponential decay of a pure LR circuit having the decay time constant τ, the time constant of the circuit given by

$$\tau = \frac{L}{R} \qquad (2)$$

Moreover, the circuit interruption by the blast would cause a decrease in current and a corresponding voltage pulse of the opposite sign. Specifically, the voltage $V(t)$ of an LR circuit having circuit inductance L and resistance R is given by

$$V(t) = IR + L\frac{dI}{dt} \tag{3}$$

wherein the input current $I(t)$ having a maximum I_0 was sinusoidal at 60 Hz given by

$$I(t) = I_0 \cos \omega t \tag{4}$$

and

$$\frac{dI(t)}{dt} = -I_0 \omega \sin \omega t \tag{5}$$

From Eq. (3) a negative $\frac{dI}{dt}$ pulse gives rise to a negative voltage pulse contribution. Moreover, the expected effect of the circuit reactance can be appreciated from Figure 45 wherein a voltage in the opposite direction to that applied is observed with the disruption of the power source associated with a programmable duty cycle. Expected ringing in the waveform is also observed, a characteristic signature of LR circuit reactance.

A blast-induced electromagnetic pulse (EMP) of higher voltage than the pre-ignition voltage measured on the electrode bus bars was observed at an independent electrode 20 cm from the blast (Figure 45). The ignition current decayed exponentially indicating that the voltage pulse did not significantly affect it (Figure 45). EMPs were also observed with secondary blasts at times when the current was zero and no reactive voltage was possible. Furthermore, brilliant flashes of EUV light of energy greater than 70 eV were observed during multiple microsecond duration EMP pulses when the ignition voltage was low (< 5 V) and standard sinusoidal as shown in Figure 46. In other cases, the EUV light was observed with EMPs when the ignition current and voltage were zero. The EMP's of non-electrical origin matched the hydrino plasma afterglow (Section 3.3) and confirmed their hydrino reaction basis.

Nuclear and conventional explosive EMPs comprise the abrupt pulse of electromagnetic radiation resulting from a nuclear and conventional [17] explosion, respectively. The resulting rapidly changing electric fields and magnetic fields may couple with electrical/electronic systems to produce voltage surges. The intense nuclear gamma radiation and hydrino soft X-ray radiation emitted can also ionize the surrounding gas, creating a secondary EMP as the atoms of the gas first lose their electrons and then regain them. During a phase of the ignition event, the plasma was confirmed to be essentially 100% ionized by measuring the Stark broadening of the H Balmer α line (Section 3.2).

The EMP is associated with power released and emitted by the blast rather than additional power input to drive the blast. The EMP was eliminated from the measurement of the applied voltage across the shot and the corresponding applied power and energy by measuring the total circuit current and the current of a circuit parallel to the shot of known constant resistance. The results of the calibration and matching of two Rogowski coils to absolutely measure the total and shunt current is shown in Figure 47A. The results of the measurement of the shot current, voltage, power, and energy determined using a standard shunt resistor are shown in Figures 47B-E. The peak voltage across both the shunt and the shot given by product of the measured shunt current and

resistance was 17 V, the peak power applied to the shot was 120 kW, the total energy into the shot during the blast was 17 J and the total energy into the shot from the initiation of shot heating to the end of the blast event was 66 J. From the Edgertronic high-speed video, the shot was observed to ignite just upon melting of the outer surface. Considering the molar heat capacity of silver and the heat of fusion of 25 J/(mol K) and 11.28 kJ/mol, respectively, the energy to melt the 70-80 mg silver shot was about 20 J, energy equivalent to the measured ignition input energy.

The input power to the light emission can also be measured by using the circuit LR parameters that are independent of the EMP. The voltage and current parameters of the ignition power source over an ignition event is shown in Figures 45A-B. The ignition occurred at the point of maximum current where the $\frac{dI}{dt}$ term of Eq. (3) was zero. The measured maximum current occurring at the ignition point was 21.9 kA, and the bus bar to ground and shot to ground voltages (designation shown in Figure 45 A) were 7 V and 3.5 V, respectively, corresponding to circuit resistances of 320 $\mu\Omega$ and 160 $\mu\Omega$, respectively. Using a micro-ohmmeter, the resistance of the circuit across the mounted room temperature shot was measured to be 80 $\mu\Omega$. An identical welder ignition cycle was performed on a non-hydrated silver shot that did not detonate wherein the maximum 60 cycle AC current was 25 kA, and the voltage at zero current was 4.5 volts. From Eq. (3), the corresponding welder inductance was 0.48 μH. From Eq. (2), the corresponding circuit time constant τ was 1.4 ms compared to the measured τ of 0.25 ms. Using the measured L, R, τ, and I_0 circuit parameters considering the exponentially decaying current over the duration of the blast, the integrated total input energy to the circuit during the blast E given by

$$E = \int_0^\infty I^2 R dt = R\int_0^\infty \left(I_0 e^{-\frac{t}{\tau}} \right)^2 dt = \frac{1}{2} R I_0^2 \tau; \ \tau = \frac{L}{R} \qquad (6)$$

was 20 J. Using the measured time of the highest intensity of the optical power blast of 0.5 ms, the average power was less than 40 kW, which is reasonable given that the ignition power source has an average power of 35 kW. The shot current matched the L/R circuit exponential decay for about one time constant τ wherein the majority of the optical power was released based on the temporally resolved (40 μs) Mightex spectral series and the high-speed video. Deviation from ideality then occurred as the electrodes separated due to the blast pressure. At the end of the blast event of about 0.5 ms duration, the electrodes remained separated to maintain an open circuit of essentially infinite resistance. The resulting shot input power was dwarfed by the measured high-energy peak and average optical power of 20 MW and 5 MW, respectively, over 125 times higher. The 20 J of energy determined using the current decay of the LR circuit model given by Eq. (6) matched well to the 17 J applied by the power source during the blast as determined by the parallel circuit measurement method.

The only source of stored energy was the circuit inductive reactance involving the energy periodically stored in the magnetic fields of the transformer coil. The energy stored in the transformer given by

$$E = \frac{1}{2} L I_0^2 \qquad (7)$$

was 115 J. Considering the power division according to the relative shot and balance of circuit resistances, the stored energy that could have been dissipated in the shot was 30 J, and again it was insignificant compared to

the measured 4616 J of optical energy. Moreover, any reactive power would have flowed in the opposite direction to the applied ignition power as a reflected wave on the bus bars comprising the transmission line to decrease the input power and energy. Any reactant reflected power would also have decreased the time constant τ from that given by Eq. (2) to cause a decrease input energy according to Eq. (6).

Given that the measured applied voltage was 17 V, and the insignificant energy input relative to the optical energy, the applied field could not be the source of the emission that extended to 122.4 eV. Moreover, the EUV continuum was observed in our laboratory from plasma having essentially no field. Intense pulses of EUV light (>70 eV) were recorded by a EUV diode when the voltage was very low (< 5 V) as shown in Figure 46, and the voltage was zero in some instances. There is no energy releasing reaction between the combination of silver, water, and copper corresponding to the ignition of the hydrated silver shots at the copper electrodes.

3.2 Balmer α Line Broadening Measurements

The visible spectra in the spectral region of the H Balmer α line measured using the Jobin Yvon Horiba 1250 M spectrometer with 20 μm slits and the Ocean Optics spectrometer is shown in Figures 48A-D. The full width half maximum (FWHM) of the 632.8 nm HeNe laser line was 0.37 Å that confirmed the high spectral resolution of the former. In contrast, the FWHM of the Balmer α line from the emission of the ignited hydrated silver shot under atmospheric argon was massively broadened, and the line was shifted by +1.2 Å. The Voigt-fit to the spectral profile gave FWHM of 22.8 Å broadening (Figure 48C) that is far too excessive to comprise a significant Doppler [18-24] or pressure broadening contribution [25]. An electron density of 4 x $10^{23}/m^3$ was determined from the Stark broadening using the formula of Gigosos et al. [26] with the corresponding full width half maximum of 14 Å. During a phase of the ignition event, the plasma was almost completely ionized.

3.3 High-speed video, current, voltage, and spectroscopic measurement of ignited hydrated silver shots

High-speed (17,791 frames per second) video recording of brilliant light-emitting expanding plasma formed from the low voltage, high current detonation of the hydrated silver shot with synchronized recording of the voltage and current waveforms (Figure 49) show plasma at a time when there was no electrical input power for a fuel having no known energy-releasing chemical reaction. The plasma persisted for 4 ms while the input power was zero at 0.8 ms. An initial transient voltage spike that was greater than the peak AC power of 75 kW was assigned to the effect of the electromagnetic pulse (EMP) (Section 3.1) on the Rogowski coil that was less than the effect on the voltage probe. The EMP did not contribute to the power input to the shot as indicated by the exponential current decay. The UV-Vis spectrum recorded with the Mightex system (40 μs time resolution) at a time 40 μs post the input ignition power becoming zero showed argon ion plasma emission lines (Ar I 588.8, 518.8 nm, and 549.6 nm) and an UV-Vis power of 11 kW that typically represented only 20% of the total power that was predominantly EUV wavelength range emission. Proof of a new energy source is provided by two otherwise inexplicable observations: (i) The formation of a high-energy plasma in the absence of any input electrical power, the nonexistence of any energy releasing chemistry with this fuel, and the further

impossibility of known chemistry of this high energy. (ii) The emission of EUV radiation at a voltage far less than that of the light energy produced and the inability of any known chemistry to release such high energy.

3.4 Spectrum of Continuous Molten Silver Injection to Compare with that of Ignited Hydrated Silver Shots

The UV emission of the plasma produced in a vacuum chamber by continuous injection of hydrated molten silver recorded by the normal incidence EUV spectrometer is shown Figure 50 with a superposition of the spectrum recorded on the hydrated silver shot. The comparison indicates that the UV spectral emission of the plasma formed by continuously dripping molten silver into tungsten electrodes powered by capacitors to deliver a low voltage, high ignition current is the same as that of the single shots given in Section 3.1.

High-speed video and spectroscopy was recorded on the plasma formed by dripping molten silver from an overhead source into V-shaped W electrodes mounted on copper bus bars. The current was provided by two parallel pairs of series-connected capacitors (Maxwell Technologies K2 Ultracapacitor 2.85V/3400F). The molten silver was maintained in a quartz cylinder by applying inductively coupled heating power to a circumferential antenna coil. Water was injected into the molten silver to achieve about 1 mole percent dissolved H_2O. The temporal evolution of the plasma reaction captured as high-speed video frames and the UV-Vis spectra taken at 40 μs intervals is shown at times indicated in Figures 51A-C and 52A, respectively. The temporal spectral evolution for a repeat run is shown in Figure 52B. The spectral evolved from line emission (corresponding to the portion of the windowless spectrum shown in Figure 32 not cut on the short-wavelength side by the fuse quartz window of the spectrometer) to blackbody radiation of increasingly high temperature with time as indicated by the temporal sequence of spectra shifting from long wavelengths to short (220 nm) wavelengths. The slow motion video given in the Brilliant Light Power, Inc. link [27] begins with high energy light (corresponding to the line spectrum); the silver vaporizes, and the plasma becomes optically thick, the emission and spectrum become that of a blackbody radiator with a temperature of about 5700K as confirmed by a matching Stefan Boltzmann equation plot. Figures 52A-B show the 5700K blackbody plasma that filled the argon-atmosphere glove box in which the reaction was contained. The plasma surface area was about 1 m^2. The power of a blackbody at 5700K is given by 60 MW/m^2 times the emissivity. Using the emissivity of molten silver of 0.03 [28] as that of the silver vapor plasma, the radiated power was estimated to be about 1.8 MW.

3.5 Bomb Calorimetry of Ignited Hydrated Silver Shots

Using the copper electrodes without hydrated silver shot, the heat capacity of the calorimeter and electrode apparatus used to measure the energy balance of hydrated silver shot samples was determined to be 6400 J/°C. The calorimetry method used to determine the thermal output from the temperature versus time response following equilibration and ignition was the analytical method described in the operating manual of the Parr 1341 bomb calorimeter [14]. The net energy is the difference between the thermal output and energy input.

The input energy of the calibration and ignition of the hydrated silver shot was given as the product of the voltage and current integrated over the time of the input. In the case of ignited shots, the input power data was separately processed to calculate the input energy during the pre-ignition heating phase and during the rapid power decay following ignition to an open circuit. (Unlike the case of the optical power determination that used flexible pressurized bus bars, the calorimeter circuit bus bars where rigidly fixed such that a gap opened when the shot blew out). Taking the product of the measured voltage waveform obtained from the voltage taps immediately above the water level on the 5/8" OD Cu rods and the measured current waveform given by the Rogowski coil yielded the power waveform. The time integrated power waveform yielded the cumulative energy provided to the system to the time point that the ignition or detonation event occurred that created an open circuit. Using the methods of Sections 2.5 and 3.1, the maximum input voltage was 12 V, and the input energy during the blast event was measured to 20 J. The 20 J blast-time-period input energy was added to the integral of the voltage and current for the non-blast portions of the VI waveform. The repeatability of the externally determined input energy of 20 J was attributed to the constancy of the welder inductance of 0.045 μH (much smaller for the Acme welder compared to the Taylor-Winfield) and the reproducibility of the circuit resistance wherein the contribution of the shot (~80 $\mu\Omega$) was smaller than the resistance of balance of the circuit (200 $\mu\Omega$) such that any small variability in the shot resistance had a negligible effect. The input power and energy to the ignited shot during calorimetric measurement was very similar to those of the ignited shot during optical power measurement as shown in Figure 53 and Figure 47E, respectively. Again, the average power of about was 45 kW, about that of the average power rating of the welder, and it was divided proportionally between the relative series resistance of the bus bars and the shot. The average power from the ignition of a fuel shot given by the calorimetrically determined net energy divided by the time of the ignition plasma event of 0.5 ms was much greater, hundreds of thousands of watts. The controls were appropriate in being resistive in nature, showing no energetic behavior. Energetic samples are expected to show energy; therefore they do not serve as proper controls. The results of the controls were consistent the theoretical heat capacity of the calorimetric system.

As in the case of the optical power experiments given in Section 3.1, the current of the LR circuit decayed exponentially with a time constant τ given by Eq. (2) wherein L is the inductance of the welder circuit measured to be 0.045 μH and R is the total shot circuit resistance that is typically about 300 $\mu\Omega$. The resistance was determined from the measured voltage V and current I at a point where the time derivative of the current $\frac{dI}{dt}$ was zero in Eq. (3). Due to the low inductance, τ was small, being about 150 μs, and the time to the open circuit condition can be taken to have a similar duration. Thus, the resistance was taken as constant during the decay of duration τ. The good exponential curve fit of the decay of the current from the initial magnitude of I_0 measured with the Rogowski coil to 36.8% of I_0 corresponding to a decay duration of one time constant τ confirmed that the resistance was sufficiently constant during this time interval for the determination of the input energy E using the integral of the power given by Eq. (6). The typical energy during decay was about 20 J in agreement with the direct energy measurement as well as the direct energy

measurement and LR circuit decay energy calculation of the shot in the optical energy measurements section (Section 3.1).

As shown in Table 1, significant energy and power was observed for the HOH-based hydrated silver shot wherein HOH served as catalyst. Up to 200 J was recorded for an ignition event having the majority of the energy release in a 0.5 ms span corresponding to an average power of 400,000 W. The power from the absolute spectroscopy on the ignition of hydrated silver shot (Sec. 3.1) was higher due to the dissipation of a significant portion of the input power in the two joints and the bus bars of the calorimetric ignition circuit with only about 25% of the input power actually delivered to the shot to cause it to ignite. For hydrated silver, no theoretical energy exits since the no exothermic reaction was possible between argon, hydrogen, H_2O, and silver [29-31].

3.6 Shockwave Propagation Velocity and Pressure Measurements of Novel Detonation Mechanism

The behavior of hydrated Ag shots subjected to low-voltage high-current initiation consistently demonstrate explosive formation of a plasma in which the Ag-H2O constituents are nearly completely ionized. These experiments demonstrate that the resulting air shocks are comparable to those created by the explosive initiation of conventional energetic materials. The results of the shockwave speed and corresponding pressure are given in Figures 54-58 and Tables 2 and 3. The titanium power-water shot with one half the moles of water as moles of gunpowder have slightly higher speed and intensity than gunpowder. An increase in moles of water increased the speed and pressure. Remarkably, hydrated silver shots comprising only 65 μmoles H_2O produced a shockwave that was equivalent to about 10 times more moles of gunpowder (0.6 millimoles).

3.7 Raman, XPS, and NMR Analytical

3.7a Raman Identification of Molecular Hydrino

$H_2(1/p)$ may uniquely undergo a pure ro-vibrational transition having the selection rule $\Delta J = 0, \pm 1$ wherein the rotational energy is $p^2(J+1)0.01509\ eV$ and 0.01509 is the rotational energy of H_2 [1, 8-11]. The predicted hydrino product $H_2(1/4)$ was identified by Raman spectroscopy. Using a Thermo Scientific DXR SmartRaman with a 780 nm diode laser, an absorption peak at 1982 cm^{-1} having a width of 40 cm^{-1} was observed (Figure 59) on the indium metal foil that was exposed to the hydrino product gas. The only possible elements to consider as the source were In and O. Permutations of controls did not reproduce the peak, only samples exposed to the gas showed the absorption peak. Since no other element or compound is known that can absorb a single 40 cm^{-1} (0.005 eV) near infrared line at 1.33 eV (the energy of the 780 nm laser minus 2000 cm^{-1}) $H_2(1/4)$ was considered. The absorption peak starting at 1950 cm^{-1} matched the free space rotational energy of $H_2(1/4)$ (0.2414 eV) to four significant figures, and the width of 40 cm^{-1} matches the orbital-nuclear coupling energy splitting [1]. The absorption was assigned to an inverse Raman effect (IRE) [32] peak for the $H_2(1/4)$ rotational energy for the $J' = 1$ to $J'' = 0$ transition [1] as described previously [8-11].

Permitted by the change in ℓ quantum number, the de-excitation vibrational transition $\upsilon = 1 \rightarrow \upsilon = 0$ with a rotational energy up conversion ($J' - J'' = -1$), a down conversion ($J' - J'' = +1$), and no change ($J' - J'' = 0$) gives rise to the P, R, and Q branches, respectively. The ro-vibrational emission (so called 260

nm band) of $H_2\left(1/4\right)$ trapped in the crystalline lattice of KCl getters was recorded previously by windowless UV spectroscopy by excitation of the emission by an incident 6 keV electron beam [10]. The plot of the energy versus peak number yielded a line given by y = -0.249 eV + 5.8 eV at R^2 = 0.999 or better in very good agreement with the predicted values for $H_2(1/4)$ for the transitions $\upsilon = 1 \rightarrow \upsilon = 0$ and Q(0), R(0), R(1), R(2), P(1), P(2), P(3), and P(4) wherein Q(0) was identifiable as the most intense peak of the series and the vibrational energy $p^2 0.515\ eV$ or four squared that of ordinary H_2 was redshifted due to the lattice reduced mass contribution similar to the factor seen with lattice-embedded ordinary H_2 [9-11].

Another successful cross-confirmatory technique in the search for hydrino spectra involved the use of the Raman spectrometer to record the ro-vibration of $H_2(1/4)$ as second order fluorescence matching the previously observed first order spectrum in the ultraviolet, the 260 nm e-beam band [10]. In this study, the Raman spectrum of the NaOH:KCl (1:1 wt%) getter of the hydrino product gas was recorded using the Horiba Jobin Yvon LabRAM Aramis Raman spectrometer with a HeCd 325 nm laser in microscope mode with a magnification of 40X. No features were observed in the starting material getter. Ball milling the getter which comprised a hydroxide-halide solid fuel [8] resulted in a low intensity series of 1000 cm^{-1} (0.1234 eV) equal-energy spaced Raman peaks observed in the 8000 cm^{-1} to 18,000 cm^{-1} region wherein ball milling has an effect equivalent to heating to drive chemical reactions [33]. An intense, over an order of magnitude, increase in the series of peaks was observed upon exposure to the ignition product gas. The conversion of the Raman spectrum into the fluorescence or photoluminescence spectrum revealed a match as the second order ro-vibrational spectrum of $H_2(1/4)$ corresponding to the 260 nm band first observed by e-beam excitation [10]. Assigning Q(0) to the most intense peak, the peak assignments given in Table 4 to the Q, R, and P branches for the spectra shown in Figure 60 are Q(0), R(0), R(1), R(2), P(1), P(2), P(3) and P(4), observed at 13,226, 12,213, 11,231, 10,196, 14,181, 15,137, 16,107 and 16,998 cm^{-1}, respectively. The theoretical transition energies with peak assignments compared with the observed Raman spectrum are shown in Table 4 and Figure 61. Specifically, the rotational peak energies E_{rot} were calculated using the second order of the 260 nm peak formula

$$E_{rot} = \left[\frac{1240\ eV \cdot nm}{325\ nm} - \left(\left(0, \pm 1 \right) 0.2414\ \left(J+1 \right) eV + 2 \left(\frac{1240\ eV \cdot nm}{325\ nm} - 13{,}236\ cm^{-1} \left(8.06573\ X\ 10^3\ \frac{cm^{-1}}{eV} \right)^{-1} \right) \right) \right] \left(8.06573\ X\ 10^3\ \frac{cm^{-1}}{eV} \right) \quad (8)$$

wherein the theoretical peaks energies were subtracted from the Raman 325 nm laser energy to convert the second order fluorescence spectrum into a Raman spectrum, the lattice-shifted vibrational energy was given by the energy of the Q(0) peak, and 0, ± 1 correspond to Q, P, and R branches.

The excitation was deemed to be by the high-energy UV and EUV He and Cd emission of the laser wherein the laser optics are transparent to at least 170 nm and the grating (Labram Aramis 2400 g/mm 460 mm focal length system with 1024 X 26 μm^2 pixels CCD) is dispersive and has its maximum efficiency at the shorter wavelength side of the spectral range, the same range as the 260 nm band. For example, cadmium has a very intense line at 214.4 nm (5.8 eV) that matches the ro-vibrational excitation energy of $H_2(1/4)$ in KCl matrix

based on the e-beam excitation data [10]. The CCD is also most responsive at 500 nm, the region of the second order of the 260 nm band centered at 520 nm.

Overall, the Raman results such as the observation of the 0.241 eV (1940 cm^{-1}) inverse Raman effect peak and the 0.2414 eV-spaced Raman photoluminescence band that matched the 260 nm e-beam spectrum is strong confirmation of molecular hydrino having an internuclear distance that is 1/4 that of H_2. The evidence in the latter case is further substantiated by being in a region having no known first order peaks or possible assignment of matrix peaks at four significant figure agreement with theoretical predictions. These characteristic ro-vibration signatures of $H_2(1/4)$ match those observed previously on thermal and electrochemical cells [8-11].

3.7b XPS Identification of Molecular Hydrino

Using a Scienta 300 XPS spectrometer, XPS was performed at Lehigh University on the indium metal foil that showed a strong 1982 cm^{-1} IRE peak following exposure to the gases from the series ignition of the shots. A strong peak was observed at 498.5 eV (Figure 62) that could not be assigned to any known elements. Na, Sn, and Zn being the only possibilities were easy to eliminate based on the absence of any other corresponding peaks of these elements since only In, C, O, Cu, Ag, and Si peaks were observed. The peak matched the energy of the theoretically allowed double ionization [8-11] of molecular hydrino $H_2(1/4)$. This result confirms the molecular hydrino assignment by Raman spectroscopy, the inverse Raman effect absorption peak centered at 1982 cm^{-1}.

3.7c MAS ^1H NMR Identification of Molecular Hydrino

MAS NMR of molecular hydrino trapped in protic matrix represents a means to exploit the unique characteristics of molecular hydrino for its identification via its interaction with the matrix. A unique consideration regarding the NMR spectrum is the possible molecular hydrino quantum states. Similar to H_2 exited states, molecular hydrinos $H_2(1/p)$ have states with $\ell = 0,1,2,...,p-1$. Even the $\ell = 0$ quantum state has a relatively large quadrupole moment, and additionally, the corresponding orbital angular momentum of $\ell \neq 0$ states gives rise to a magnetic moment [1] that could cause an upfield matrix shift. The MAS NMR spectrum of the carbon getter after exposure to the hydrino reaction product following ignition of the shots are shown in Figure 63. The hydrino gas exposed carbon getter showed a matrix to the upfield region of about -7.7 ppm.

IV. Conclusion

Extreme ultraviolet (EUV) continuum radiation (10-30 nm) arising only from very low energy pulsed pinch gas discharges comprising some hydrogen was first observed at Brilliant Light Power, Inc. and reproduced at the Harvard Center for Astrophysics (CfA). The source was determined to be due to the HOH catalyzed transition of H to the lower-energy hydrogen or hydrino state H(1/4). The HOH catalyst was further shown to give EUV radiation of the same nature by igniting hydrated silver shots comprising a source of H and HOH catalyst by passing a low voltage, high current through the shot to produce explosive plasma that emitted

brilliant light predominantly in the short-wavelength 10 to 300 nm region. The power and energy of the light released from the shot ignition event were determined using absolute spectroscopy over the 22.8-647 nm region. The peak and average powers of the light released from the shot ignition event determined using absolute spectroscopy over the 22.8-647 nm region were 19 MW and 4.6 MW corresponding to 800 J in 40 us and 4616 J in a 1 ms blast event, respectively. The power density was high considering the source of the more than 4.6 MW was a shot of less than 10 microliter volume. This result is even more extraordinary considering the peak power was 19 MW.

The kinetics of catalysis of H to H(1/4) by HOH catalyst was explosive when a high current such as 22,000 A was flowed through ~80 mg hydrated silver shots comprising a source of H and HOH embedded in a highly conductive matrix. The resulting brilliant light-emitting expanding plasma emitted the EUV continuum radiation emission with short wavelength cutoff and energy of $m^2 \cdot 13.6 \text{ eV} \left(\frac{91.2}{m^2} \text{ nm} \right); m = 3$ predicted for the HOH catalysis reaction of H to $H_2\left(1/4\right)$ when it was expanded into a vacuum chamber such that its high pressure was dissipated sufficiently to overcome the optical thickness. Based on a spectroscopically measured Stark line broadening, during the initial phase of the ignition event, the H_2O-based fuel ignition produced essentially fully ionized plasma that was optically thick. The explosive plasma expanded at sound speed or greater [7] to become optically thin with a transparency to short wavelength light to 10.1 nm (122.4 eV). Remarkably, the emission during the optically thin plasma stage of the blast was essentially all EUV and UV light with essentially no visible or infrared emission. Due to the optical thickness of elements in the plasma, ion emission lines were observed as expected on a continuum radiation background due to continuum absorption and reemission as spectral lines, predominantly silver atom and ion lines. Synchronized high-speed video and spectroscopic recording of the plasma emission and the measurement of the applied ignition power over time showed that plasma with high energy light emission persisted even after the ignition power decayed to zero.

Any alternative mechanism of the EUV continuum emission such as being due to a high electric field creating highly charged ions was dispatched since the measured voltage of the ignition current source was under 15 V and the optical emission energy was 250 times the applied energy. Moreover, chemical reactions are not capable of more than a few eVs, whereas, the continuum radiation extended to 122.4 eV. The electric field was confined between the electrodes, and the plasma expanded at sound speed or greater. The plasma had to expand into vacuum away from the electrodes to be sufficiently optical thin to observe soft X-ray emission. Thus, essentially all of the emission occurred outside of the electrode region. The electron temperature was consequently low, about 1 eV, a factor of 100 times less than required to support the observed >100 eV continuum radiation [7]. It is difficult to achieve this high an electron temperature even at low densities, and it is extremely improbable to be formed at solid to atmospheric high densities of the hydrated silver shot plasmas by a conventional means. No high field existed to form highly ionized ions that could give radiation in this region. Moreover, as shown in Figure 49, following ignition, high-power plasma was observed with no power input. The soft X-ray energy exceeded the total input energy by a factor of 250 (Section 3.1). The massive power of the EUV emission during phases of the ignition event requires a unique high energy and a high power source other than that provided by the electrical input. Controls showed no soft X-ray emission. This plasma

source serves as strong evidence for the existence of the transition of H to hydrino H(1/4) by HOH as the catalyst as a new energy source. The H_2O-based solid fuels behave as energetic materials of extraordinarily high power density with most of the energy released as high energy light versus pressure-volume work. This aspect can be appreciated by comparison of high-speed video recordings of hydrino-based (Figures 49 and 51A-C) and conventional explosives that show billowing smoke and fire [34-35].

The plasma EUV emission with continuous molten silver injection with hydrated silver matched that of the hydrated silver shots. The short wavelength light was absorbed by silver vapor, which was formed by power released by the hydrino reaction by the rapid ignition of water-entrained molten silver gravity feed between tungsten ignition electrodes. The continuous plasma reached a blackbody temperature of about 5700K when the plasma became optically thick from silver vaporization wherein the corresponding blackbody radiative power given by the product of a radiance of 60 MW/m^2, a plasma surface area of 1 m^2, and an emissivity of 0.03 [28] was estimated to be about 1.8 MW, greatly exceeding the average capacitor power of about 5 kW. This result further confirmed the hydrino power source that greatly exceeded the average ignition power of the capacitors of about 5 kW. The energetic ignition reaction produced an EMP similar to that of an explosive. The temperature of high explosives is also as high as 5500 K [36-37].

The power of the shot ignition was further measured calorimetrically wherein the energy released from a 80 mg, 10 microliter shot by the nascent HOH catalyzed transition of H to hydrino state $H_2(1/4)$ was observed to be up to 200 J for an approximately 0.5 ms event corresponding to an average power of 400,000 W. Shots such as hydrated silver shots comprising a source of H and HOH catalyst were ignited by passing a low voltage, high current through the shot to produce explosive power, an electromagnetic pulse, and a shock wave. The shockwave propagation velocity and the corresponding pressure were measured and compared to standard energetic materials gunpowder and ammonium (AN). Hydrated silver shots comprising only 65 μmoles H_2O produced a shockwave that was equivalent to about 10 times more moles of gunpowder (0.6 millimoles). Water and silver have no known chemistry and the ignition voltage did not exceed 20 V; yet the ignition of the hydrated shots produced an extremely powerful detonation wave further validating the hydrino reaction as a new energetic power source. Since there are no gaseous products, a likely mechanism is coupling of the massive amounts to EUV radiation to air to cause superheating akin to the mechanism of nuclear detonation where X-rays serve the role of the EUV radiation of comparable peak power density (e.g. 20 WM/7.6 X 10^{-6} liter = 2.6 X 10^{12} W/liter in the presented hydrino reaction case). Similarly, the hydrino reaction may be the source of the shockwave of lightning discharges in atmospheric water vapor. The predicted molecular hydrino $H_2(1/4)$ was identified as a product of the hydrated silver ignition by Raman spectroscopy, photoluminescence emission spectroscopy, X-ray photoelectron spectroscopy, and MAS ^1H NMR.

References

1. R. Mills *The Grand Unified Theory of Classical Physics* September 2016 Edition posted at http://brilliantlightpower.com/book-download-and-streaming/.
2. R. L. Mills, Y. Lu, "Hydrino continuum transitions with cutoffs at 22.8 nm and 10.1 nm," Int. J. Hydrogen Energy, 35 (2010), pp. 8446-8456, doi: 10.1016/j.ijhydene.2010.05.098.

3. R. L. Mills, Y. Lu, K. Akhtar, "Spectroscopic observation of helium-ion- and hydrogen-catalyzed hydrino transitions," Cent. Eur. J. Phys., 8 (2010), pp. 318-339, doi: 10.2478/s11534-009-0106-9.
4. R. L. Mills, Y. Lu, "Time-resolved hydrino continuum transitions with cutoffs at 22.8 nm and 10.1 nm," Eur. Phys. J. D, Vol. 64, (2011), pp. 65, DOI: 10.1140/epjd/e2011-20246-5.
5. R. L. Mills, R. Booker, Y. Lu, "Soft X-ray Continuum Radiation from Low-Energy Pinch Discharges of Hydrogen," J. Plasma Physics, Vol. 79, (2013), pp 489-507; doi: 10.1017/S0022377812001109.
6. A. Bykanov, "Validation of the observation of soft X-ray continuum radiation from low energy pinch discharges in the presence of molecular hydrogen," http://www.blacklightpower.com/wp-content/uploads/pdf/GEN3_Harvard.pdf.
7. R. Mills, J. Lotoski, Y. Lu, "Mechanism of Soft X-ray Continuum Radiation from Low-Energy Pinch Discharges of Hydrogen and Ultra-low Field Ignition of Solid Fuels", (2017), in press, http://brilliantlightpower.com/wp-content/uploads/papers/Cont_EUV_HOH-031215.pdf.
8. R. Mills, J. Lotoski, W. Good, J. He, "Solid Fuels that Form HOH Catalyst," Int'l J. Hydrogen Energy, Vol. 39 (2014), pp. 11930–11944 DOI: 10.1016/j.ijhydene.2014.05.170.
9. R. Mills J. Lotoski, "H_2O-based solid fuel power source based on the catalysis of H by HOH catalyst", Int'l J. Hydrogen Energy, Vol. 40, (2015), 25-37.
10. R. Mills, X Yu, Y. Lu, G Chu, J. He, J. Lotoski, "Catalyst induced hydrino transition (CIHT) electrochemical cell," Int. J. Energy Res., Volume 38, Issue 13 (2013), pp 1741-1765; DOI: 10.1002/er.3142.
11. R. Mills, J. Lotoski, J. Kong, G. Chu, J. He, J. Trevey, "High-Power-Density Catalyst Induced Hydrino Transition (CIHT) Electrochemical Cell." Int. J. Hydrogen Energy, 39 (2014), pp. 14512–14530 DOI: 10.1016/j.ijhydene.2014.06.153.
12. Newport Light Sources document, Figure 2 (page 16: http://assets.newport.com/webdocuments-en/images/light_sources.pdf).
13. Lawrence Berkley National Laboratory, http://henke.lbl.gov/optical_constants/filter2.html.
14. http://www.parrinst.com/products/oxygen-bomb-calorimeters/1341-plain-jacket-bomb-calorimeter/.
15. https://www.hamamatsu.com/resources/pdf/etd/D2lamps_TLS1017E.pdf
16. Relative irradiance spectrum published by Los Alamos National Laboratory; J. Danielson, G. Sinnis, "Ultraviolet Light Sources for LAr Detector Calibration", Presentation on February 2, 2013, Los Alamos National Laboratory; https://www.google.com/search?q=injection+of+vuv+photons+into+LAr&oq=injection+of+vuv+photons+into+LAr&aqs=chrome..69i57.14799j0j8&sourceid=chrome&ie=UTF-8.
17. J. E. Fine, "Estimates of the electromagnetic radiation from detonation of conventional explosives", Army Research Laboratory, Adelphi, MD, ARL-TR-2447, September, (2001).
18. K. Akhtar, J. Scharer, R. L. Mills, "Substantial Doppler broadening of atomic-hydrogen lines in DC and capacitively coupled RF plasmas**,"** J. Phys. D, Applied Physics, Vol. 42 No.13, (2009), doi:10.1088/0022-3727/42/13/135207.
19. R. Mills, K. Akhtar, "Tests of features of field-acceleration models for the extraordinary selective H Balmer

α broadening in certain hydrogen mixed plasmas," Int. J. Hydrogen Energy, Vol. 34, (2009), pp. 6465-6477.

20. R. L. Mills, B. Dhandapani, K. Akhtar, "Excessive Balmer α line broadening of water-vapor capacitively-coupled RF discharge plasmas," Int. J. Hydrogen Energy, Vol. 33, (2008), pp. 802-815.
21. R. Mills, P. Ray, B. Dhandapani, "Evidence of an energy transfer reaction between atomic hydrogen and argon II or helium II as the source of excessively hot H atoms in RF plasmas," Journal of Plasma Physics, Vol. 72, Issue 4, (2006), pp. 469-484.
22. J. Phillips, C-K Chen, K. Akhtar, B. Dhandapani, R. Mills, "Evidence of catalytic production of hot hydrogen in RF generated hydrogen/argon plasmas," International Journal of Hydrogen Energy, Vol. 32(14), (2007), 3010-3025.
23. R. L. Mills, P. C. Ray, R. M. Mayo, M. Nansteel, B. Dhandapani, J. Phillips, "Spectroscopic study of unique line broadening and inversion in low pressure microwave generated water plasmas," J. Plasma Physics, Vol. 71, Part 6, (2005), pp. 877-888.
24. R. L. Mills, K. Akhtar, "Fast H in hydrogen mixed gas microwave plasmas when an atomic hydrogen supporting surface was present," Int. J. Hydrogen Energy, 35 (2010), pp. 2546-2555, doi:10.1016/j.ijhydene.2009.12.148.
25. R.M. van der Horst, T. Verreycken, E.M. van Veldhuizen, "P.J. Bruggeman, "Time-resolved optical emission spectroscopy of nanosecond pulsed discharges in atmospheric pressure N_2 and N_2/H_2O mixtures", arXiv:1403.5259v1 [physics.plasm-ph], 20 Mar 2014.
26. M. A. Gigosos, M. A. Gonzalez, V. Cardenoso, Computer simulated Balmer -alpha -beta, and gamma Stark line profiles for non-equilibrium plasmas diagnostics", Spectrochimica Acta Part B, Vol. 58, (2003), pp. 1489-1504.
27. http://brilliantlightpower.com/wp-content/uploads/presentations/Tech-Business%20Presentation%20November%201%202016.pdf, slide 69.
28. http://www.omega.com/temperature/Z/pdf/z088-089.pdf.
29. D. R. Lide, *CRC Handbook of Chemistry and Physics*, 88th Edition, CRC Press, Taylor & Francis, Boca Raton, (2007-8).
30. J. A. Dean, *Lange's Handbook of Chemistry*, Fifteenth Edition, McGraw-Hill Professional, New York, (1999).
31. O. Knacke, O. Kubascheeski, K. Hesselmann, *Thermochemical Properties of Inorganic Substances*, 2nd Ed., Springer-Verlag Berlin, Heidelberg 1991.
32. W. J. Jones, B. P. Stoicheff, "Inverse Raman spectra: Induced absorption at optical frequencies," Physical Review Letters, Vol. 13, No. 22, (1964), pp. 657-659.
33. T. Markmaitree, R. Ren, L. L. Shaw, "Enhancement of lithium amide to lithium imide transition via mechanical activation", J. Phys. Chem. B., Vol. 110, No. 41, pp. 20710-20718.
34. http://www.youtube.com/watch?v=ni4qXAPtrlw
35. https://www.youtube.com/watch?v=HFsAbkkAV-Q
36. R. Simpson, "Unraveling the mystery of detonation," https://www.llnl.gov/str/Simpson99.html.

37. R. Meyer, J. Kohler, A. Homburg, “Explosives”, Sixth Edition, Wiley-VCH Verlag GmbH & Co. KGaA, Weinheim, (2007), p. 119.

Table 1. Determination of the energy balance of the hydrino reactant hydrated silver shot by bomb calorimetry wherein the atmosphere in all cases was $Ar/H_2(3\%)$.

Experiment	Sample	Full Wave Peak I di/dt = 0 (kA)	Full Wave di/dt=0 Voltage (V)	Full Wave Implied Resist (μΩ)	Outer Peak Pre-Init I (kA)	Outer Peak V Prior to Init (V)	Initiation Implied Resist (μΩ)	Thermal Energy Out (J)	VI Fitted Energy (J)	VI Fitted Net Energy (J)	VI Fitted Gain (X)
2017-05-12-TIG8	Ag TIG-BB4	12.55	2.730	89.7	23.448	38.754	89.7	345.1	184.5	160.6	1.87
2017-05-11-TIG7	Ag TIG-BB4	12	5.100	99.6	22.34	41.576	99.6	322.1	140.4	181.7	2.29
2017-05-11-TIG3	Ag TIG-BB4	13	4.240	100.0	21.792	41.224	100.0	331.2	132.5	198.7	2.50
2017-05-11-TIG2	Ag TIG-BB4	12.5	5.700	102.0	21.41	43.041	102.0	286.3	135.1	151.2	2.12
2016-11-03-RF3	Control, Resistive waveform	12.70	1.10	91.5	24.3	2.050	84.4	206.6	203.3	3.3	1.02
2016-11-03-RF2	Control, Resistive waveform	12.70	1.10	91.5	24.3	2.050	84.4	168.0	201.5	-33.6	0.83
2016-11-03-RF1	Control, Resistive waveform	12.70	1.10	91.5	24.3	2.050	84.4	193.6	205.4	-11.8	0.94

Table 2. Blast shockwave speed and corresponding pressure at a distance of 38.1 cm from the blast.

Sample	Average Shockwave Speed (m/s)	Shockwave Pressure (PSI)
Hydrated silver shot (70 mg/6.5 X 10^{-4} moles Ag + 6.5 X 10^{-5} moles H_2O	384	0.25
Ti powder (15 mg/3.1 X 10^{-4} moles) + H_2O (5 mg/2.8 X 10^{-4} moles) in the Al DSC pan	400	0.45
Ti powder (83 mg/1.7 X 10^{-3} moles) + H_2O (30 mg/1.7 X 10^{-3} moles) in the Al DSC pan	422	1.09
Gunpowder (47 mg/0.563 X 10^{-3} moles) in the Al DSC pan	398	0.43
NH_4NO_3 (58 mg/7.25 X 10^{-4} moles) in the Al DSC pan	390	0.44

Table 3. Blast shockwave speed and corresponding pressure of the shot comprising Ti powder (83 mg/1.7 X 10^{-3} moles) + H_2O (30 mg/1.7 X 10^{-3} moles) in the Al DSC pan as a function of distance from the blast.

Distance	Average Shockwave Speed (m/s)	Shockwave Pressure (PSI)
25.4 cm	450	1.61
38.1 cm	413	0.95
63.5 cm	391	0.61
76.2 cm	383	0.47

Table 4. Comparison of the theoretical transition energies (Eq. (8)) and transition assignments [1] with the observed Raman peaks.

Assignment	Calculated (cm^{-1})	Experimental (cm^{-1})	Difference (%)
P(4)	17,130	16,988	0.83
P(3)	16,157	16,107	0.31
P(2)	15,183	15,137	0.30
P(1)	14,210	14,181	0.20
Q(0)	13,236	13,226	0.08
R(0)	12,262	12,213	0.40
R(1)	11,289	11,231	0.51
R(2)	10,315	10,196	1.15

Figures 1A-K. Schematics of the light source comprising hydrated silver shot ignited with a spot welder, the intensity reducing, evacuated light conduit, each of the three spectrometers to cover the spectral wavelength range of 10 nm to 815 nm, and the W-halogen and deuterium calibration lamps. A. Deuterium lamp (Gooch & Housego, model OL UV-40, S/N 1028). B. Calibrated quartz tungsten lamp (QTH) (Newport, model 63350). C-E Ultraviolet-visible (UV-Vis) spectrometer. F-H. Normal incidence EUV spectrometer (NIS). I-K. Grazing incidence EUV spectrometer (GIS).

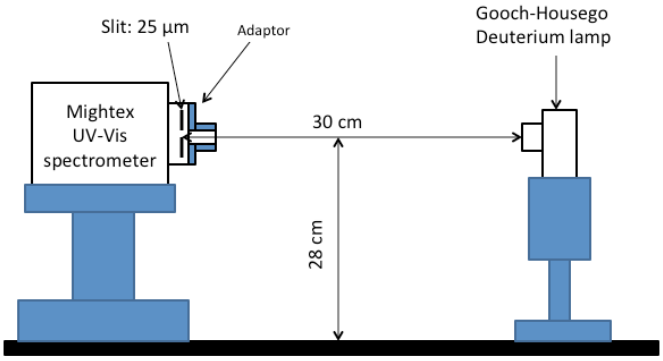

(A)

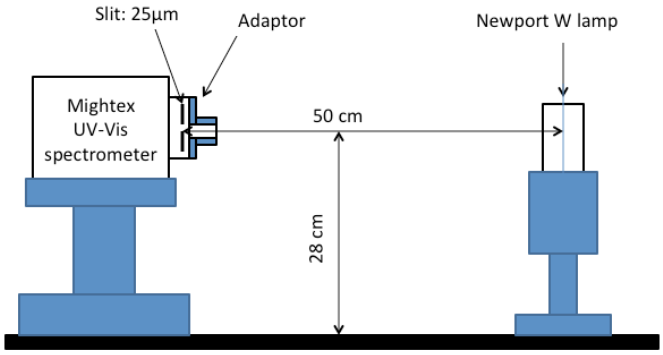

(B)

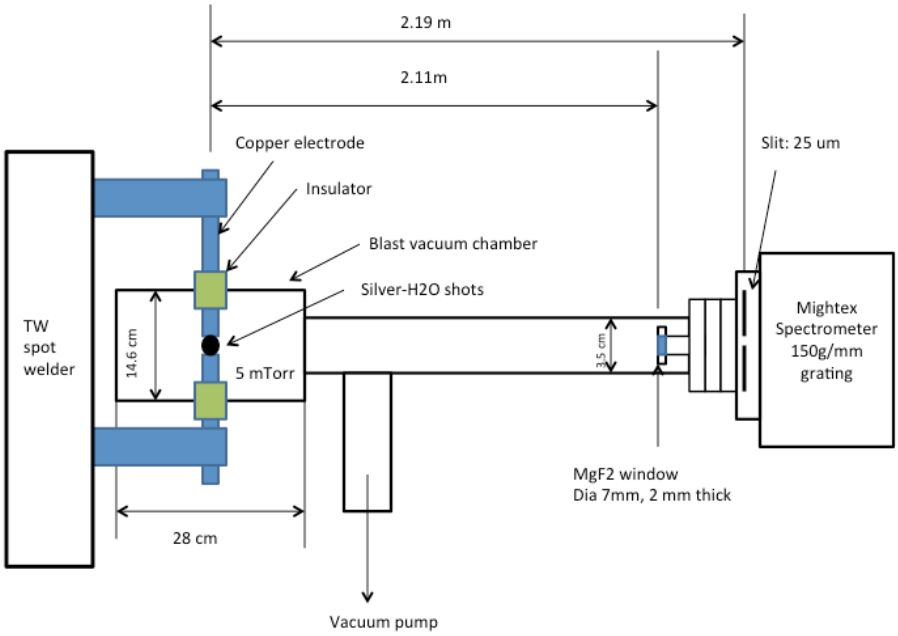
2.19 m
2.11m
Copper electrode
Insulator
Blast vacuum chamber
Silver-H2O shots
Slit: 25 um
TW
spot
welder
14.6 cm
5 mTorr
3.5 cm
Mightex
Spectrometer
150g/mm
grating
MgF2 window
Dia 7mm, 2 mm thick
28 cm
Vacuum pump

(C)

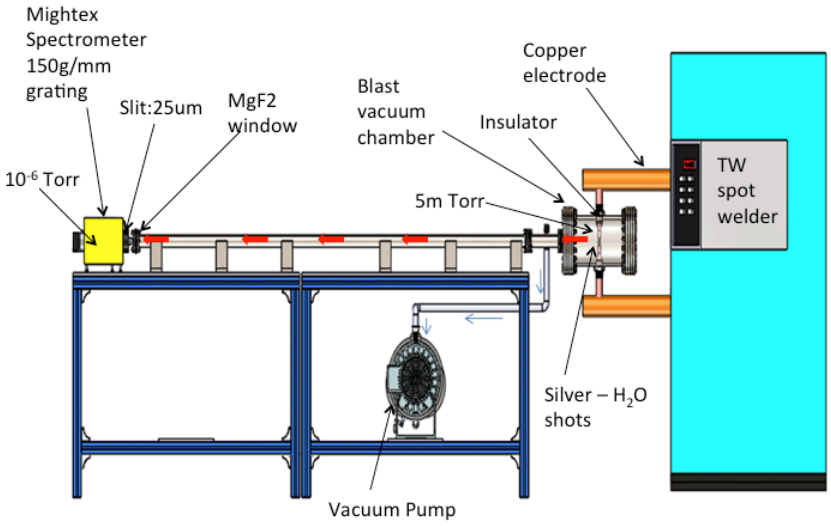
Mightex
Spectrometer
150g/mm
grating
Slit:25um
MgF2
window
Blast
vacuum
chamber
Copper
electrode
Insulator
10-6 Torr
5m Torr
TW
spot
welder
Silver – H2O
shots
Vacuum Pump

(D)

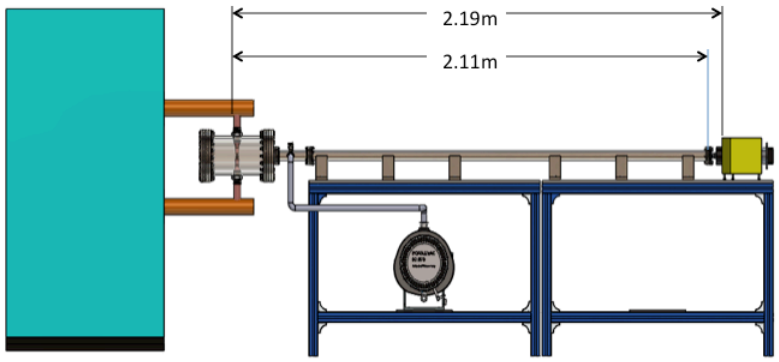
2.19m
2.11m

(E)

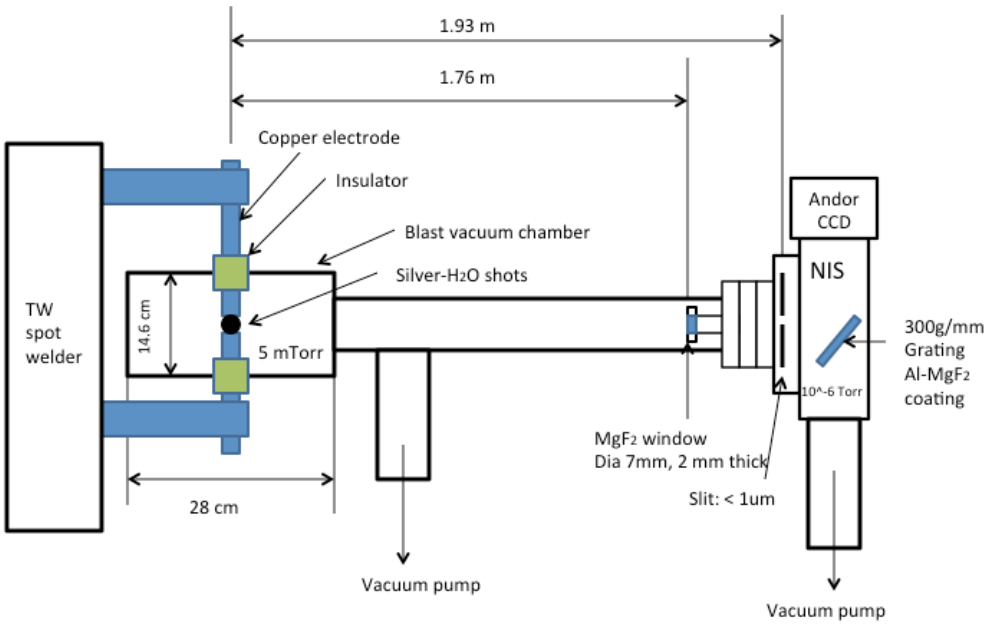
1.93 m
1.76 m
Copper electrode
Insulator
Blast vacuum chamber
Silver-H2O shots
TW
spot
welder
14.6 cm
5 mTorr
28 cm
Vacuum pump
Andor
CCD
NIS
300g/mm
Grating
Al-MgF2
coating
10^-6 Torr
MgF2 window
Dia 7mm, 2 mm thick
Slit: < 1um
Vacuum pump

(F)

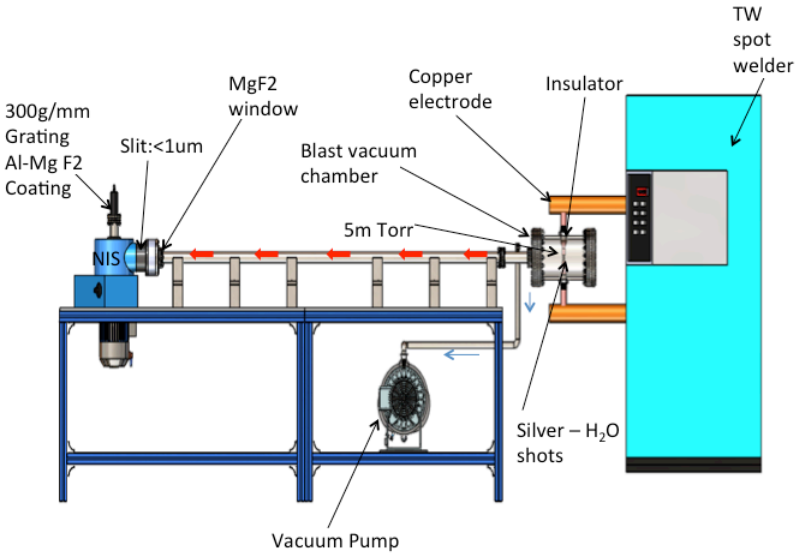
TW
spot
welder
MgF2
window
Copper
electrode
Insulator
300g/mm
Grating
Al-Mg F2
Coating
Slit:<1um
Blast vacuum
chamber
5m Torr
NIS
Silver – H_2O
shots
Vacuum Pump

(G)

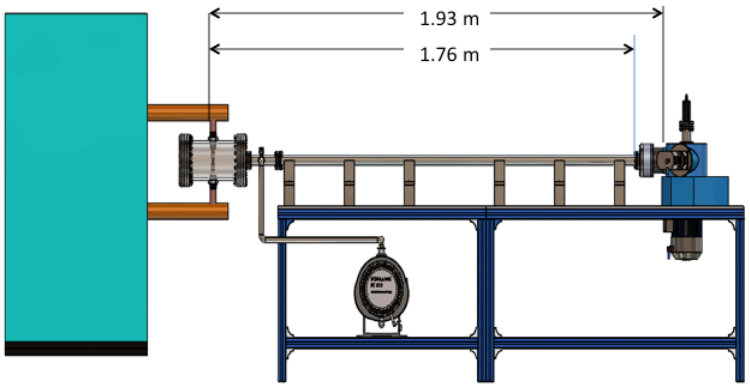
1.93 m
1.76 m

(H)

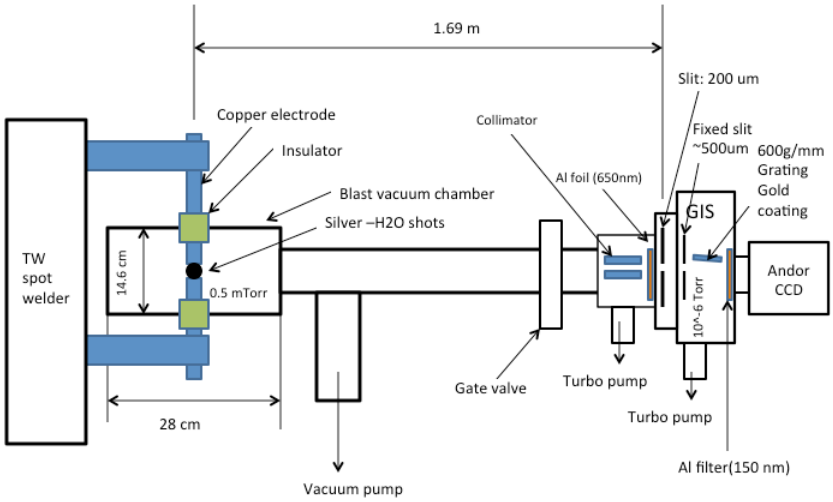
1.69 m
Slit: 200 um
Copper electrode
Insulator
Collimator
Fixed slit
~500um
600g/mm
Grating
Gold
coating
Al foil (650nm)
Blast vacuum chamber
Silver –H2O shots
GIS
TW
spot
welder
14.6 cm
0.5 mTorr
10^-6 Torr
Andor
CCD
28 cm
Gate valve
Turbo pump
Turbo pump
Vacuum pump
Al filter(150 nm)

(I)

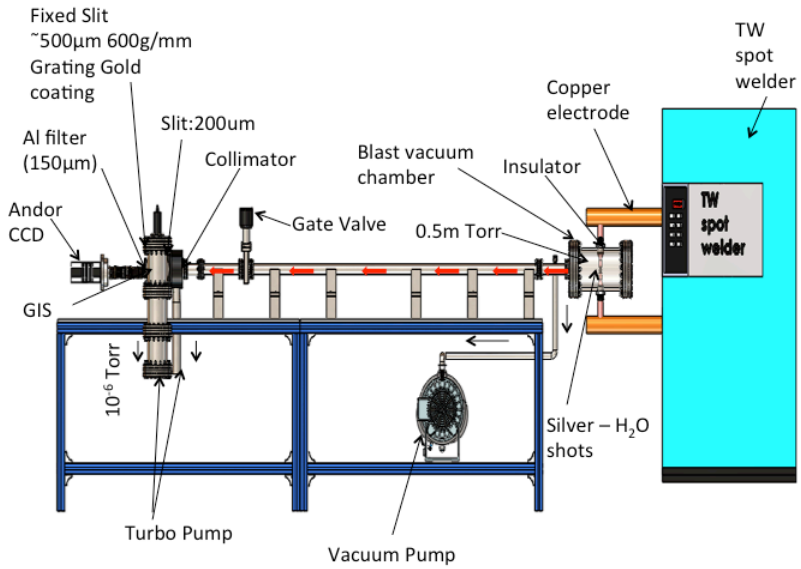
Fixed Slit
~500µm 600g/mm
Grating Gold
coating
TW
spot
welder
Copper
electrode
Slit:200um
Al filter
(150µm)
Collimator
Blast vacuum
chamber
Insulator
Andor
CCD
Gate Valve
0.5m Torr
TW
spot
welder
GIS
10-6 Torr
Silver – H2O
shots
Turbo Pump
Vacuum Pump

(J)

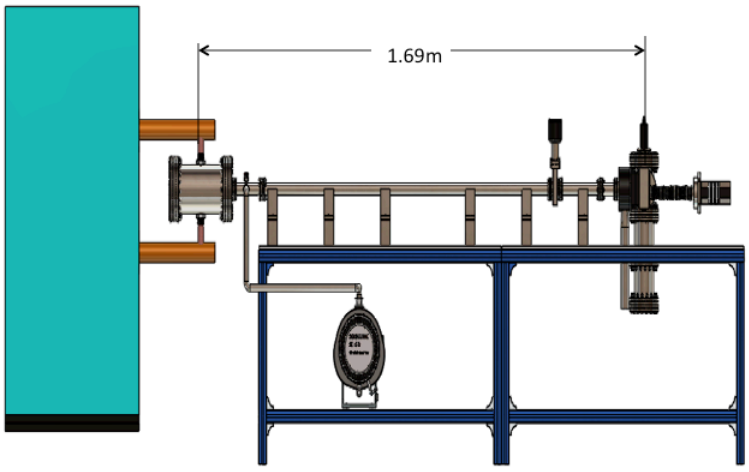

(K)

Figures 2A-C. Transmission curves of filters for EUV light that blocked visible light. A. The Al filter (150 nm thickness) having a cutoff to short wavelengths at ~17 nm. B. The Lawrence Berkley National Laboratory Al filter combined transmission curve given as the sum of the contributions from the 150 nm thick and 650 nm thick Al filters. C. The Zr filter (150 nm thickness) having high transmission at the predicted H(1/4) transition cutoff 10.1 nm.

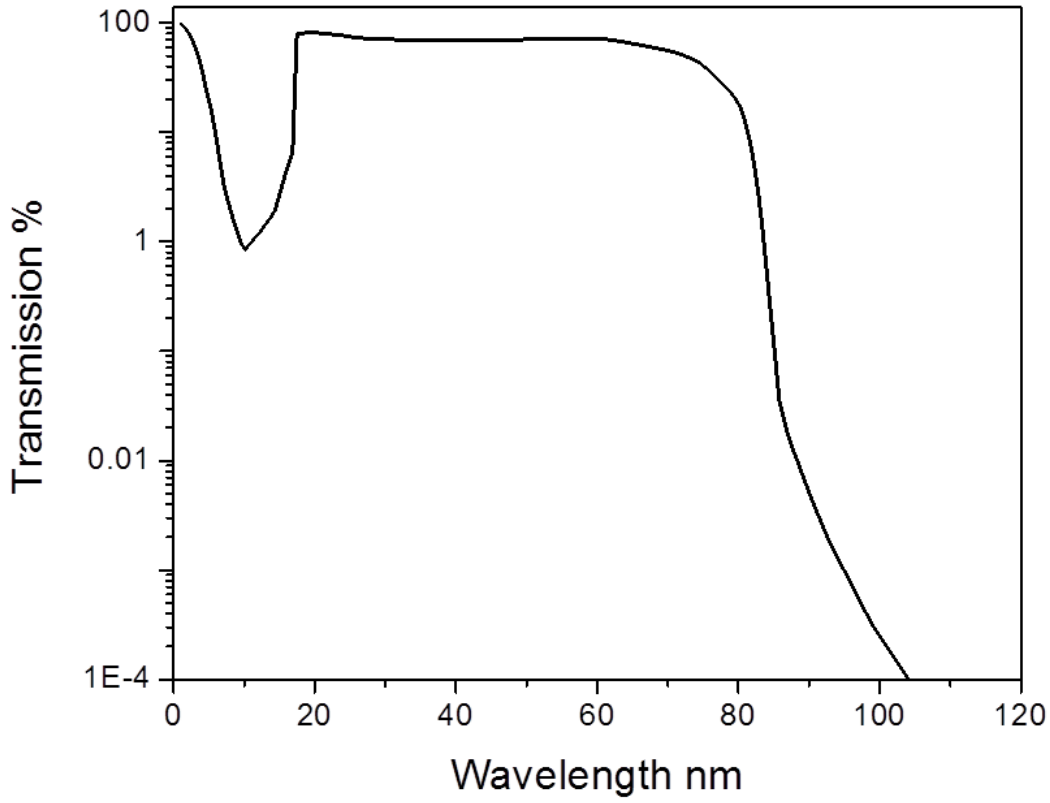

(A)

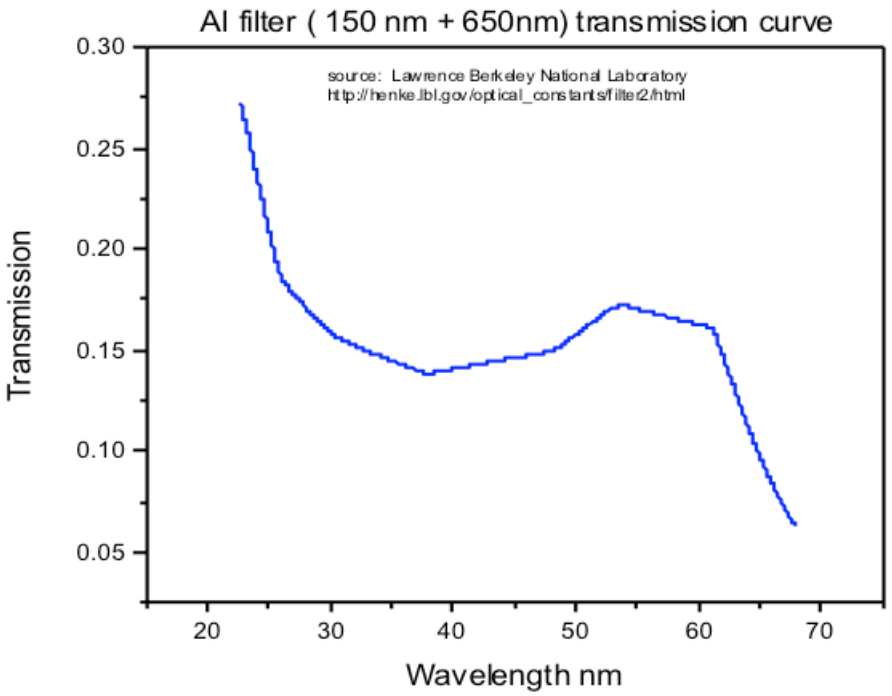
Al filter (150 nm + 650nm) transmission curve
source: Lawrence Berkeley National Laboratory
http://henke.lbl.gov/optical_constants/filter2.html
Transmission
0.30
0.25
0.20
0.15
0.10
0.05
20
30
40
50
60
70
Wavelength nm

(B)

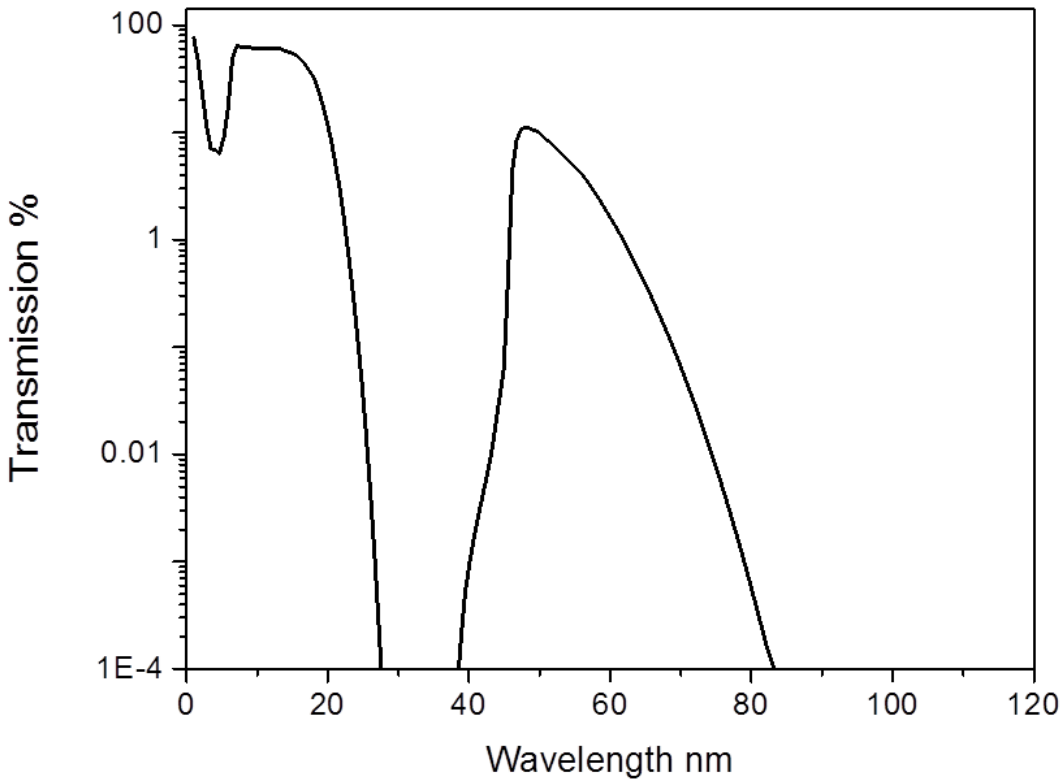

(C)

Figures 3A-F. The system to maintain continuous ignition of injected molten silver and record the UV spectrum. (A). Side view. (B). Top view. (C). Optical table setup. (D). Optical table setup dimensions. (E). Top view. F. Ignition components.

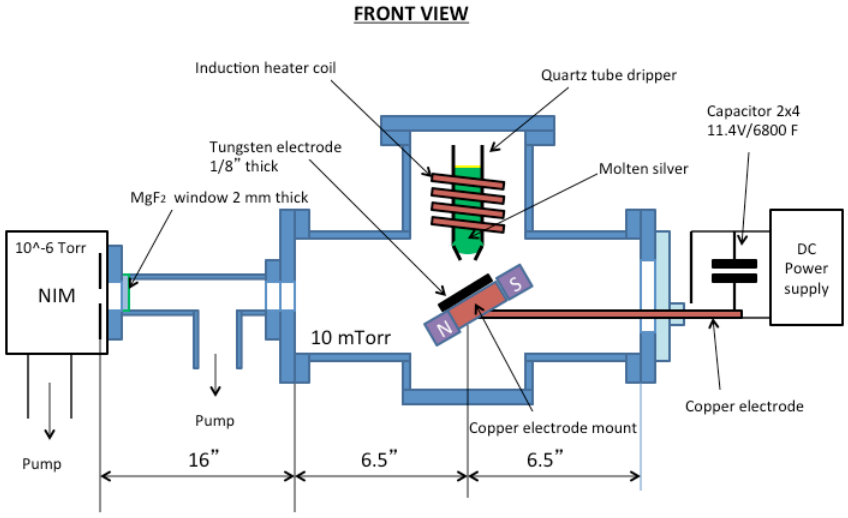

(A)

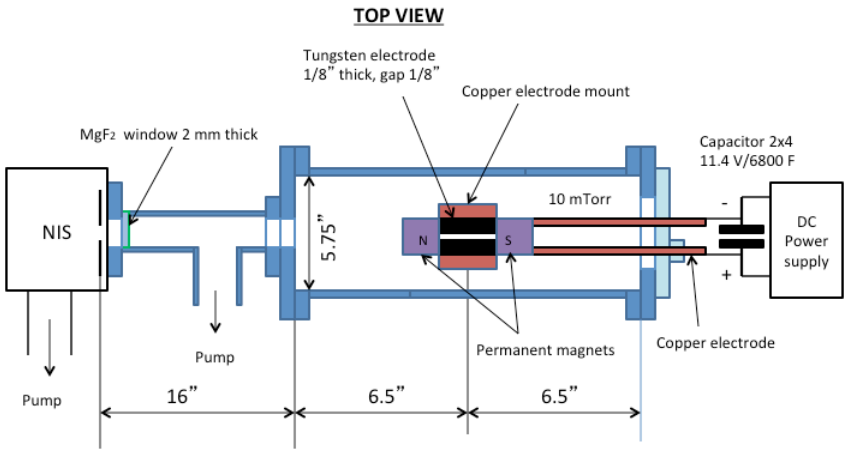

(B)

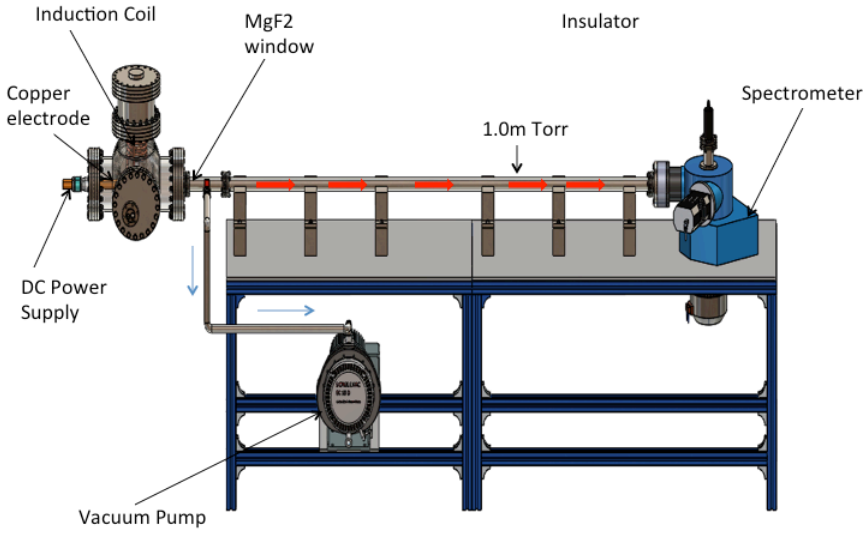
Induction Coil
MgF2
window
Insulator
Copper
electrode
Spectrometer
1.0m Torr
DC Power
Supply
Vacuum Pump

(C)

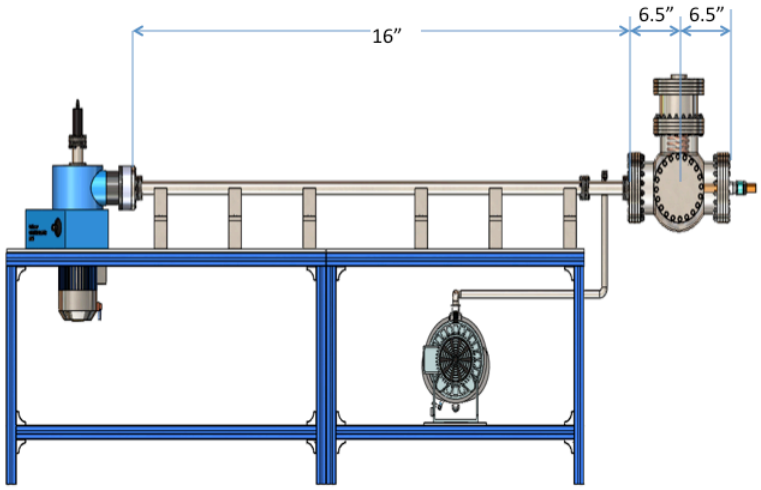
16”
6.5”
6.5”

(D)

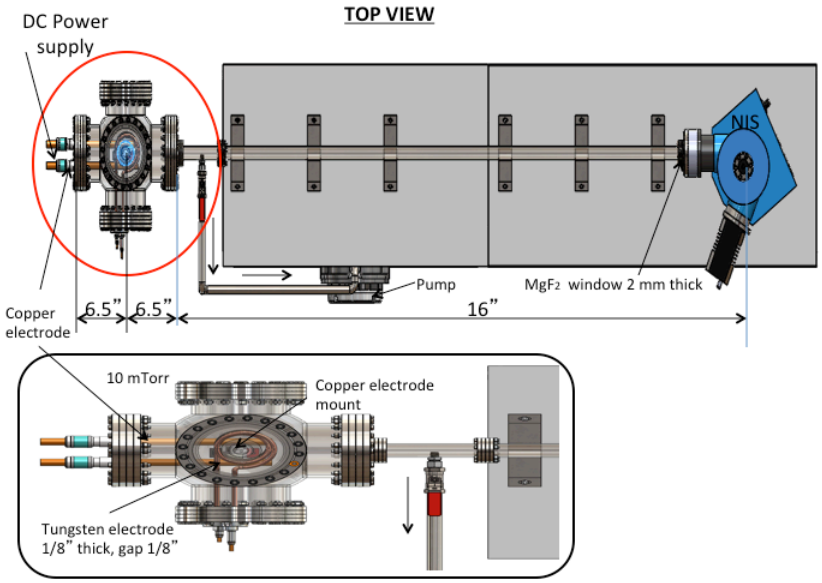
TOP VIEW
DC Power supply
NIS
Pump
MgF2 window 2 mm thick
Copper electrode
6.5”
6.5”
16”
10 mTorr
Copper electrode mount
Tungsten electrode 1/8” thick, gap 1/8”

(E)

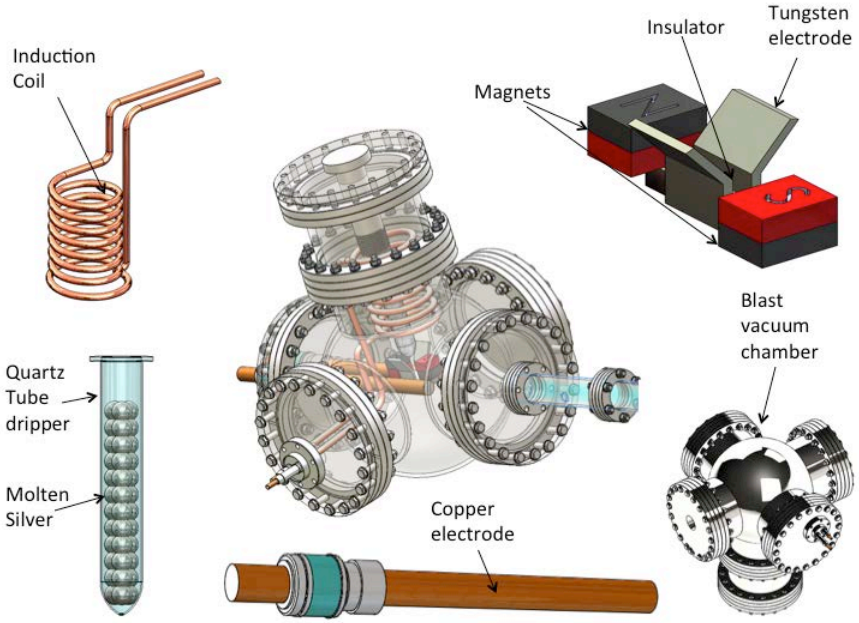
Induction Coil
Insulator
Tungsten electrode
Magnets
Blast vacuum chamber
Quartz Tube dripper
Molten Silver
Copper electrode

(F)

Figure 4. The setup of the Parr 1341 calorimeter used for the energy balance determination.

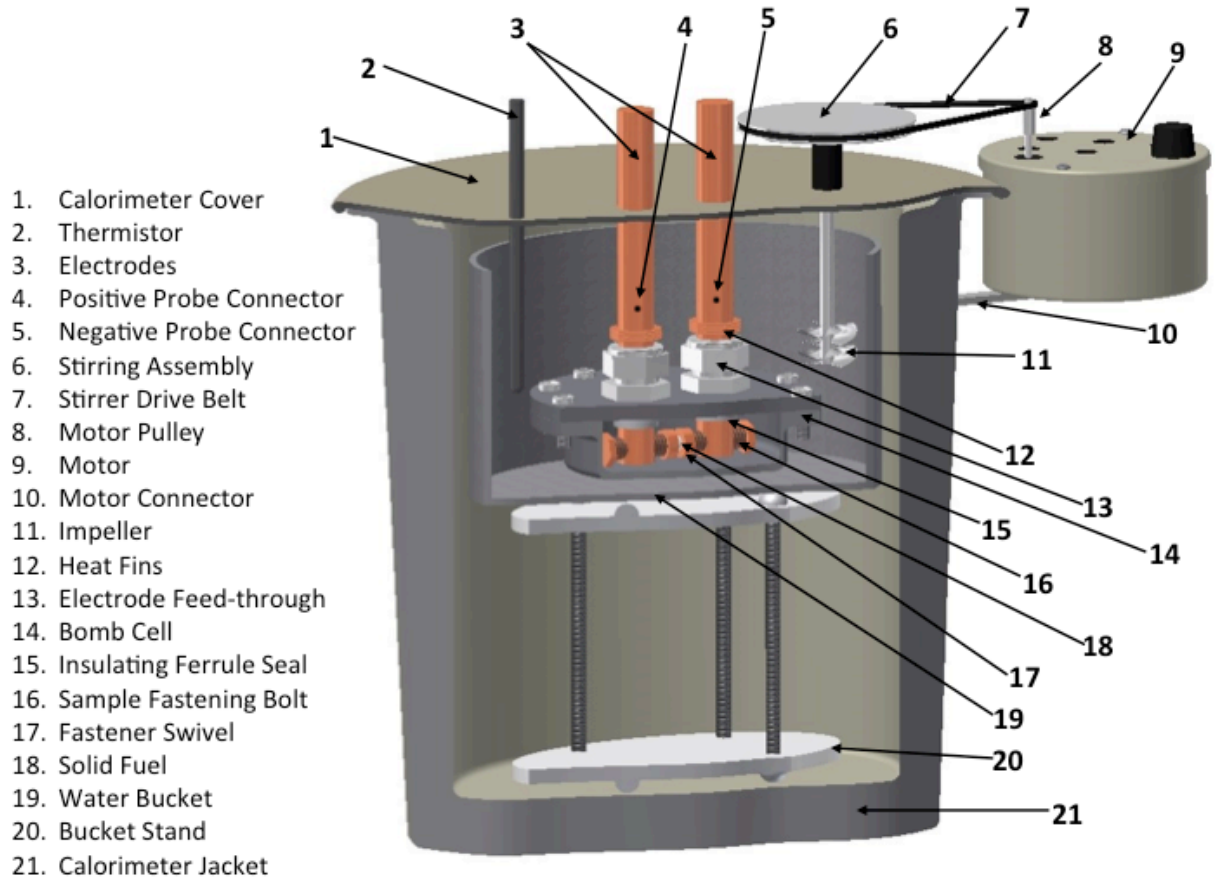

Figure 5. Experimental system to initiate and determine the detonation shockwave speed and pressure.

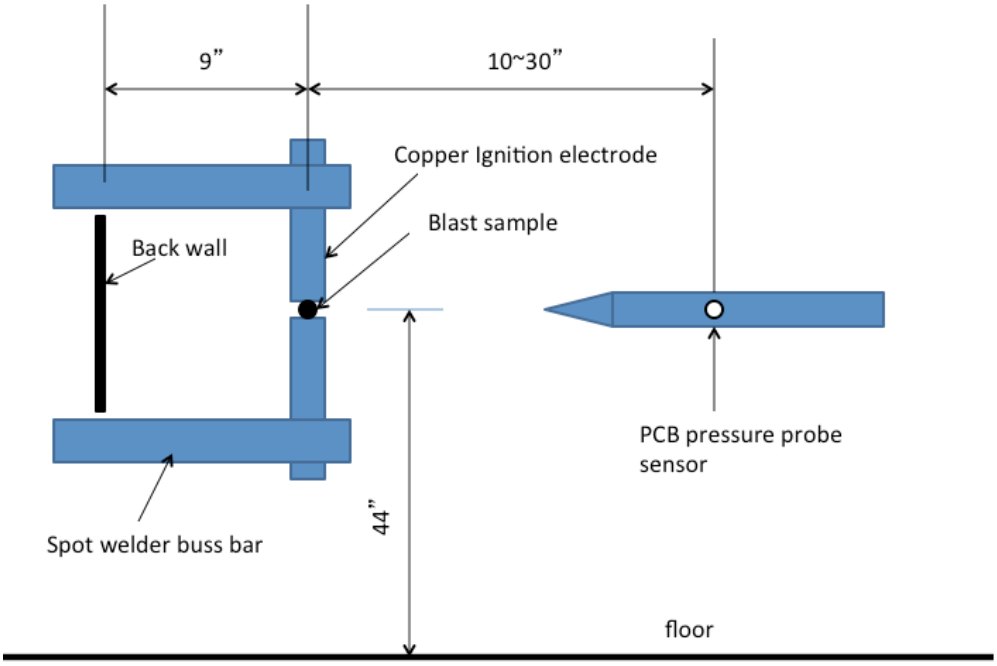

Figure 6. Photo of the experimental system to initiate and determine the detonation shockwave speed and pressure.

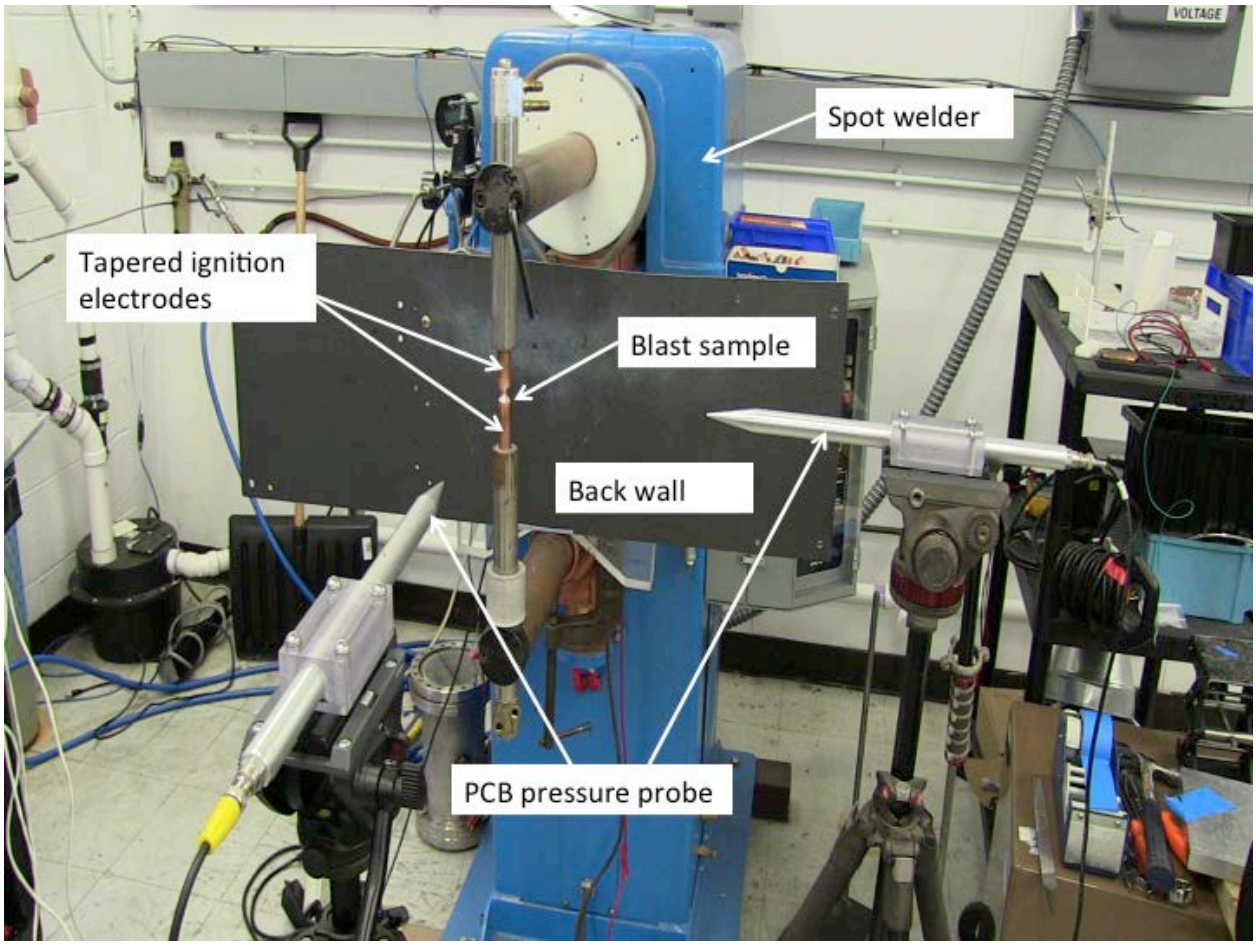

Figure 7. Mercury argon wavelength calibration spectrum (Model: Ocean Optics HG-1) in the 200-800 nm wavelength range.

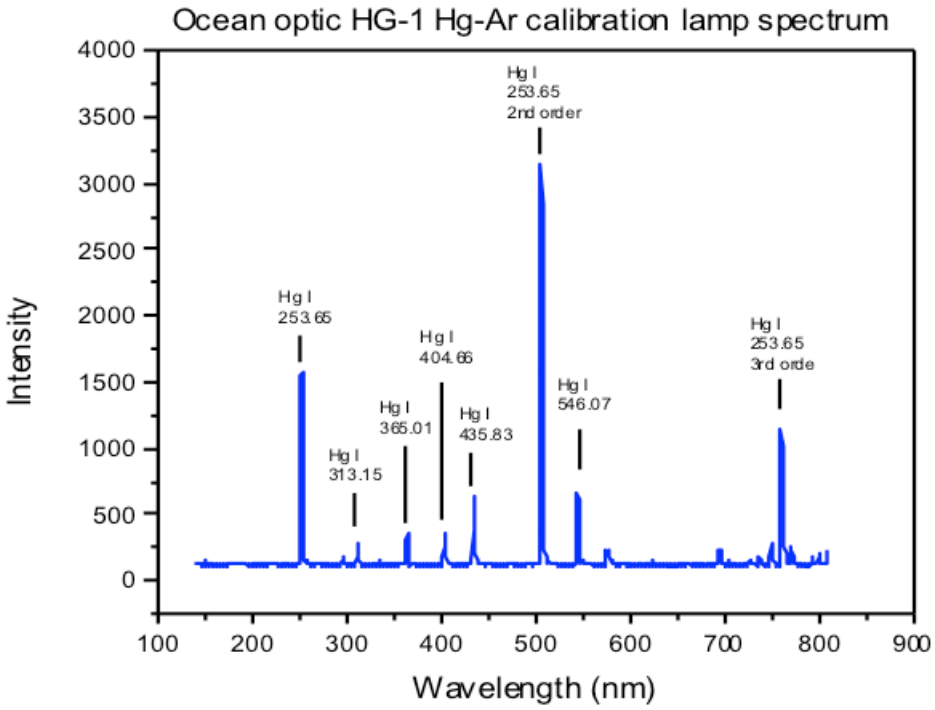

(A)

Figure 8. The NIST traceable quartz tungsten halogen lamp spectrum acquired on the Mightex UV-Vis spectrometer.

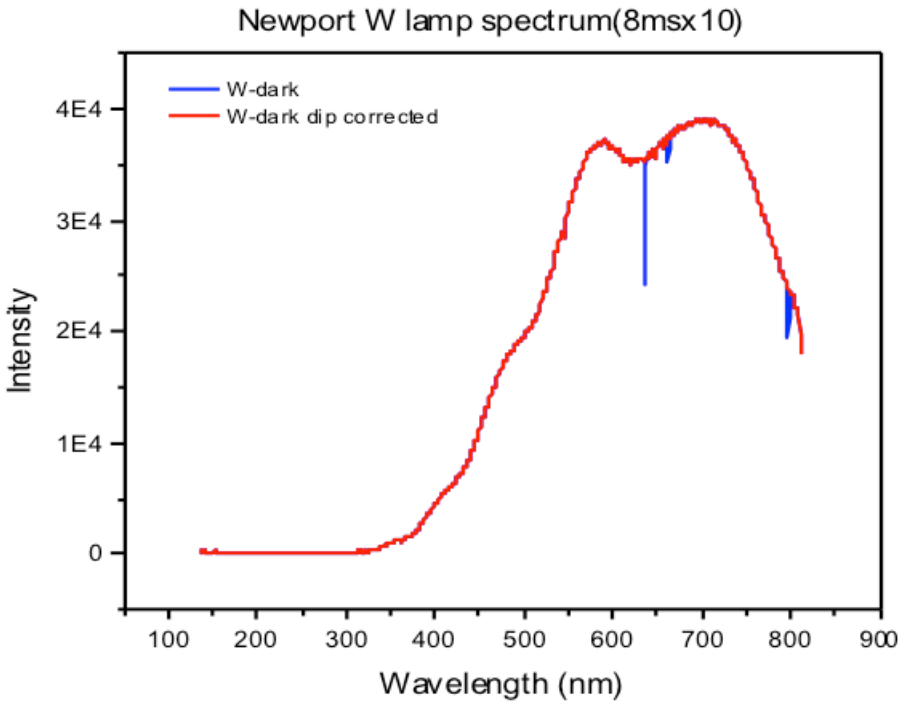

Figure 9. The NIST traceable quartz tungsten halogen lamp standard spectral irradiance.

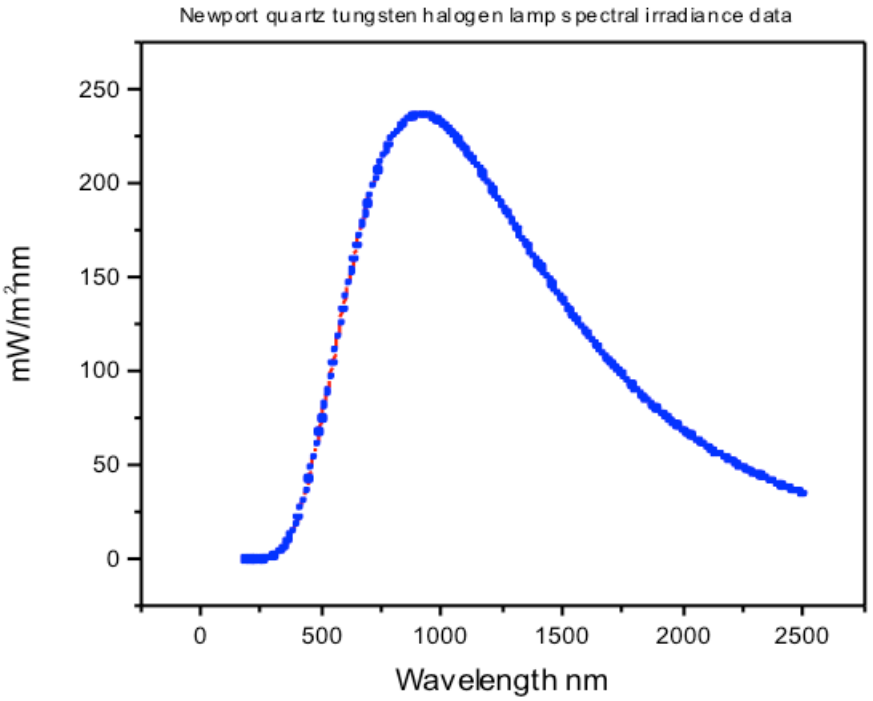

Figure 10. The NIST traceable Gooch & Housego deuterium lamp acquired on the Mightex UV-Vis spectrometer.

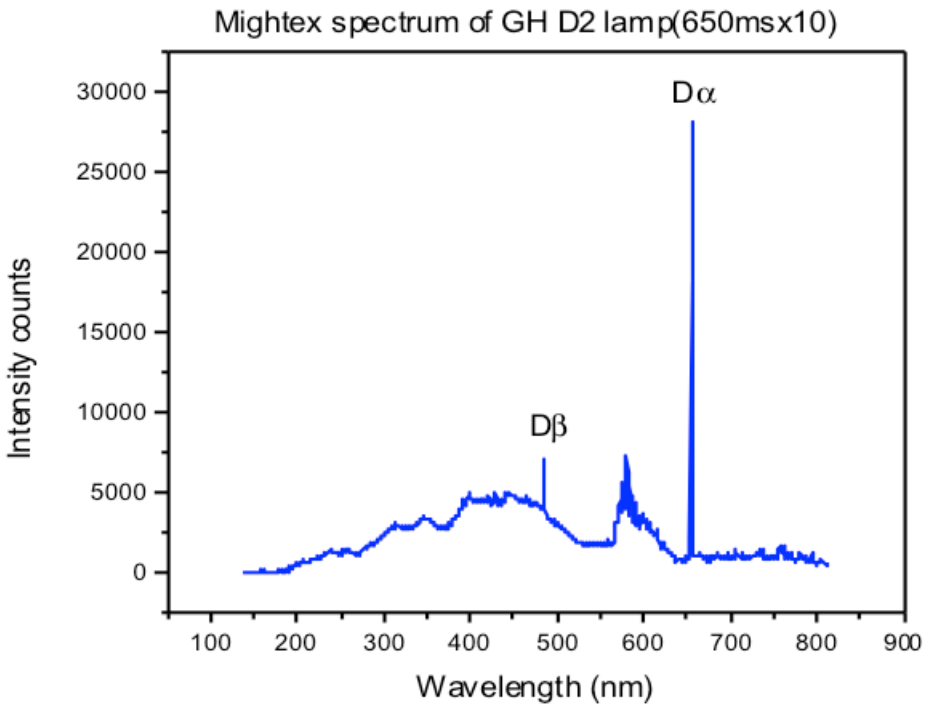

Figure 11. The NIST traceable Gooch & Housego deuterium standard irradiance.

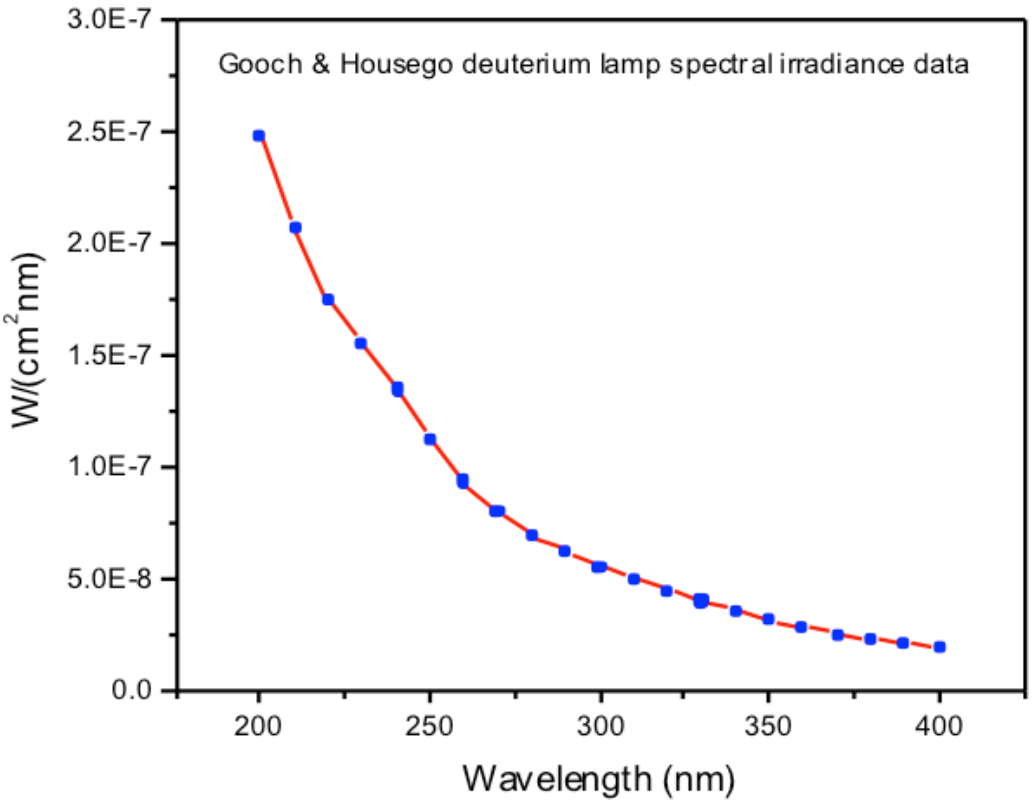

Figure 12. The Mightex UV-Vis spectrometer efficiency spectrum C_p (mJ/count) versus wavelength obtained from the NIST traceable quartz tungsten halogen lamp and the NIST traceable Gooch & Housego deuterium lamp.

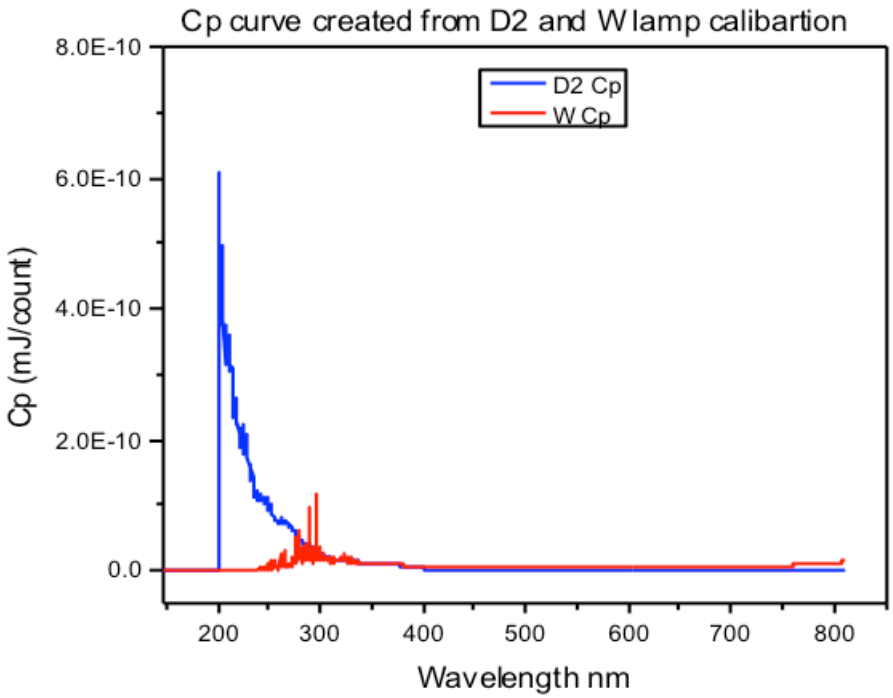

Figure 13. Superimposed NIST traceable Gooch & Housego deuterium lamp and NIST traceable quartz tungsten halogen lamp intensity calibration curves with region of overlap to stitch the curves.

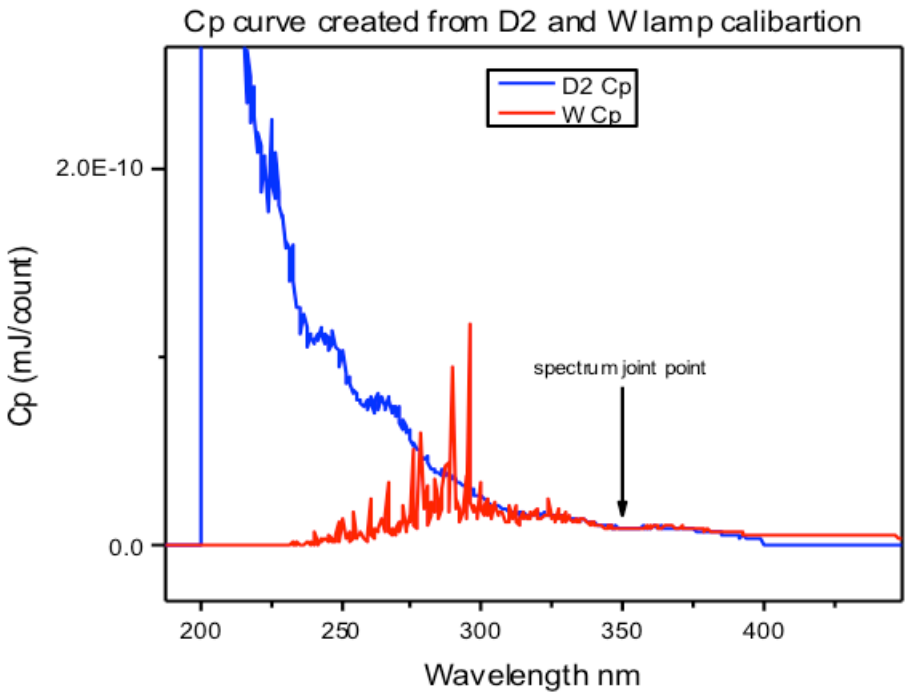

Figure 14. The final spectrometer efficiency spectrum C_p over the 200 nm to 800 nm region.

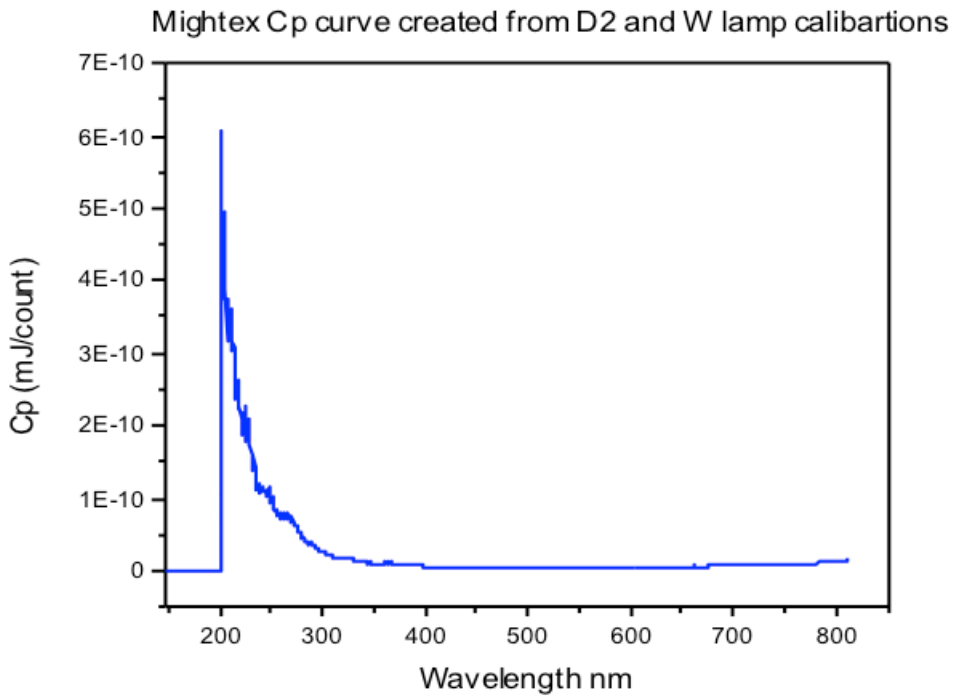

Figure 15. Superimposed Mightex UV-Vis (200-815.4 nm) spectra of the emission from five shots.

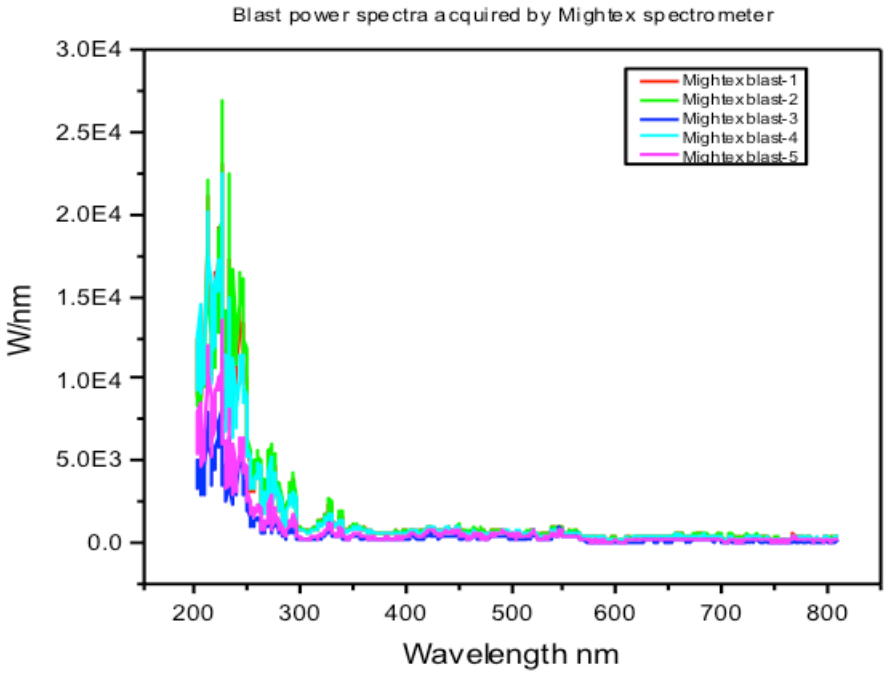

Figure 16. The transmission curve of the MgF_2 window on the entrance to the Mightex UV-Vis and NIS spectrometers, the reflectance of the NIS 300G Al-MgF_2 coated grating, and the Andor provided CCD camera quantum efficiency curve as a function of wavelength.

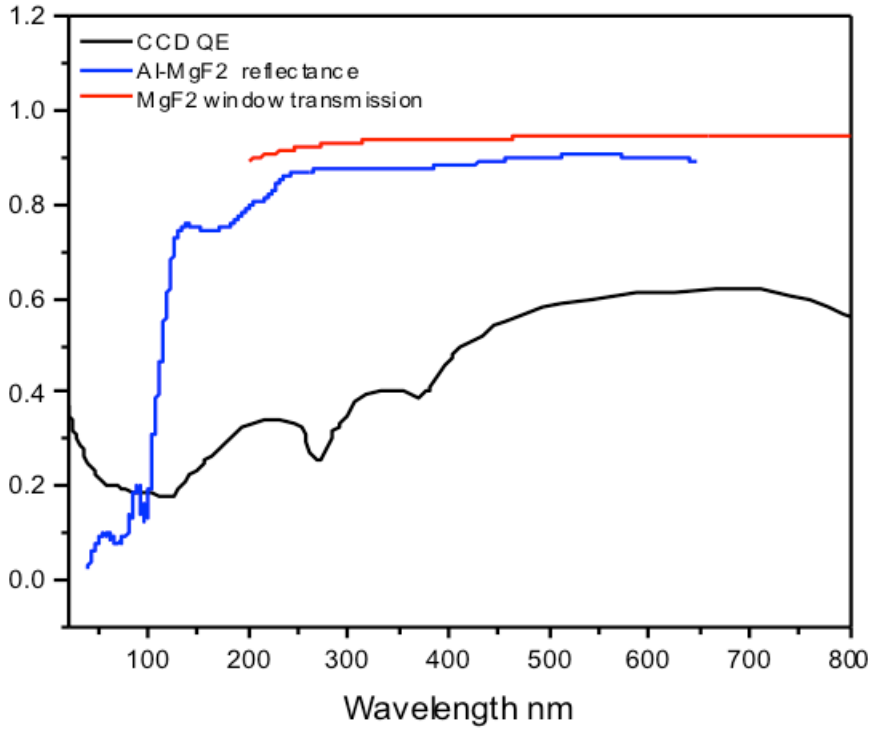

Figures 17A-B. EUV spectra recorded with the GIS that were used for wavelength calibration. A. A high voltage discharge of air wherein the positions of known oxygen and nitrogen ions were used. B. Helium microwave plasma wherein helium atom and ion lines were used.

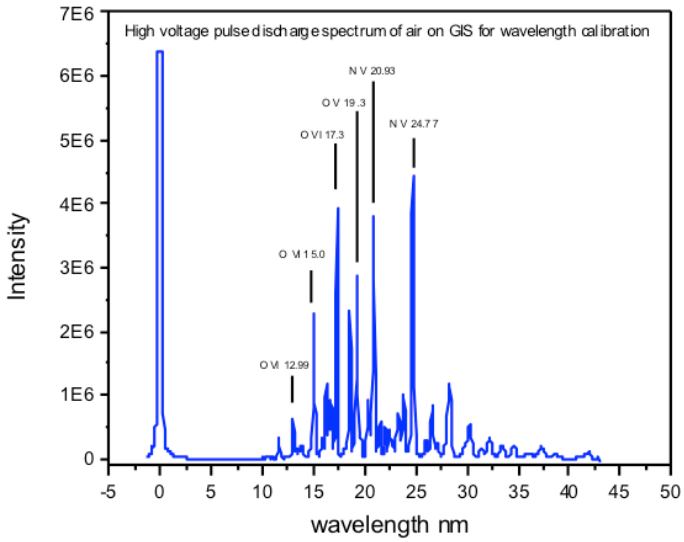

(A)

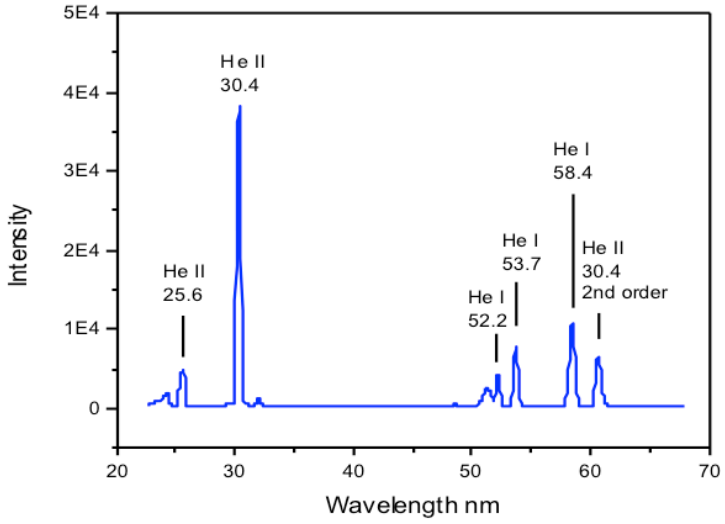

(B)

Figure 18. Superimposed EUV spectra (22-647 nm) with the CCD centered at different positions acquired using the (i) GIS, 0.8 um Al filter, no window, and CCD centered at 55 nm (black curve), (ii) NIS, no window, and CCD centered at 200 nm (blue curve), (iii) NIS, MgF_2 window, and CCD centered at 500 nm (light blue curve), (iv) NIS, MgF_2 window, and CCD centered at 400 nm, (green curve), and (v) NIS, MgF_2 window, and CCD centered at 300 nm (red curve).

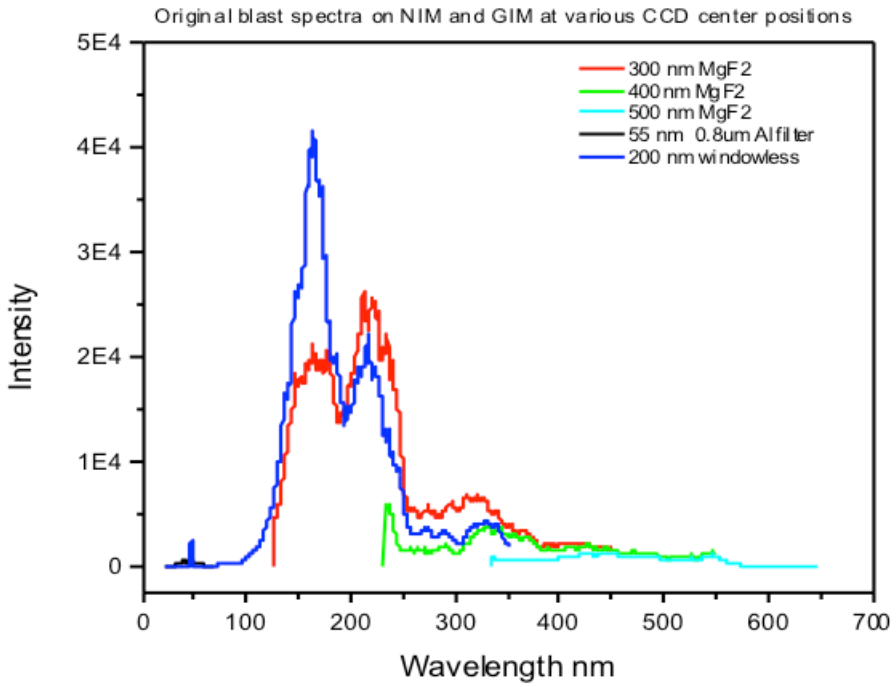

Figure 19. Matching the intensities of the GIS and NIS spectra shown in Figure 18 at overlapping spectral wavelengths were used to join curves.

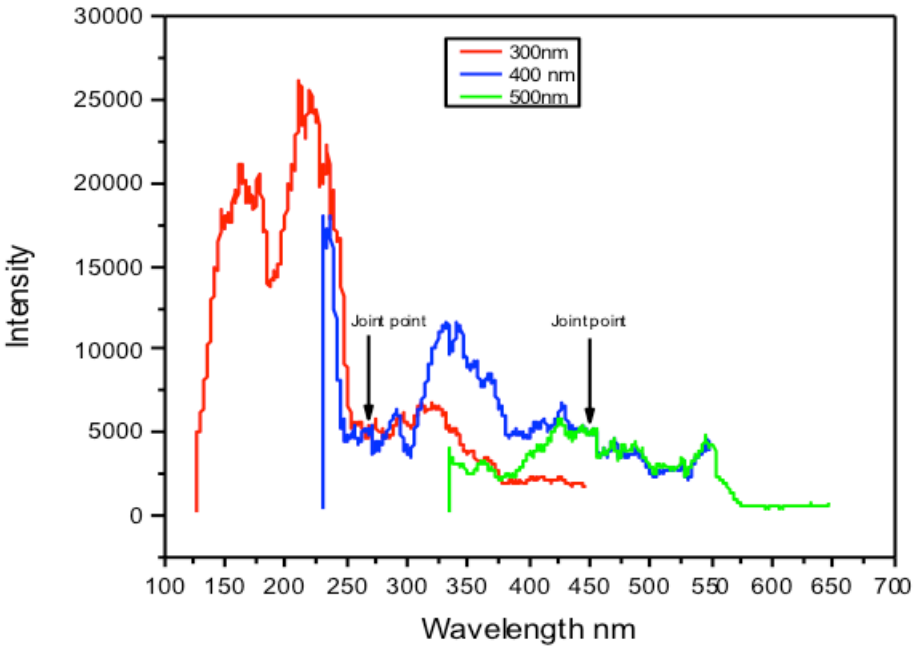

Figure 20. The joined spectra (200-640 nm) shown in Figure 19 were corrected for the attenuation by the MgF_2 window.

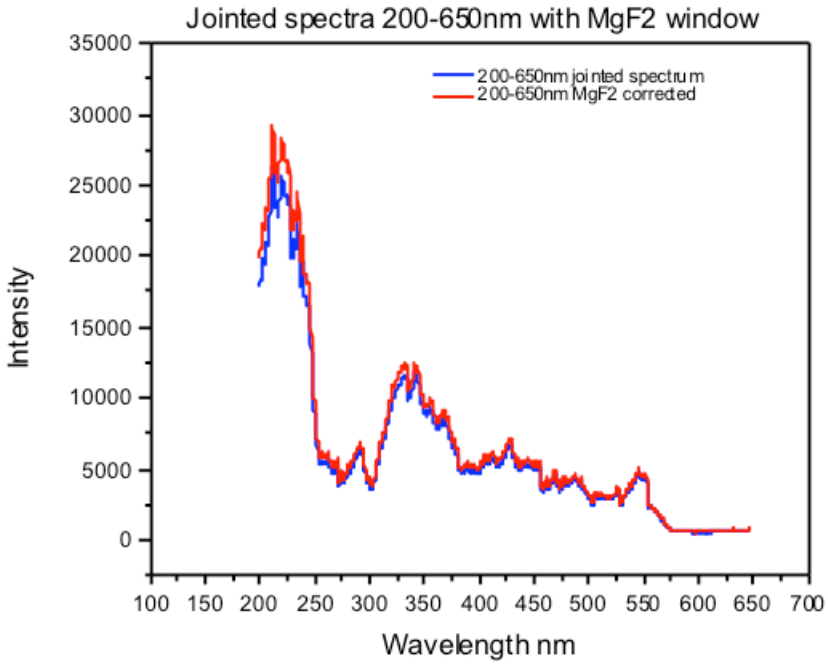

Figure 21. The joined spectra (10-640 nm) shown in Figure 19 were corrected for the attenuation by the MgF_2 window.

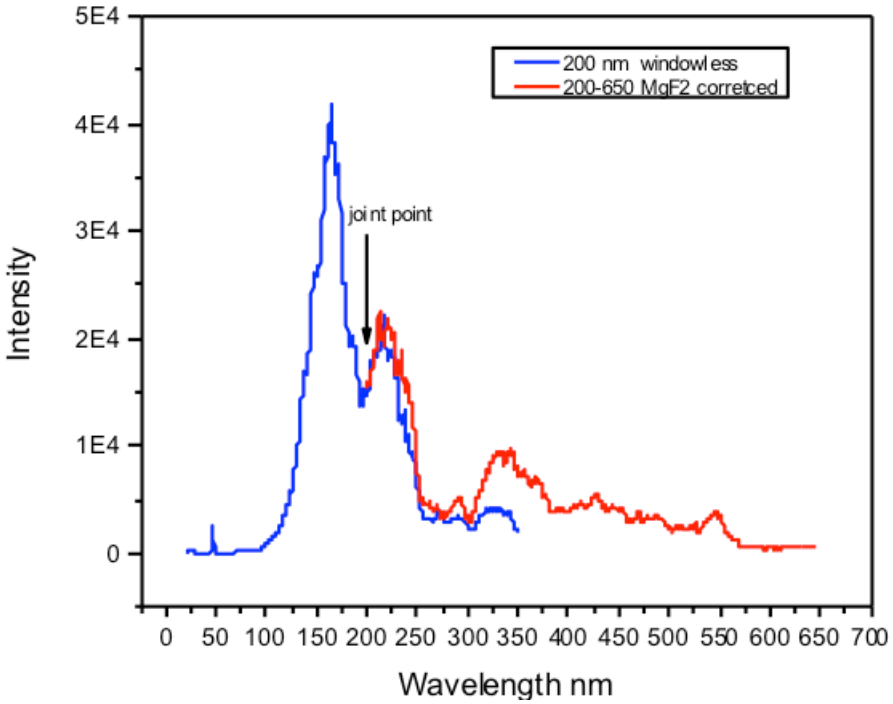

Figure 22. The NIS joined window corrected spectrum (50-650 nm) from the spectra of Figures 20 and 21.

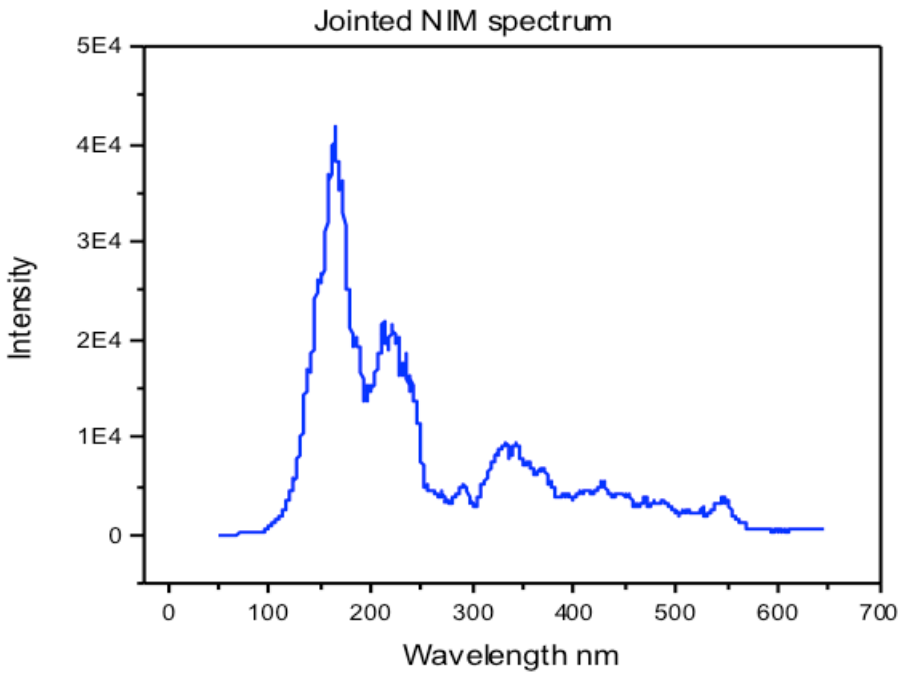

Figure 23. The NIS spectrum (50-650 nm) of Figure 22 corrected for the reflectance of the NIS 300G Al-MgF_2 coated grating.

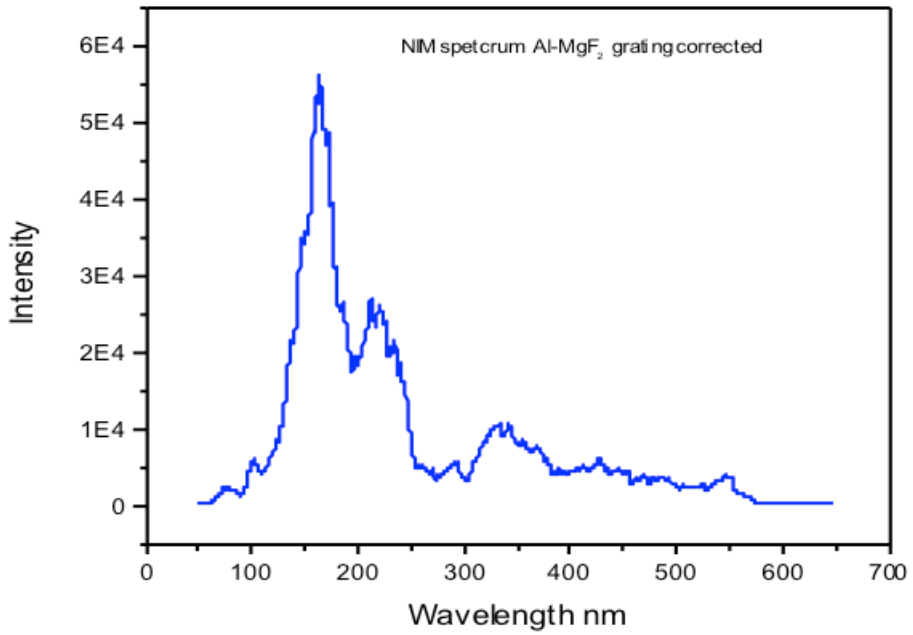

Figure 24. The shot blast emission spectrum (20-65 nm) recorded on the GIS with the CCD centered 55 nm using no MgF_2 window.

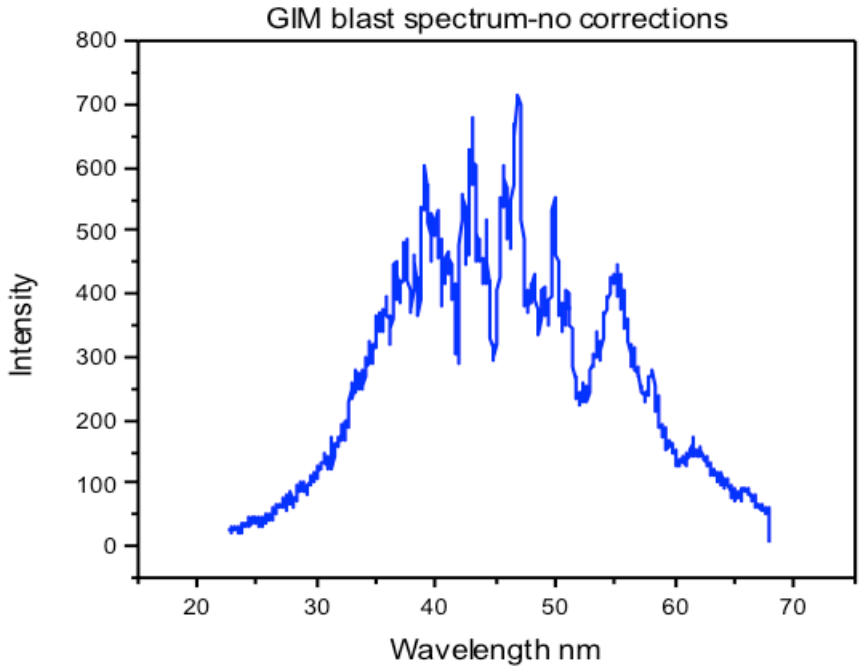

Figure 25. The GIS spectrum corrected for the Al filter.

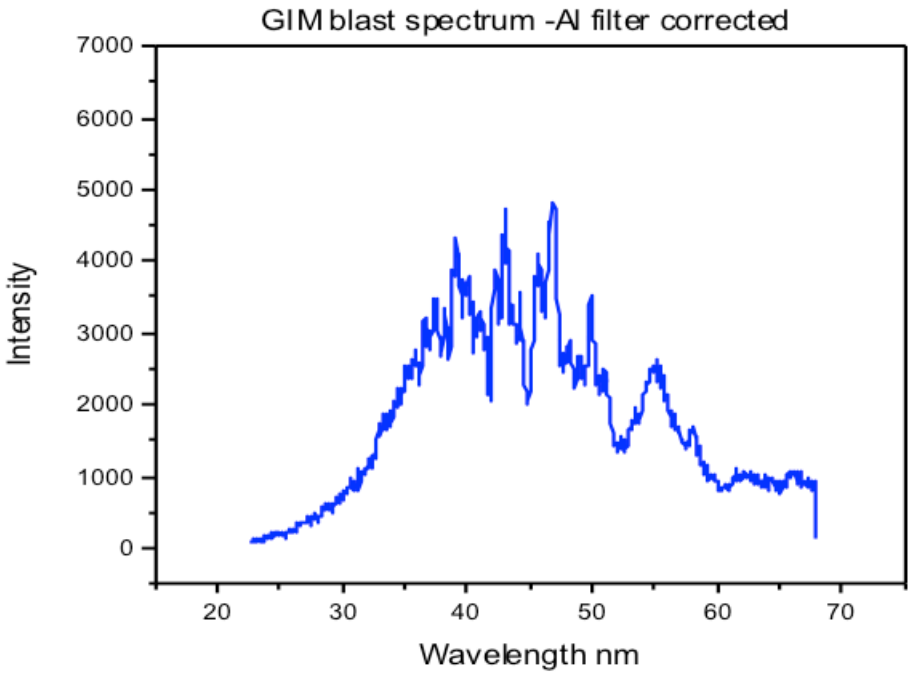

Figure 26. The manufacturer provided efficiency curve of the gold-coated GIS grating.

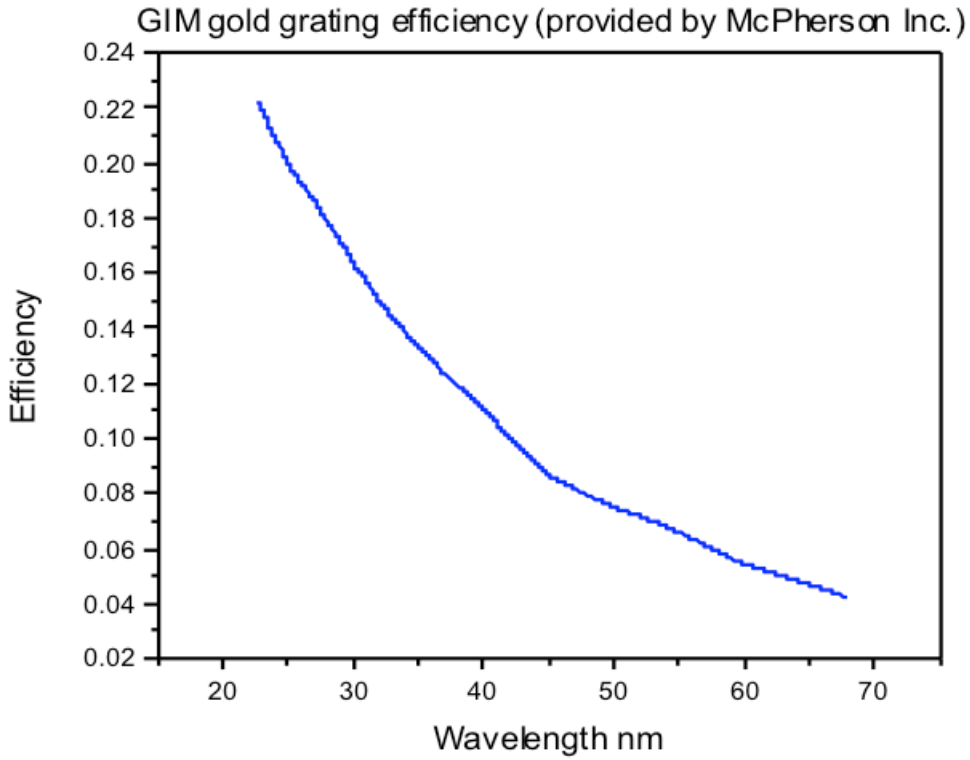

Figure 27. The GIS spectrum (20-65 nm) corrected for the efficiency of the gold-coated GIS grating.

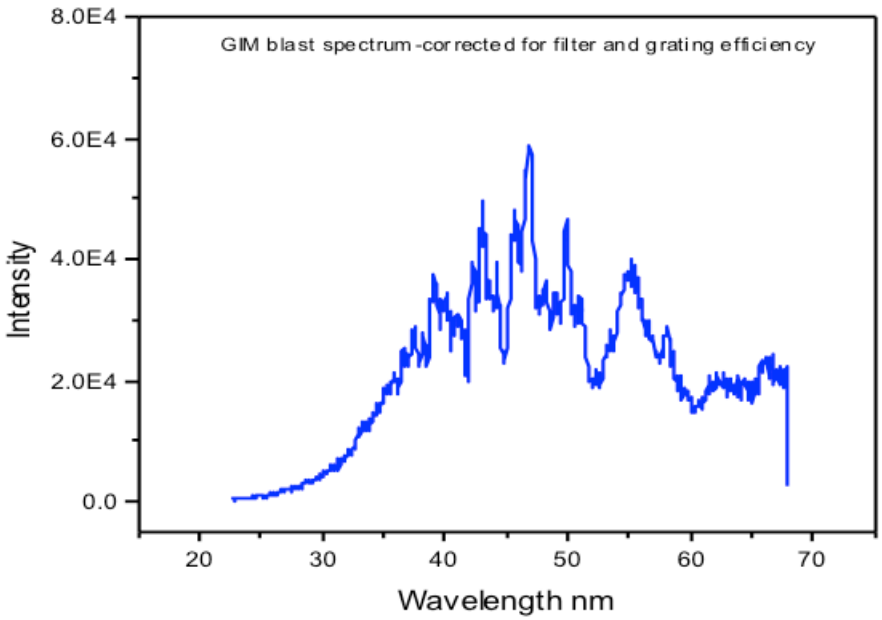

Figures 28A-B. The superimposed scaled and corrected NIS spectrum (50-650 nm) of Figure 23 and GIS spectrum (20-65 nm) to be joined at about 67 nm. A. 20-650 nm wavelength range. B. 60-75 nm wavelength range.

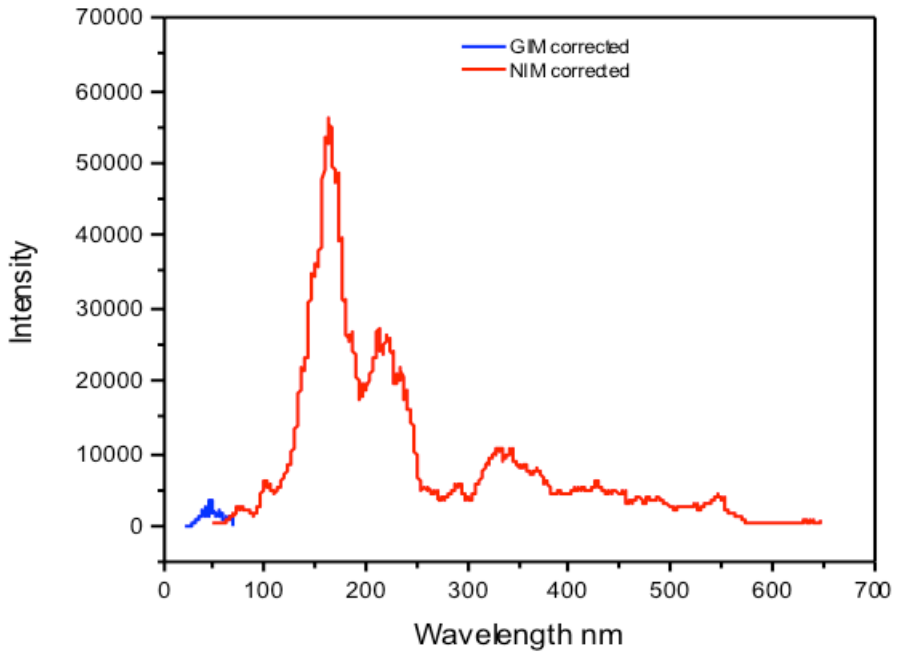

(A)

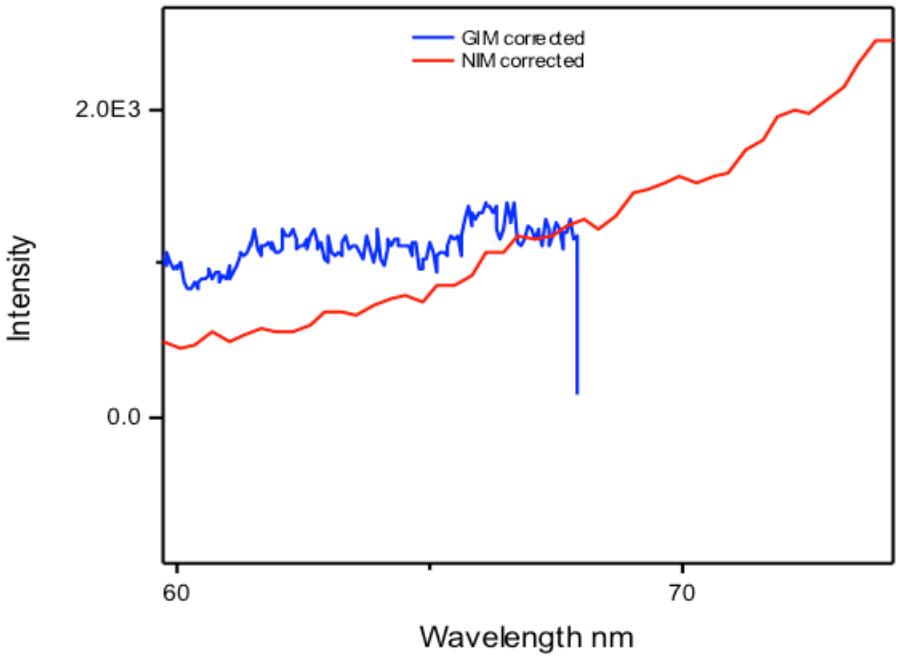
GIM corrected
NIM corrected
2.0E3
0.0
Intensity
60
70
Wavelength nm

(B)

Figure 29. The joined GIS and NIS spectrum (20-650 nm).

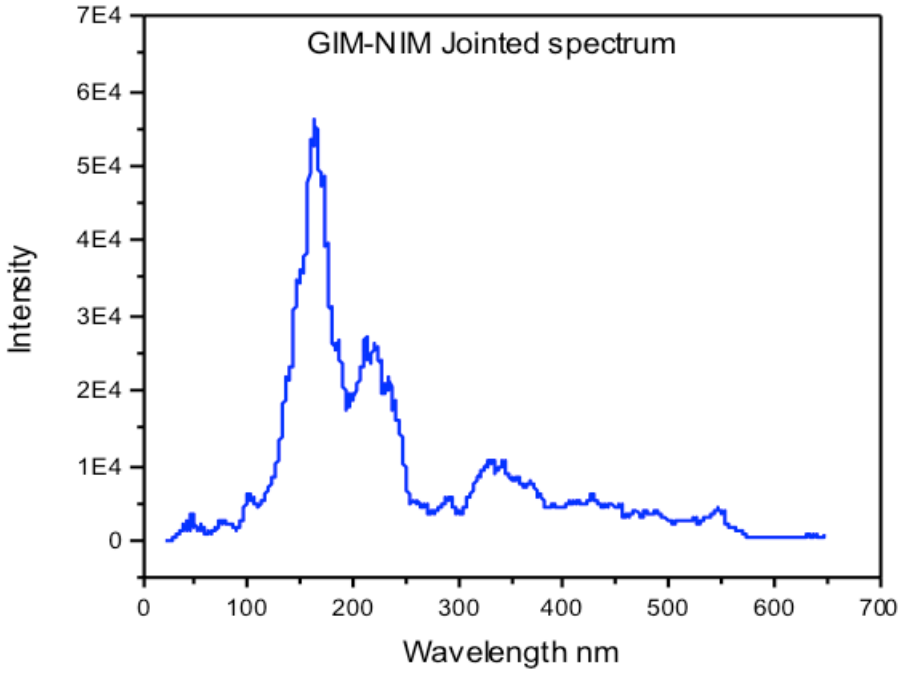

Figure 30. The GIS-NIS spectrum (20-650 nm) corrected for the quantum efficiency of the Andor CCD camera.

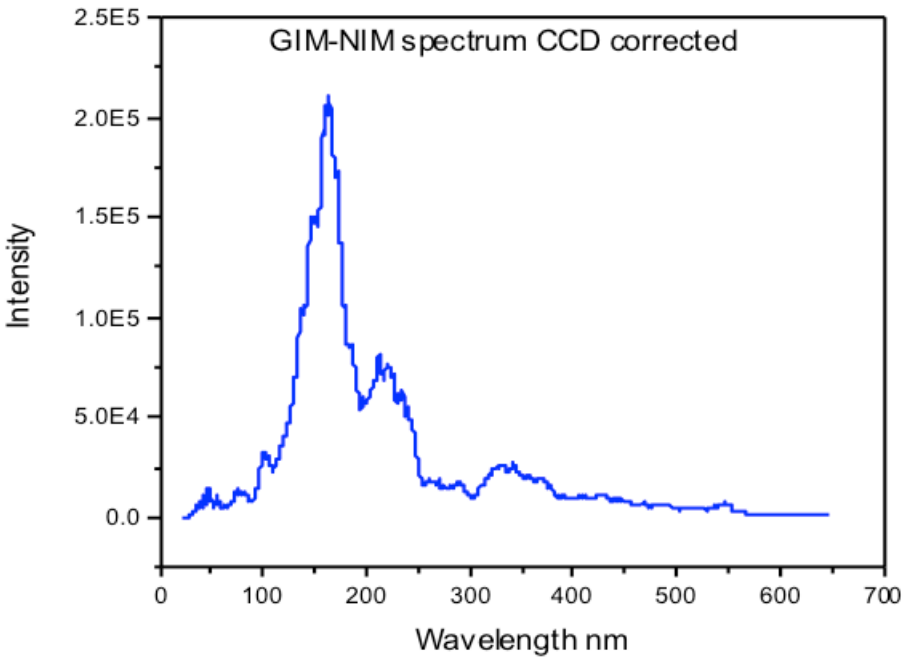

Figure 31. The combined GIS and NIS energy density spectrum (20-650 nm) before power calibration against the absolutely calibrated UV-Vis spectrum wherein the spectral count intensity of the combined GIS and NIS spectra following Al filter, window, grating, and CCD quantum efficiency corrections given in Figure 30 was converted to energy density by multiplying the counts as a function of wavelength by the conversion factor $\frac{hc}{\lambda}$.

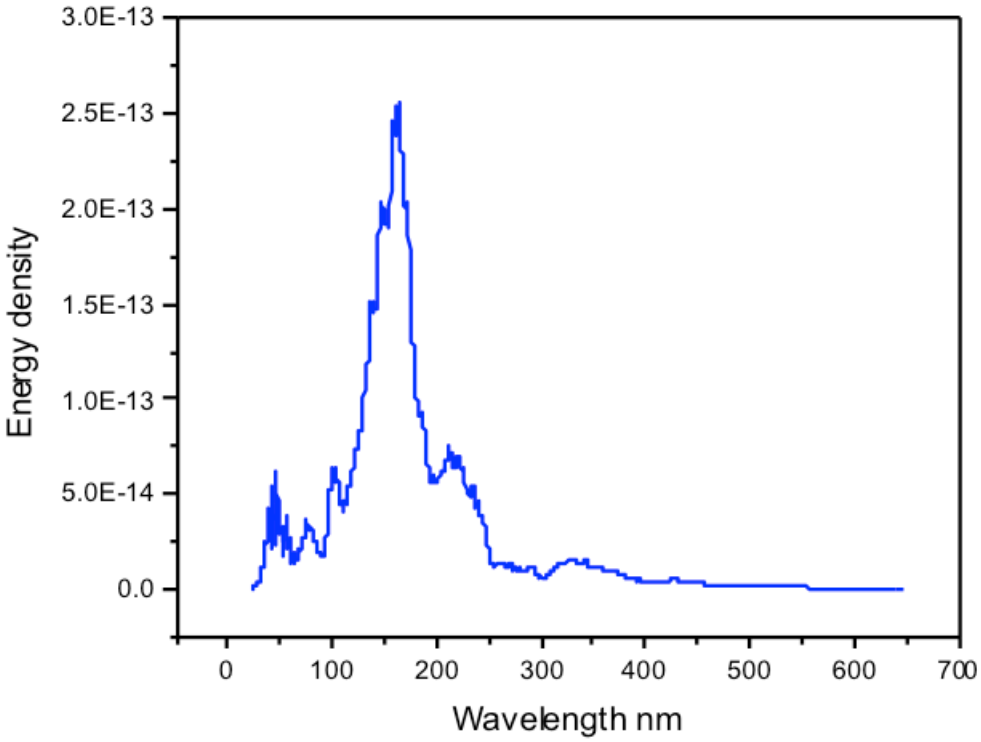

Figure 32. The MgF_2 window corrected blast ignition spectrum recorded by the absolutely calibrated Mightex UV-Vis spectrometer with the superimposed GIS-NIS energy density spectrum of Figure 31 joined at the region of spectral overlap.

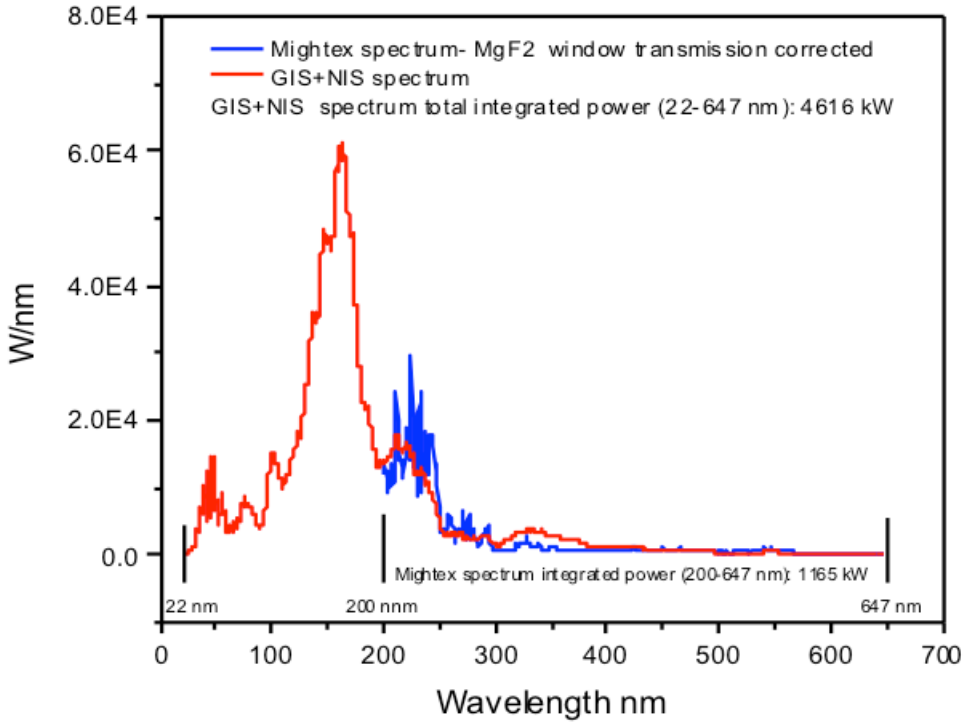

Figure 33. The peak power in the UV-Vis spectral range (200-647 nm) was 4813 kW over 40 us duration which corresponds to 19 MW over 40 us duration over the fully recorded spectral range (200-647 nm). The actual power was estimated to be at least twice that recorded based on scaling unsaturated lines of the saturated power spectrum.

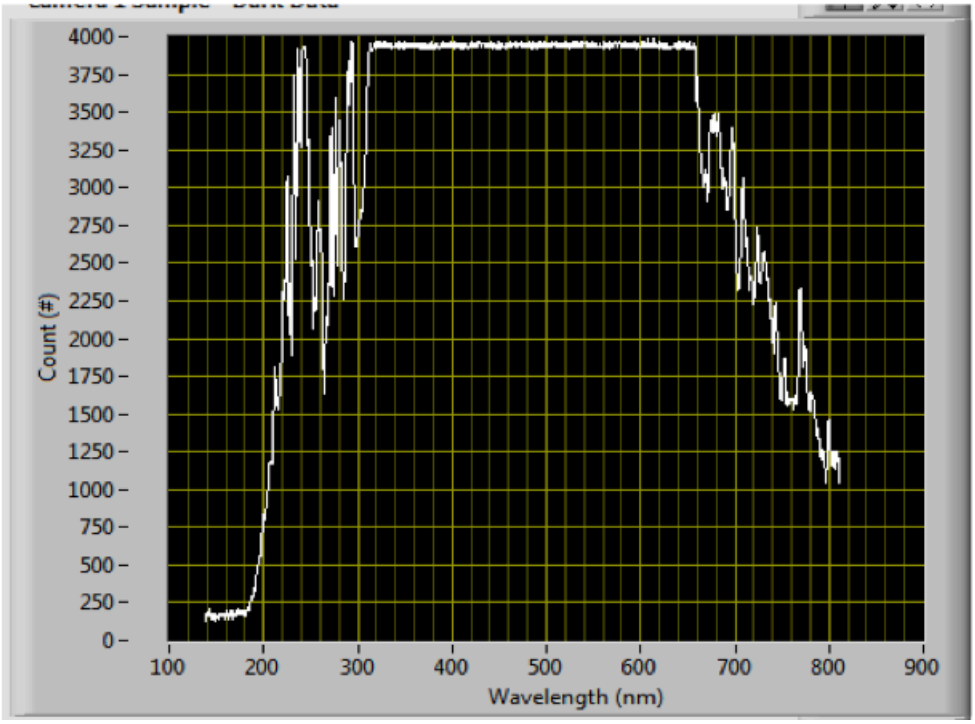

Figure 34. The wavelength calibrated and absolute intensity calibrated spectrum (10-45 nm) of the emission of hydrated silver shots recorded on the GIS with a Zr filter that shows the EUV continuum cutoff at 10.1 nm.

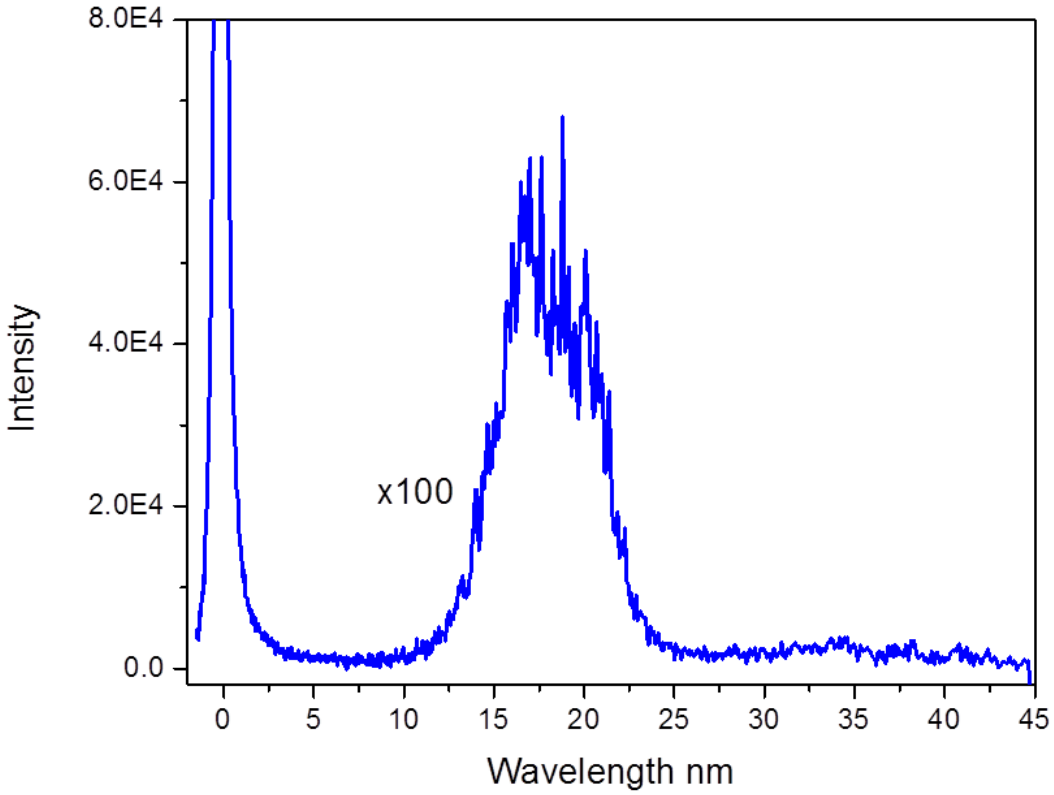

Figure 35. The combined efficiency curve C_p comprising the total correction for the product of components of the transmission curve of the MgF_2 window on the entrance to the Mightex UV-Vis and NIS spectrometers, the reflectance of the NIS 300G Al-MgF_2 coated grating, and the Andor provided CCD camera quantum efficiency curve as a function of wavelength.

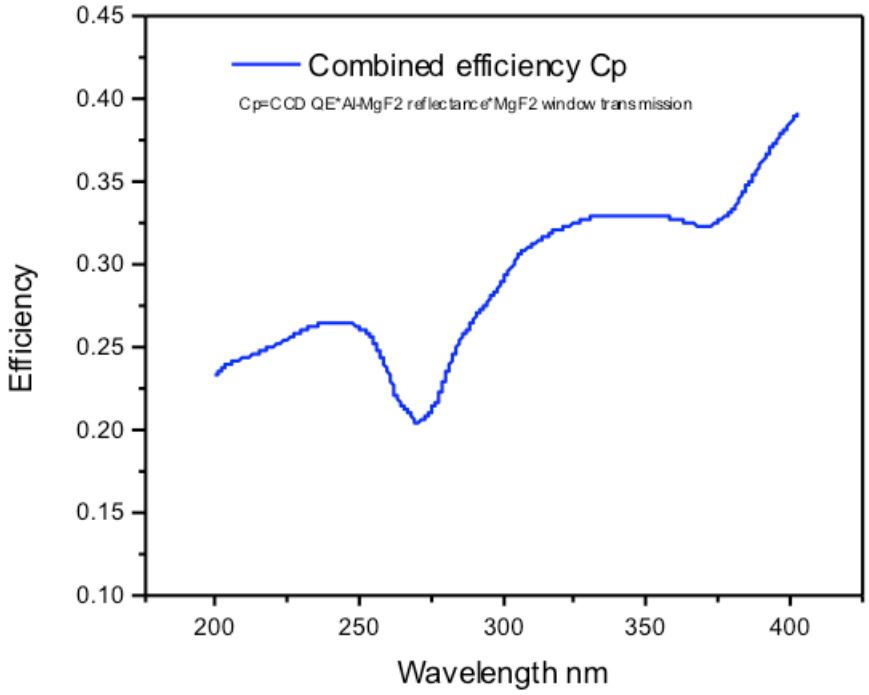

Figure 36. The G-H NIST D_2 lamp spectrum (150-450 nm) recorded on the NIS.

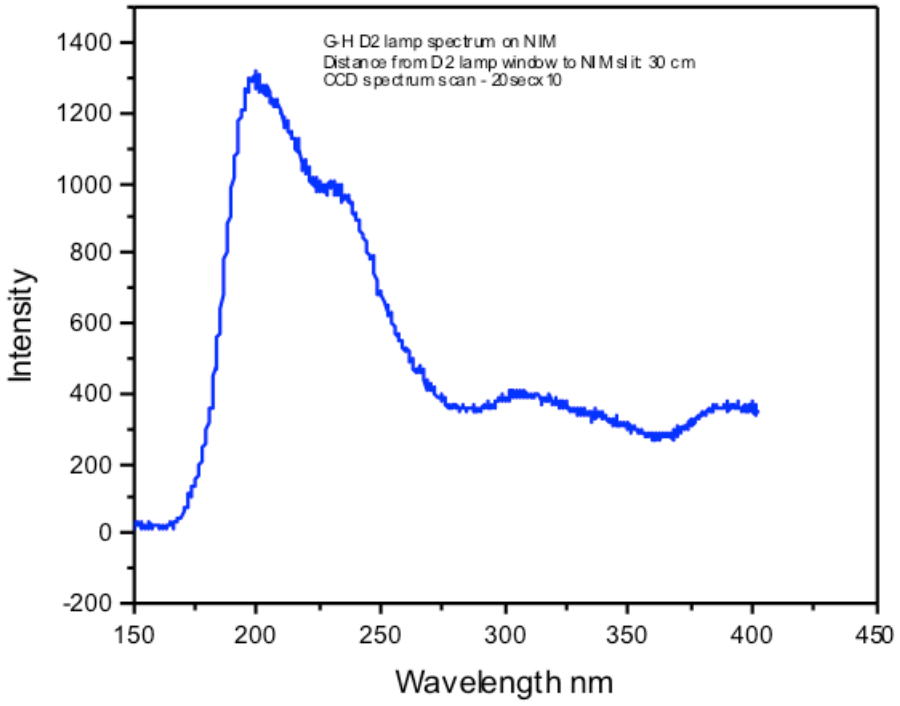

Figure 37. The optical element corrected NIS spectrum superimposed on the deuterium standard irradiance (Figure 11). The match is very good, confirming the optical element correction method.

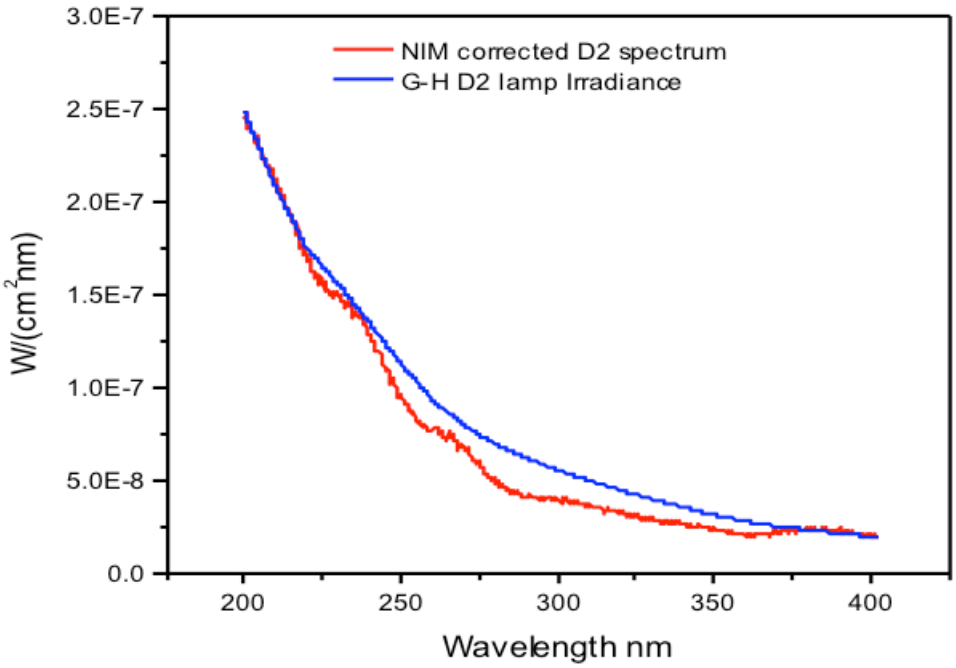

Figure 38. The comparison of the intensity of the L7293 D_2 lamp and the G-H NIST D_2 lamp showing that the L7293 D_2 lamp has a higher irradiance than the G-H NIST D_2 lamp at the same distance.

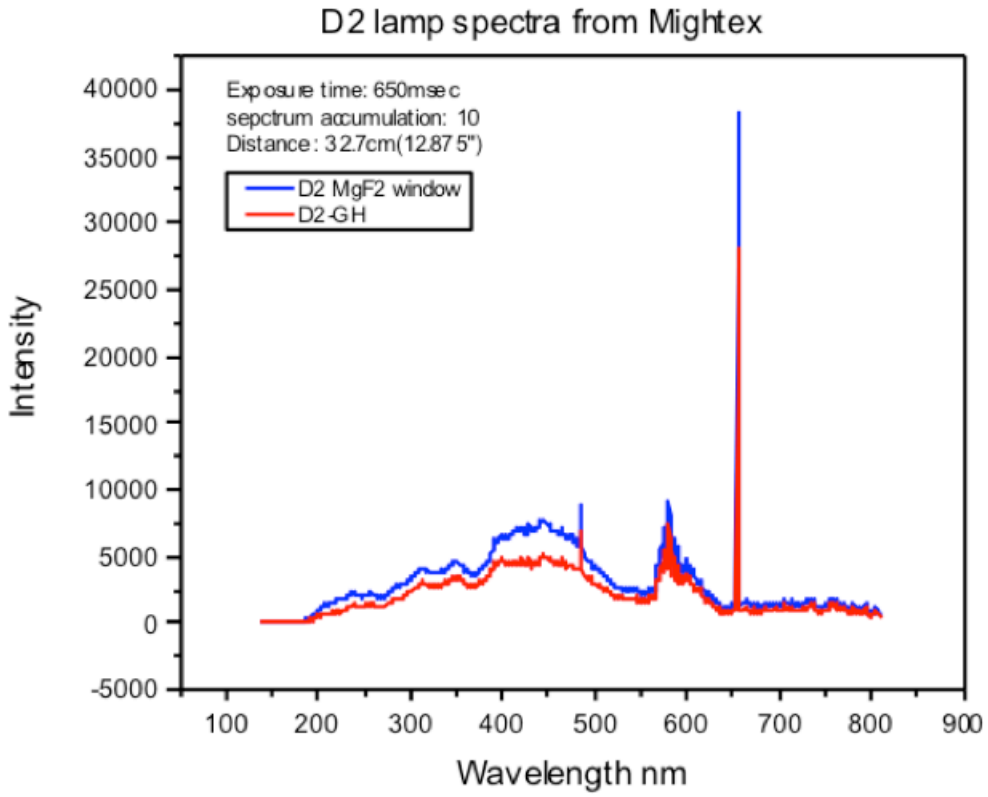

Figure 39. The Mightex power spectrum of the L7293 D_2 lamp, the G-H NIST D_2 lamp, and the NIST D_2 irradiance.

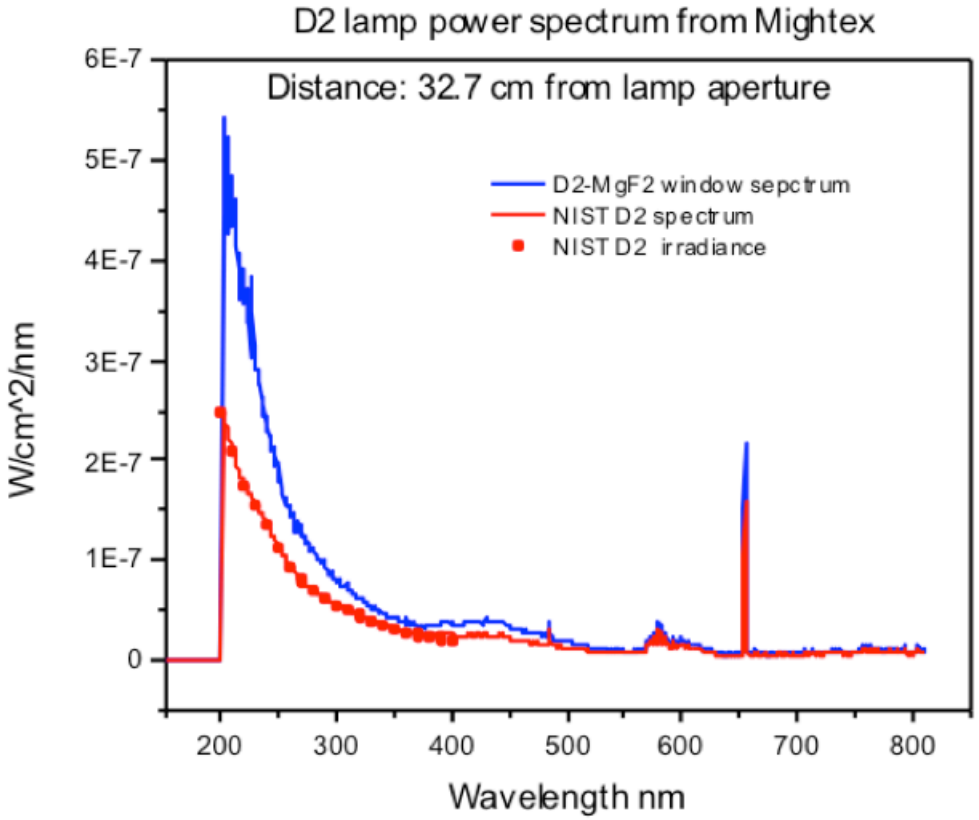

Figure 40. The L7293 D_2 lamp NIS spectrum and the corresponding spectrum corrected by using the Al-MgF_2 reflectance and CCD QE curves.

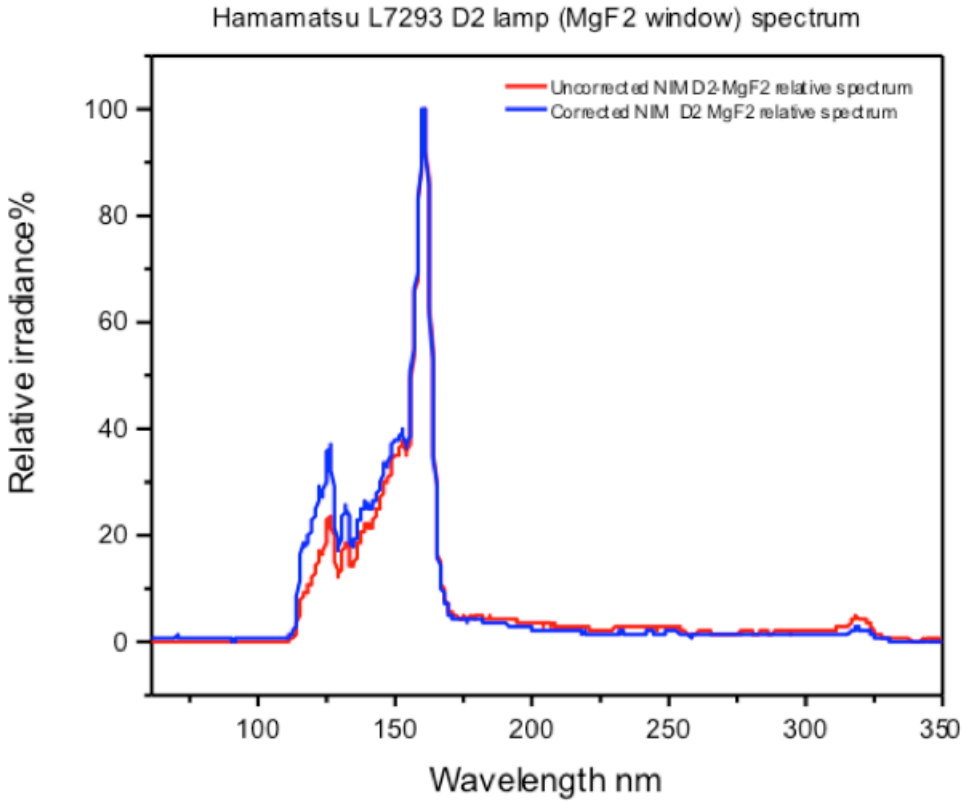

Figure 41. The Mightex G-H NIST D_2 lamp NIS spectrum that comprised the Mightex absolute calibration spectrum overlaid with the Al-MgF_2 reflectance and CCD QE corrected L7293 D_2 lamp spectrum that was scaled to stitch with the calibration spectrum in the regions of common wavelengths. Second order NIM lines such as the second order of the 163 nm EUV peak were observed.

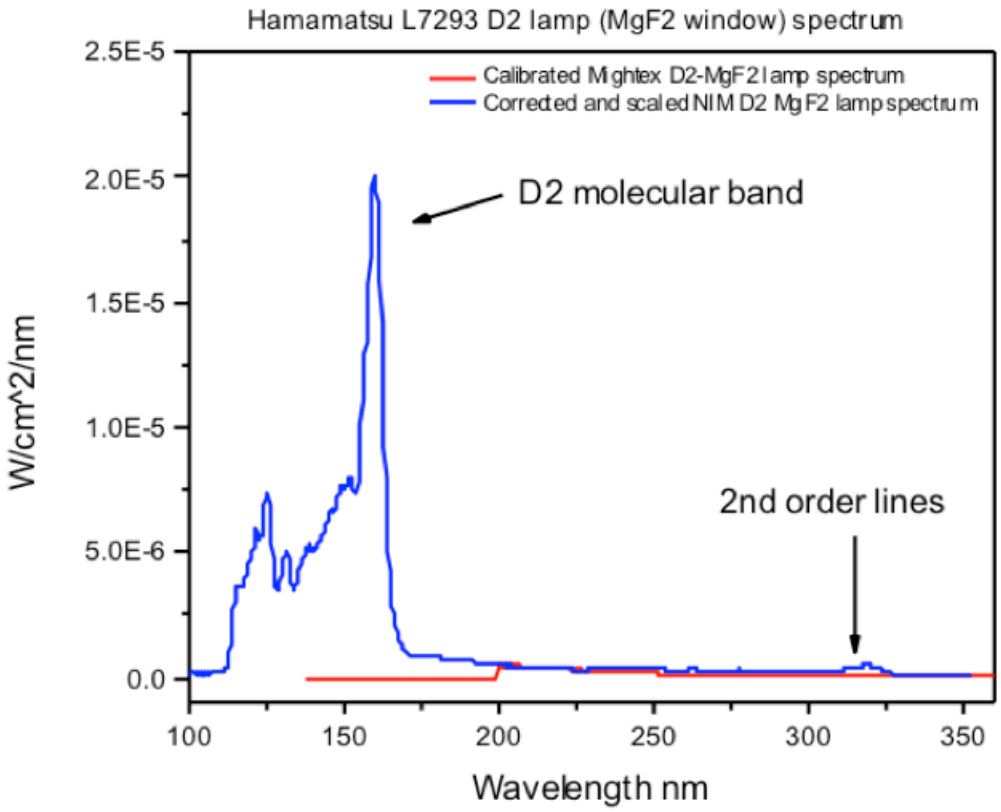

Figure 42. The overlay of the corrected L7293 D_2 lamp NIS spectrum and the calibrated Mightex spectrum over the 180-400 nm region. The intensity profiles match, and additional second order lines are observed in the corrected L7293 D_2 lamp spectrum. The second order lines were quantified to be 4.9% of the first order intensity that was not included in the output power since the light of wavelength less than 200 nm is not transparent to the window of the Mightex spectrometer.

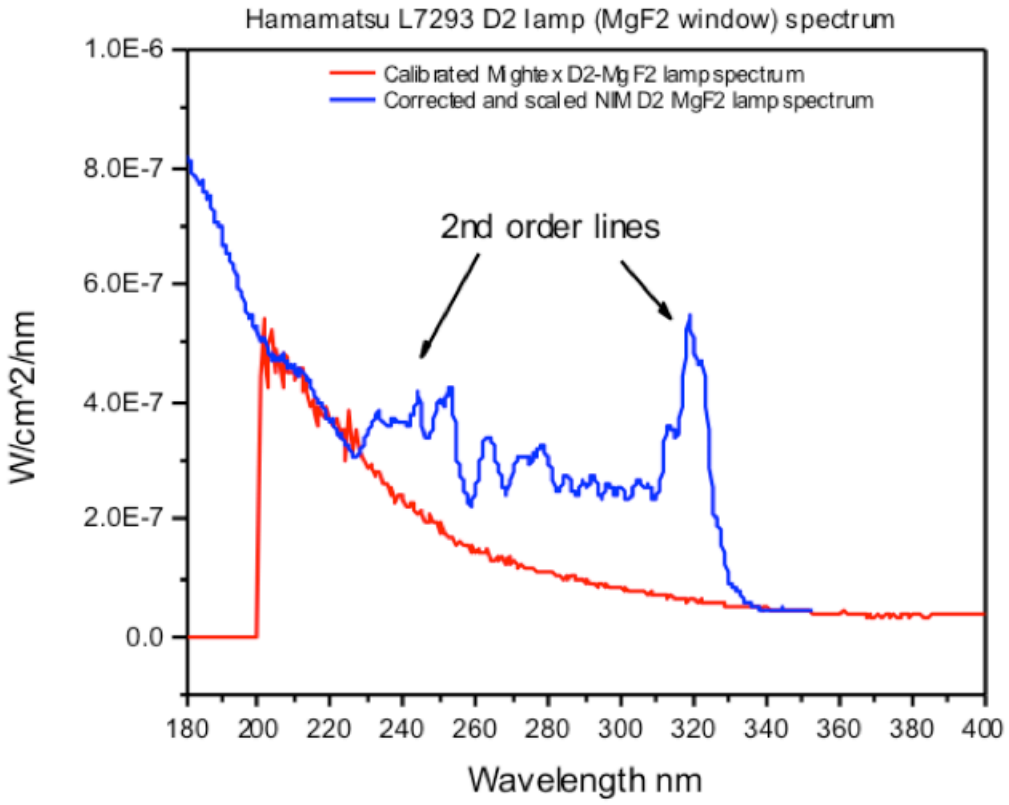

Figure 43. The overlay of the corrected L7293 D_2 lamp spectrum and the relative irradiance of the Hamamatsu L7293 D_2 lamp over the 100-400 nm region provided by Hamamatsu [15] showing a spectral match for the wavelength region greater than 155 nm.

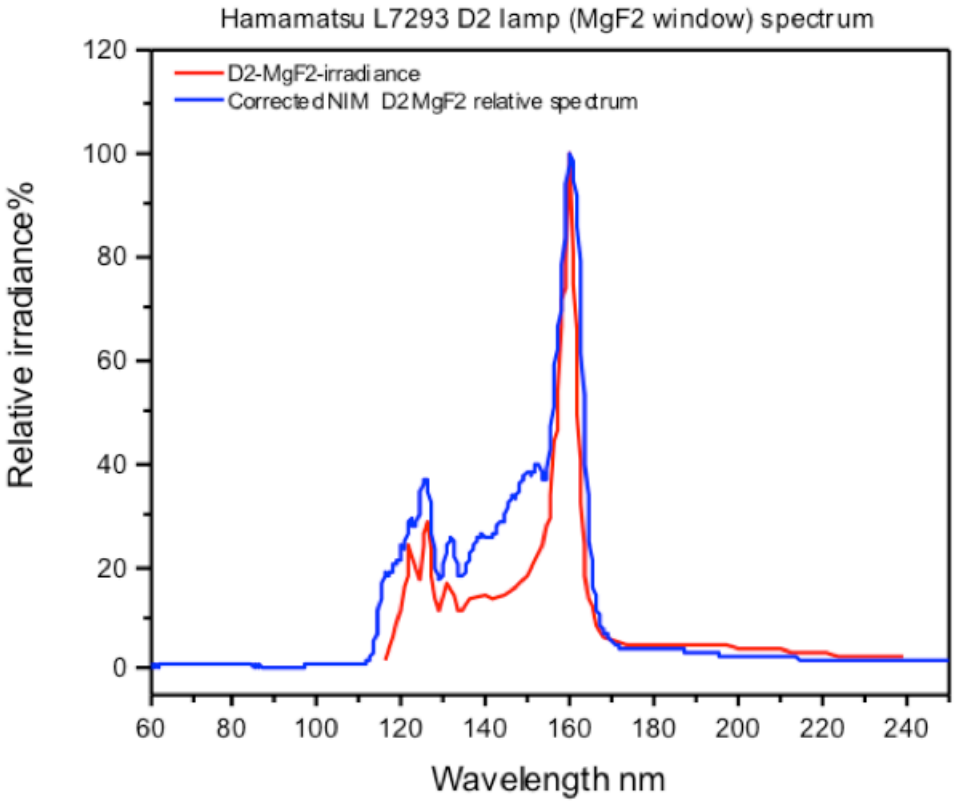

Figure 44. The overlay of the corrected L7293 D_2 lamp spectrum and the relative irradiance of a deuterium plasma over the 110-180 nm region published by Los Alamos National Laboratory [16] showing a spectral match for the wavelength region greater than 155 nm.

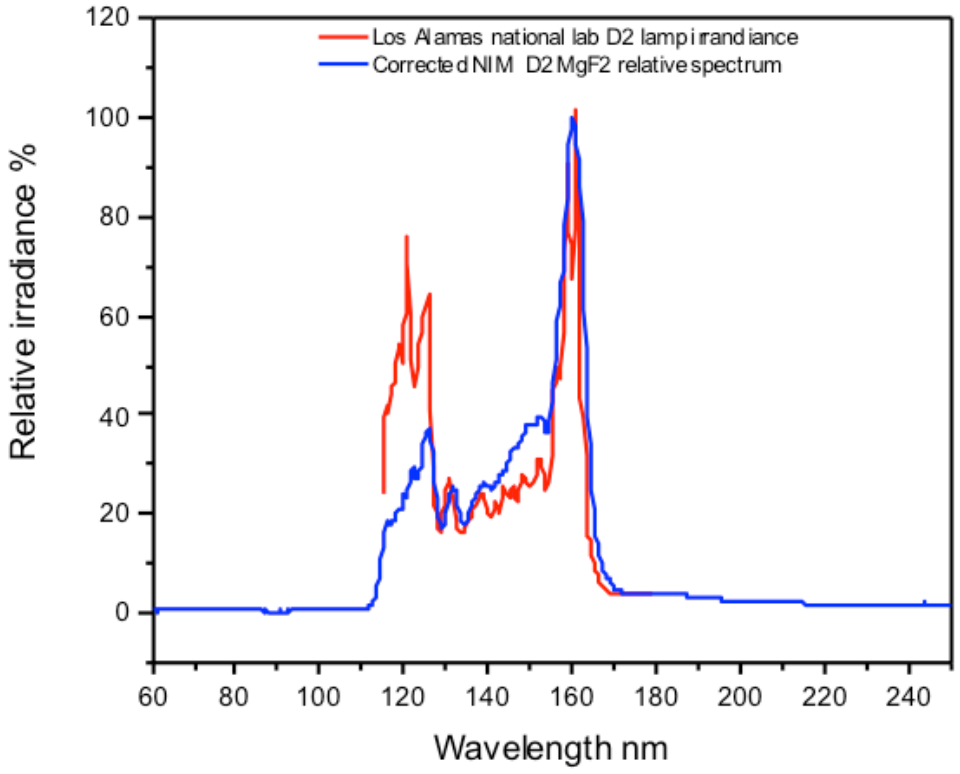

Figures 45A-B. A blast-induced electromagnetic pulse (EMP) was characterized at an independent, laboratory grounded electrode. A. The experimental setup to measure the ignition voltage and current waveforms and the EMP at an isolated electrode. B. An EMP of higher voltage than the pre-ignition voltage measured on the electrode bus bars was observed at an independent electrode placed 20 cm from the blast. The ignition current decayed exponentially indicating that the voltage pulse did not significantly affect it. EMP pulses were observed with the current at zero due to hydrino plasma afterglow.

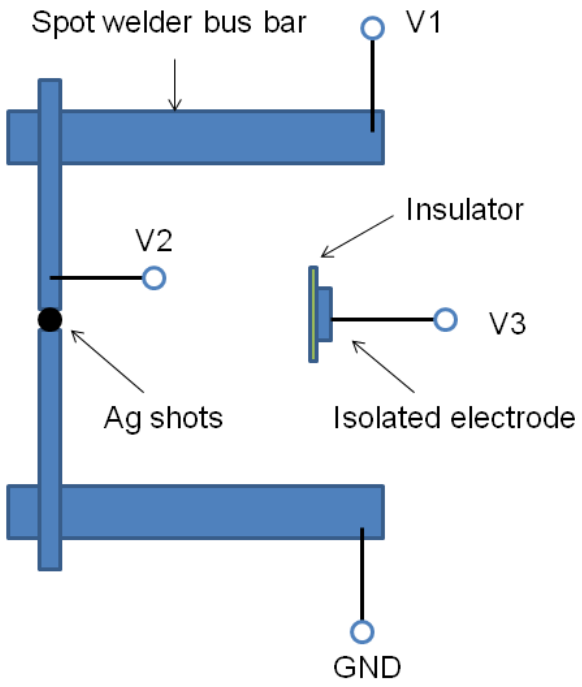

(A)

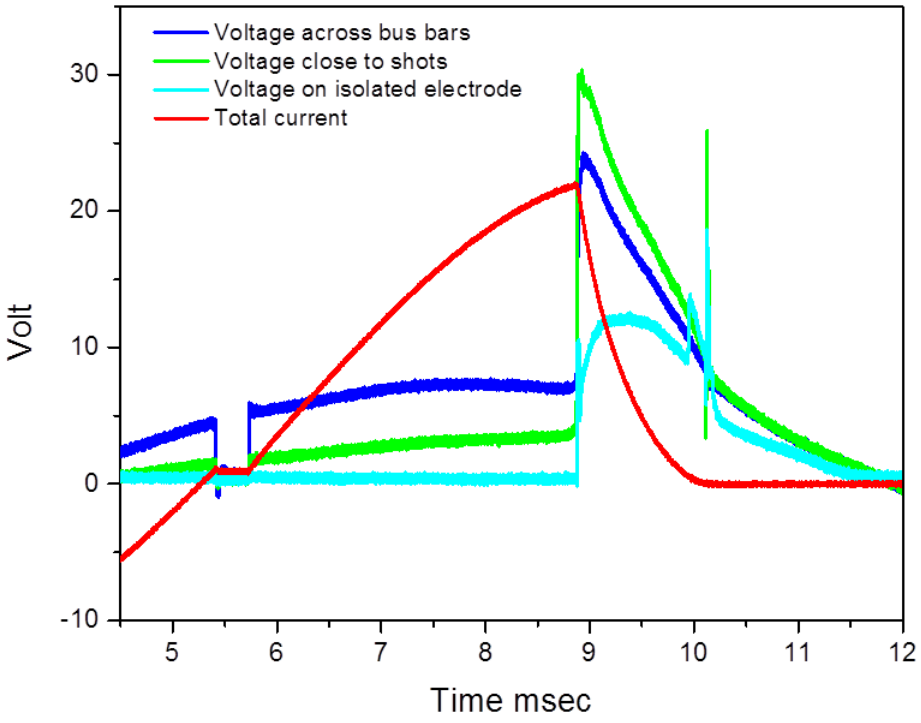
Voltage across bus bars
Voltage close to shots
Voltage on isolated electrode
Total current
Volt
Time msec
30
20
10
0
-10
5
6
7
8
9
10
11
12

(B)

Figure 46. Brilliant flashes of EUV light in the 11-18 nm EUV diode-Al filter band pass region (green trace of EUV photodiode) were observed during multiple microsecond duration EMPs when the ignition voltage (blue trace) was low and standard sinusoidal.

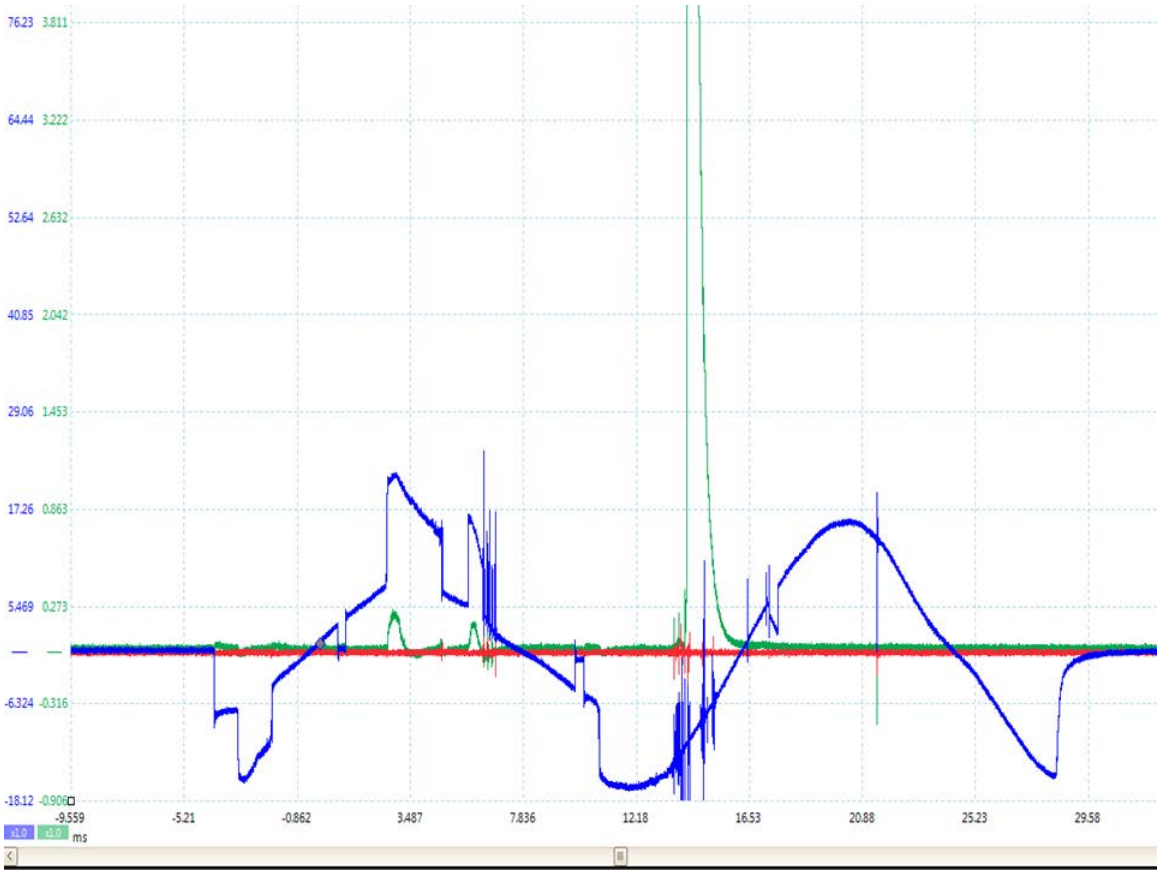

Figures 47A-E. The shot current, voltage, power, and energy determined using a standard shunt resistor. A. Rogowski coil calibration with both coils recording the same current and phase. B. The measured total bus bar current and the measured shunt current. C. The measured total bus bar current and the calculated conserved shot current of current divider circuit of the shunt and shot. D. The shunt and shot parallel voltage given by the product of the shunt current and resistance. E. The shot power given by the product of the shot voltage and shot current. The power spike was assigned to the EMP's effect on the Rogowski coil that was much less than the effect of the voltage probe. The power was integrated to give the total input energy and the energy component during the blast event when light was emitted. The total input energy from 0 ms to 9.3 ms was 66 J, and the component of the input energy during the blast event from 8.9 ms to 9.3 ms was 17 J.

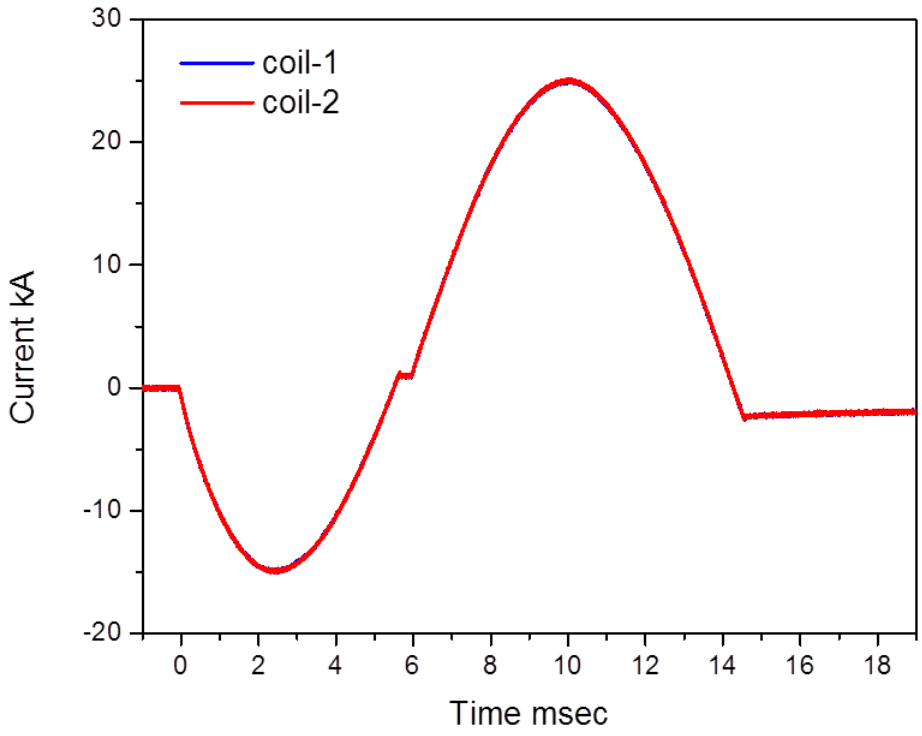

(A)

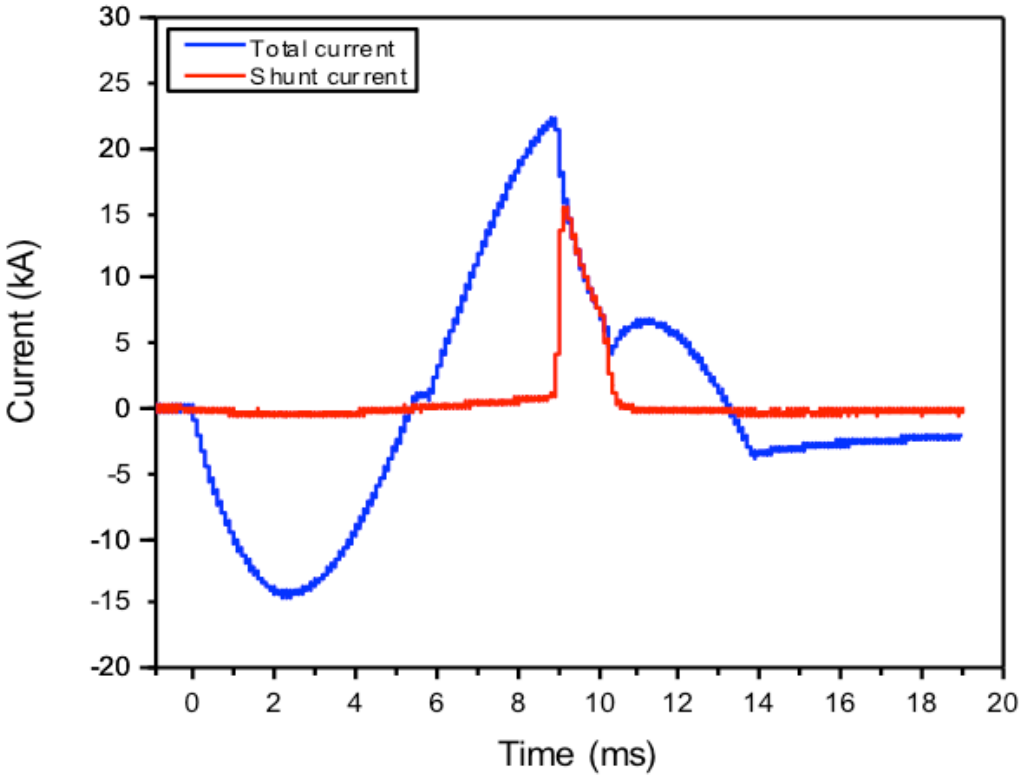
Total current
Shunt current
Current (kA)
Time (ms)
30
25
20
15
10
5
0
-5
-10
-15
-20
0
2
4
6
8
10
12
14
16
18
20

(B)

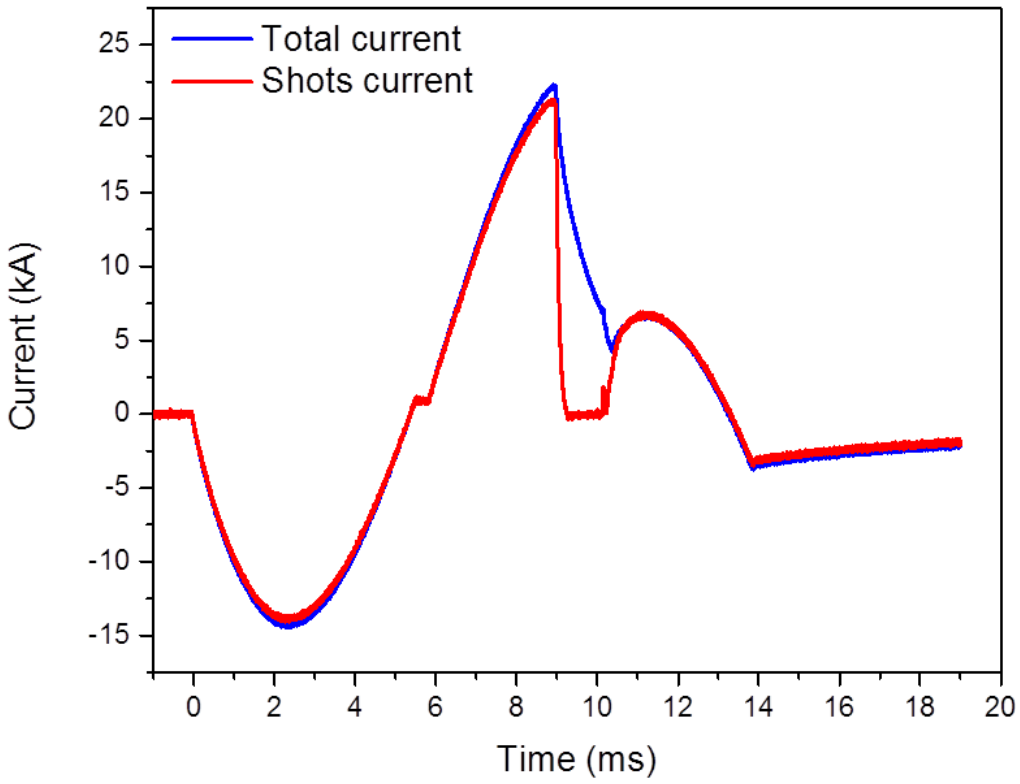
Total current
Shots current
Current (kA)
Time (ms)
25
20
15
10
5
0
-5
-10
-15
0
2
4
6
8
10
12
14
16
18
20

(C)

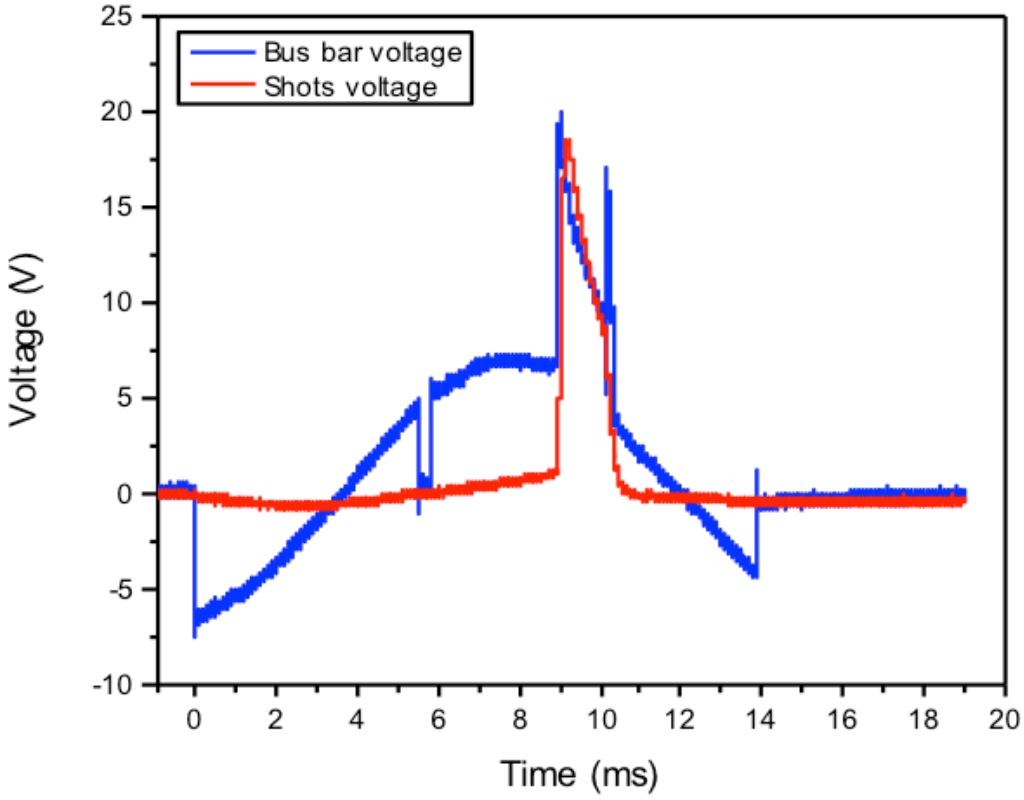
Bus bar voltage
Shots voltage
Voltage (V)
Time (ms)
25
20
15
10
5
0
-5
-10
0
2
4
6
8
10
12
14
16
18
20

(D)

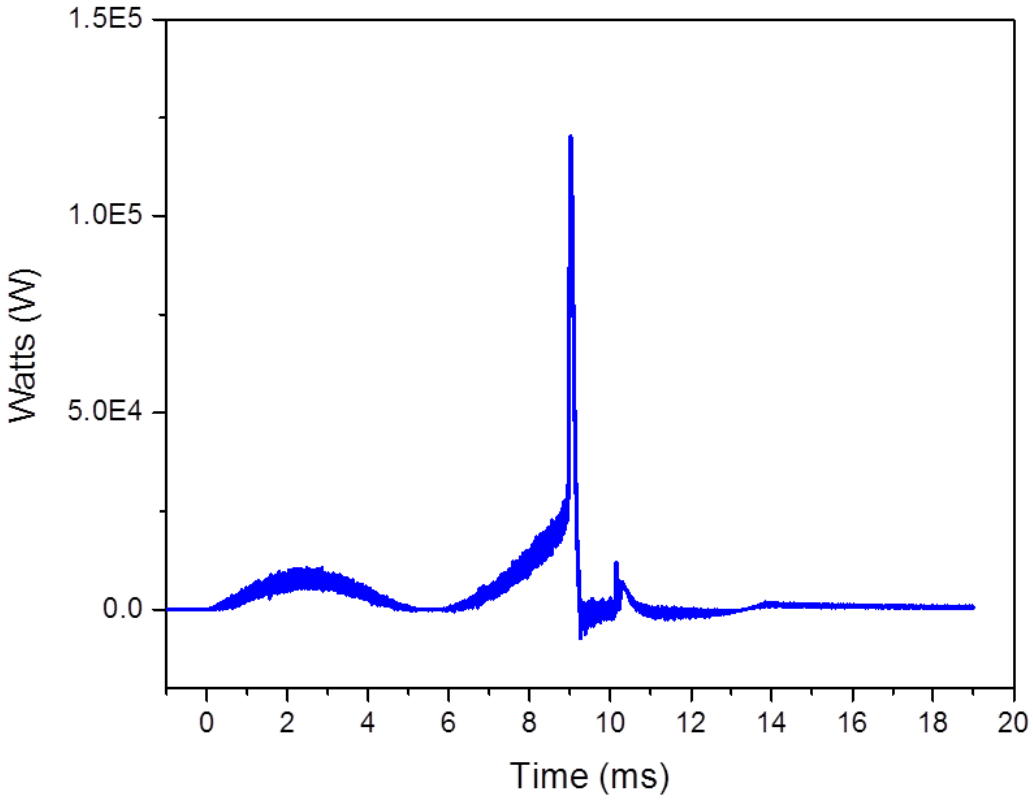

(E)

Figures 48A-C. Visible spectra in the spectral region of the H Balmer α line to determine the Stark broadening. A. The full width half maximum (FWHM) of the 632.8 nm HeNe laser line recorded on the Ocean Optics spectrometer was 12.9 Å. B. The full width half maximum (FWHM) of the 632.8 nm HeNe laser line was 0.37 Å that confirmed the high spectral resolution of the Jobin Yvon Horiba 1250 M spectrometer with a 20 μm slit. C. The FWHM of the Balmer α line from the emission of an ignited shot by the Ocean Optics spectrometer was 22.9 Å corresponding to an electron density of 4 X $10^{23}/m^3$. During a phase of the event, the plasma was almost completely ionized. D. The FWHM of the Balmer α line from the emission of an ignited shot by the Jobin Yvon Horiba 1250 M spectrometer with a 20 μm slit was 15 Å confirming the extraordinary broadening. The line was shifted by +1.2 Å.

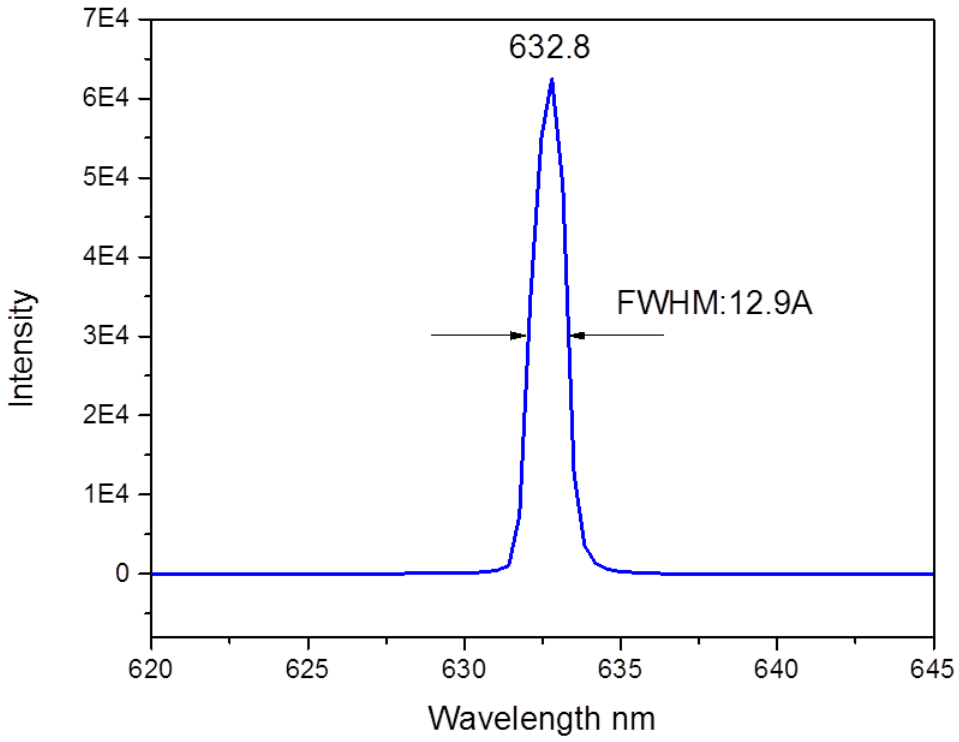

(A)

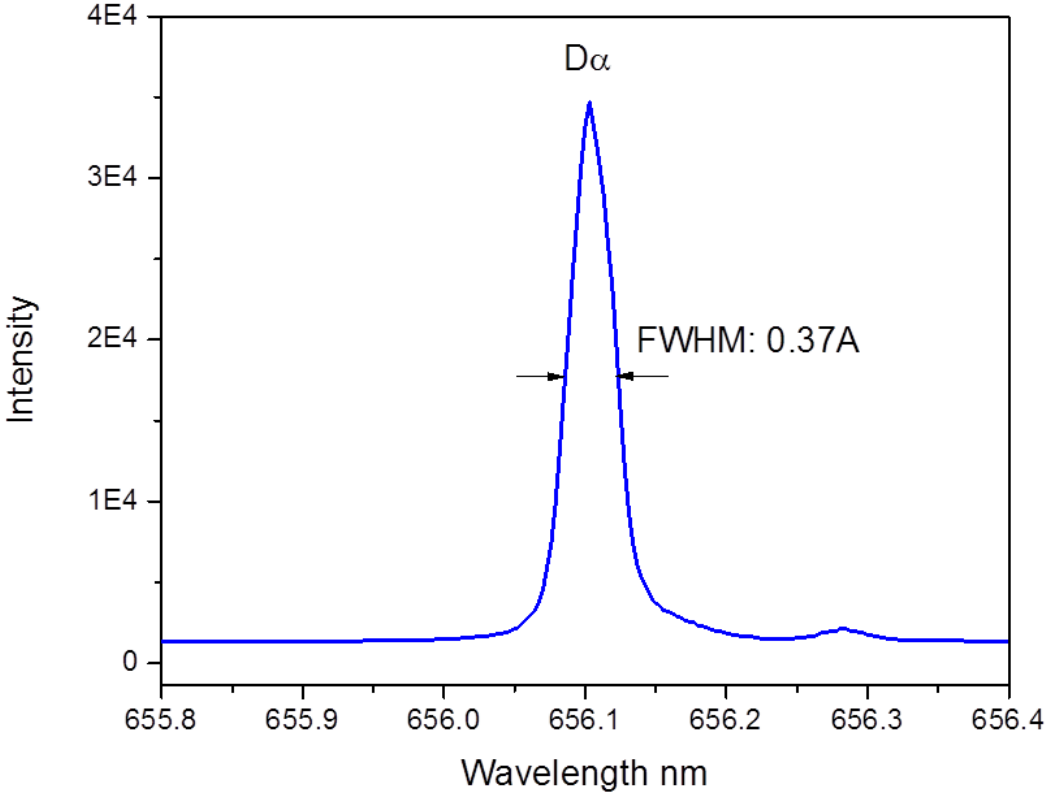
4E4
3E4
2E4
1E4
0
Intensity
Dα
FWHM: 0.37A
655.8
655.9
656.0
656.1
656.2
656.3
656.4
Wavelength nm

(B)

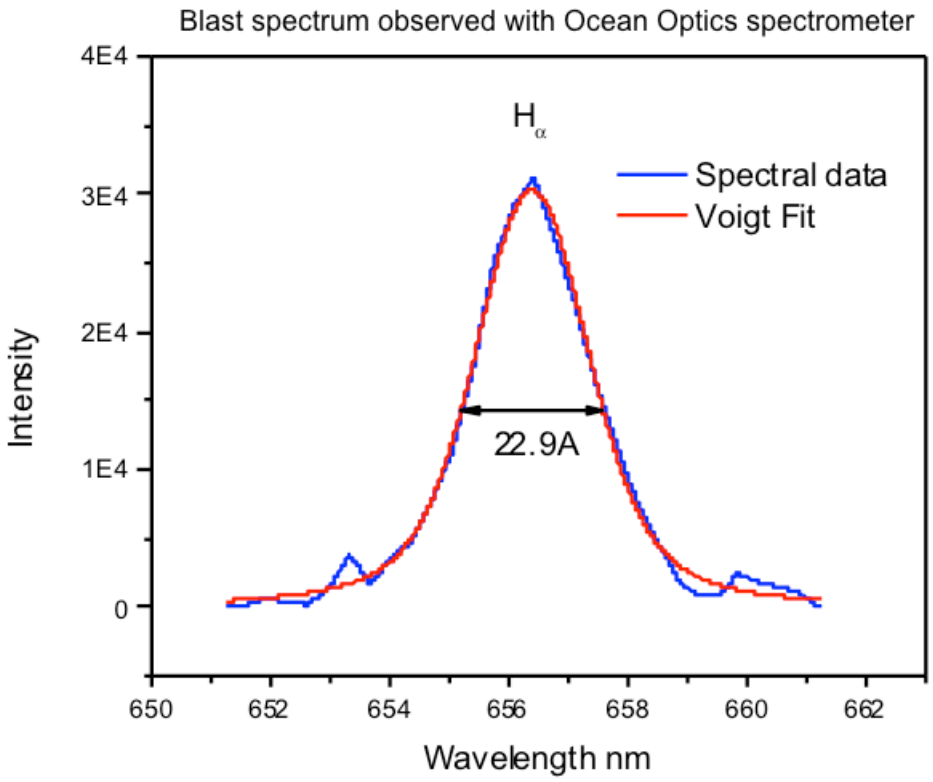
Blast spectrum observed with Ocean Optics spectrometer
4E4
3E4
2E4
1E4
0
Intensity
650
652
654
656
658
660
662
Wavelength nm
H_α
Spectral data
Voigt Fit
22.9A

(C)

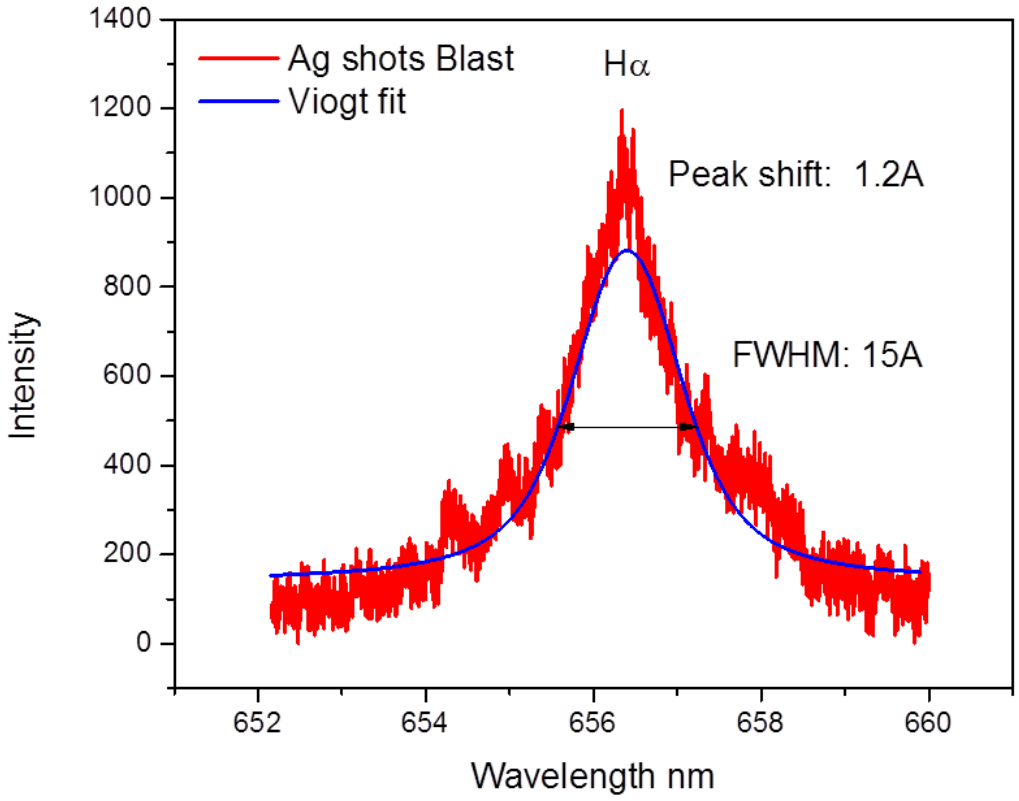
Ag shots Blast
Viogt fit
Hα
Peak shift: 1.2A
FWHM: 15A
Intensity
Wavelength nm
1400
1200
1000
800
600
400
200
0
652
654
656
658
660

(D)

Figure 49. VI waveform with superposition of time-sequenced high-speed (17,791 frames per second) video frames from the recording of brilliant light-emitting expanding plasma formed from the low voltage, high current detonation of a 70 mg hydrated silver shot. Plasma persisted at a time when there was no electrical input power (noted by the zero current (red) trace), and no chemical reaction was possible. The plasma persisted for 4 ms while the input power was zero at 0.8 ms. An electromagnetic pulse (EMP) was observed at the initiation of the blast that did not contribute to the power input to the shot as indicated by the exponential current decay.

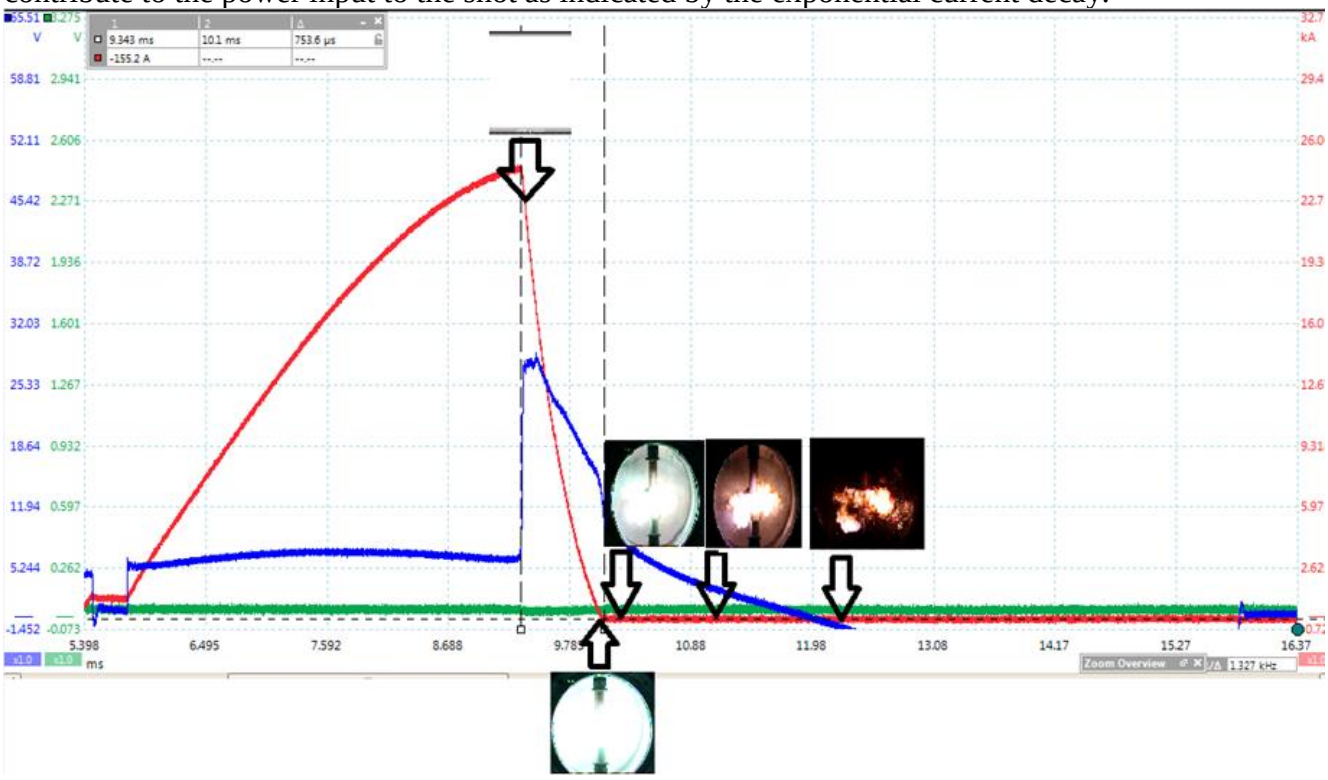

Figure 50. The EUV emission of the plasma produced in a vacuum chamber by continuous injection of molten silver recorded by the normal incidence EUV spectrometer with a superposition of the spectrum recorded on the hydrated silver shot. The comparison indicates that the UV spectral emission of the molten silver injection matches that of the single shots.

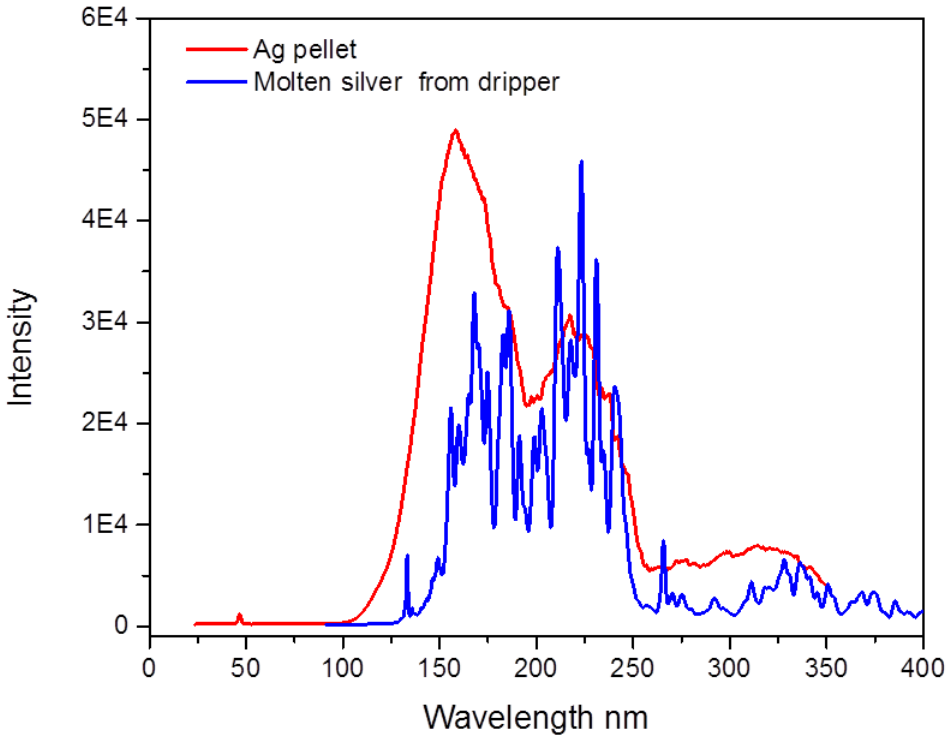

Figures 51A-C. Video frames of the time evolution of the plasma produced by continuous injection of molten silver recorded by the Edgertronic high-speed camera. The optically thick plasma emission at peak power is that of a 5700K blackbody. A. Initial emission. B. Emission at 217 ms. C. Emission at 375 ms.

(A)

(B)

(C)

Figures 52A-B. The time evolution of the UV-Visible emission of two runs of the plasma produced by continuous injection of molten silver recorded by the Mightex spectrometer. The optically thick plasma emission at peak power is that of a 5700K blackbody. A. T1 is at 0.7725 ms. B. T1 is at 0.7341 ms.

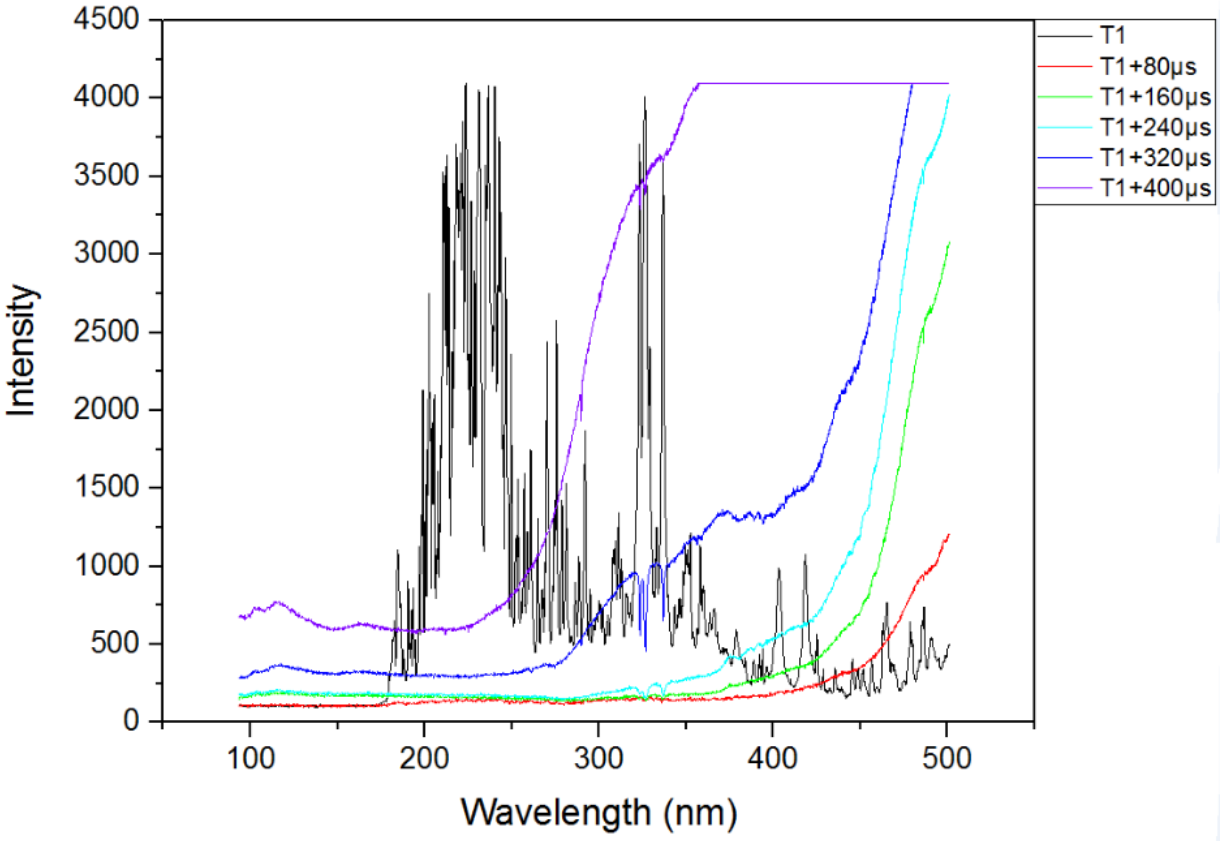

(A)

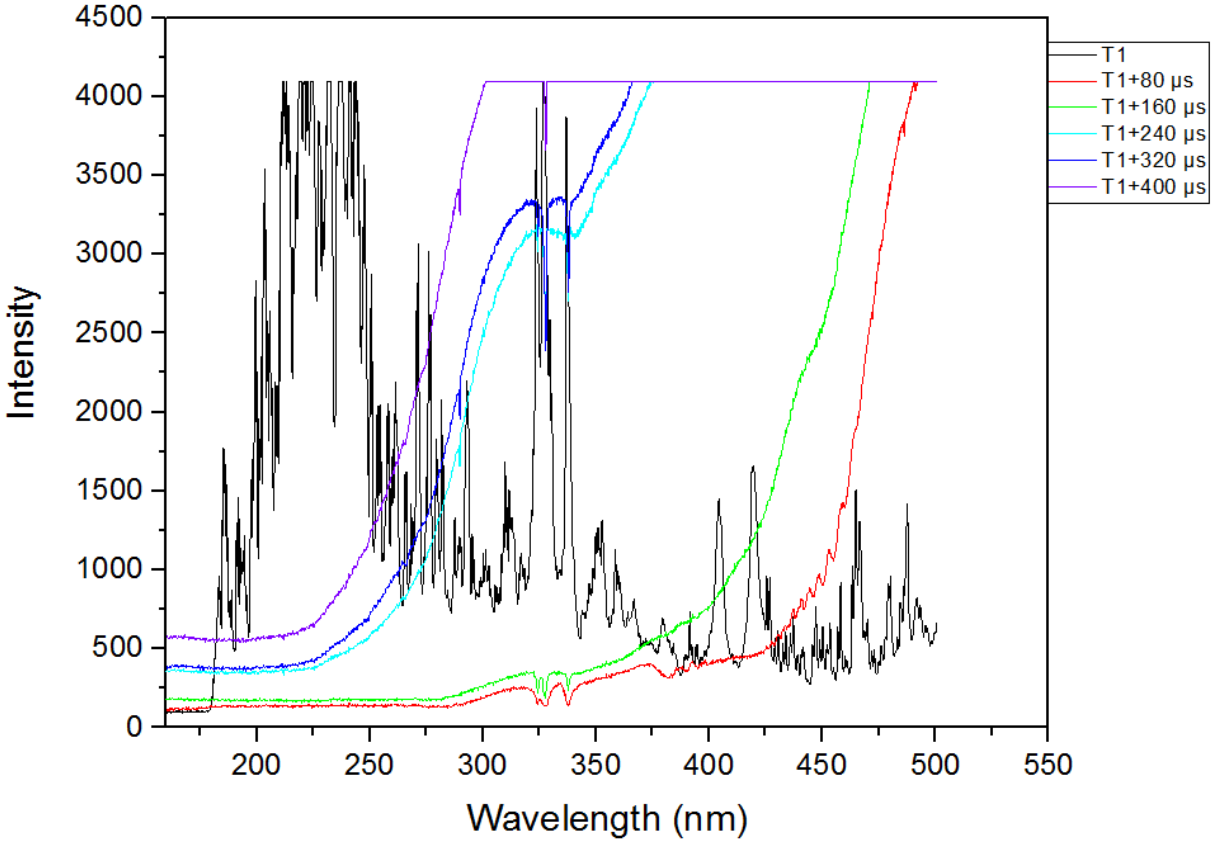
Intensity
Wavelength (nm)
T1
T1+80 µs
T1+160 µs
T1+240 µs
T1+320 µs
T1+400 µs

(B)

Figure 53. The shot power determined using a standard shunt resistor and two Rogowski coils to measure the total and shunt currents. The shot power was given by the product of the shot voltage and shot current. The power was integrated to give the total input energy. The total input energy from 0 ms to 9.53 ms was 109.6 J, and the component of the input energy during the blast event from 9.25 ms to 9.53 ms was 21.4 J.

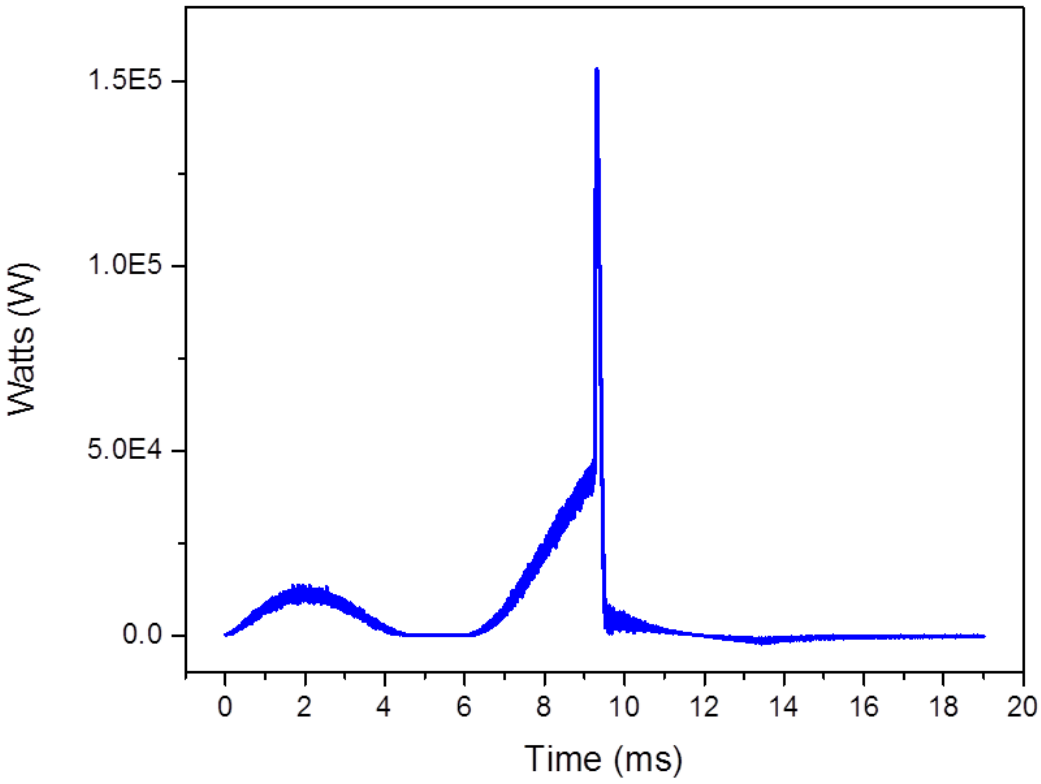

Figure 54. Welder trigger and pressure sensor data for sample hydrated silver shot (70 mg/6.5 X 10^{-4} moles Ag + 6.5 X 10^{-5} moles H_2O) as a function of time showing the detonation shockwave that is faster than sound speed. A later reflected peak is also observed. The spot welder power output peak was used as the start time of the shockwave. The shockwave speed was 384 m/s and the corresponding overpressure was 0.25 PSI.

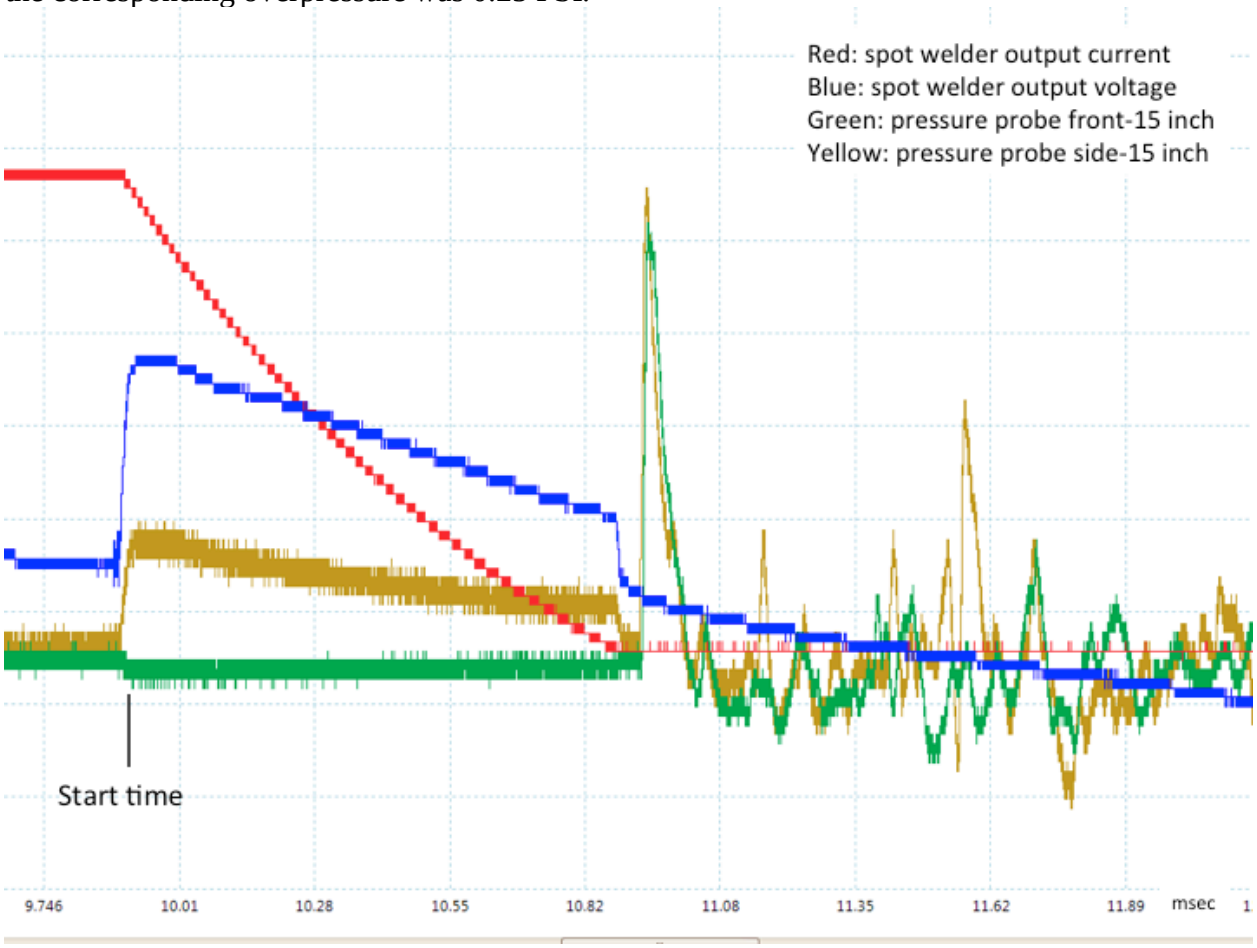

Figure 55. Welder trigger and pressure sensor data for sample Ti powder (15 mg/3.1 X 10^{-4} moles) + H_2O (5 mg/2.8 X 10^{-4} moles) in the Al DSC pan as a function of time showing the detonation shockwave that is faster than sound speed. A later reflected peak is also observed. The EMP spike was used as the start time of the shockwave. The shockwave speed was 400 m/s and the corresponding overpressure was 0.45 PSI.

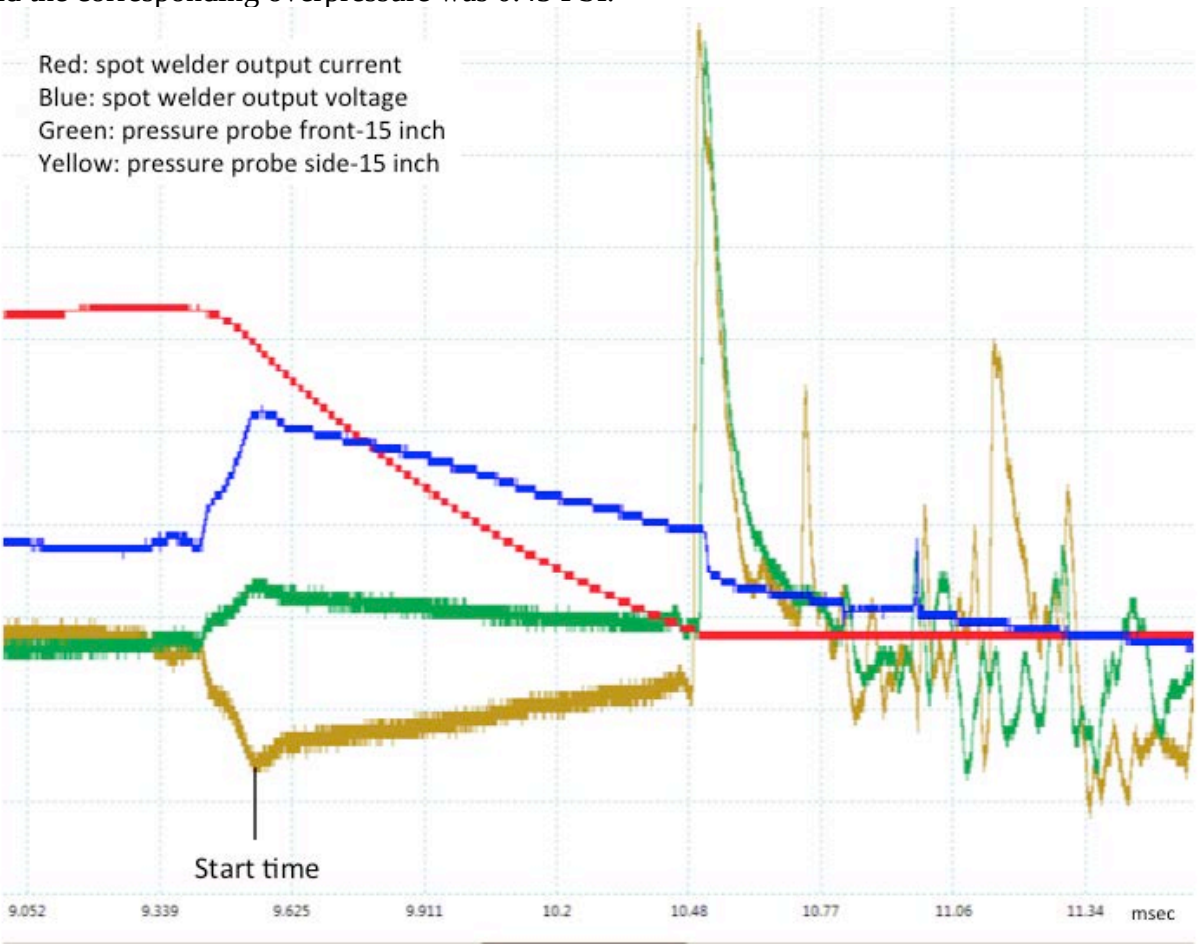

Figure 56. Welder trigger and pressure sensor data for sample Ti powder (83 mg/1.7 X 10^{-3} moles) + H_2O (30 mg/1.7 X 10^{-3} moles) in the Al DSC pan as a function of time showing the detonation shockwave that is faster than sound speed. A later reflected peak is also observed. The EMP spike was used as the start time of the shockwave. The shockwave speed was 422 m/s and the corresponding overpressure was 1.09 PSI.

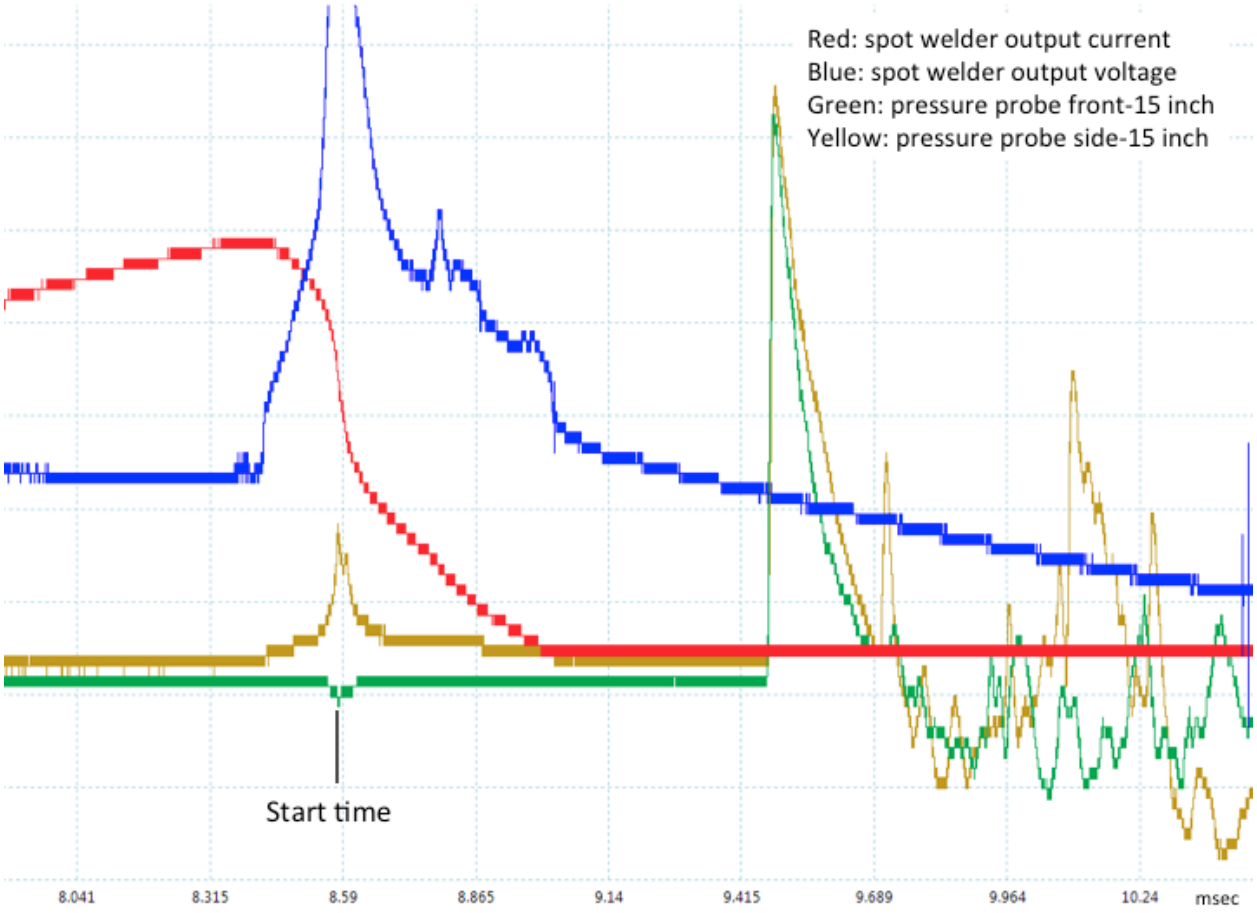

Figure 57. Welder trigger and pressure sensor data for sample gunpowder (47 mg/0.563 X 10^{-3} moles) in the Al DSC pan as a function of time showing the detonation shockwave that is faster than sound speed. A later reflected peak is also observed. The spot welder power output peak was used as the start time of the shockwave. The shockwave speed was 398 m/s and the corresponding overpressure was 0.43 PSI.

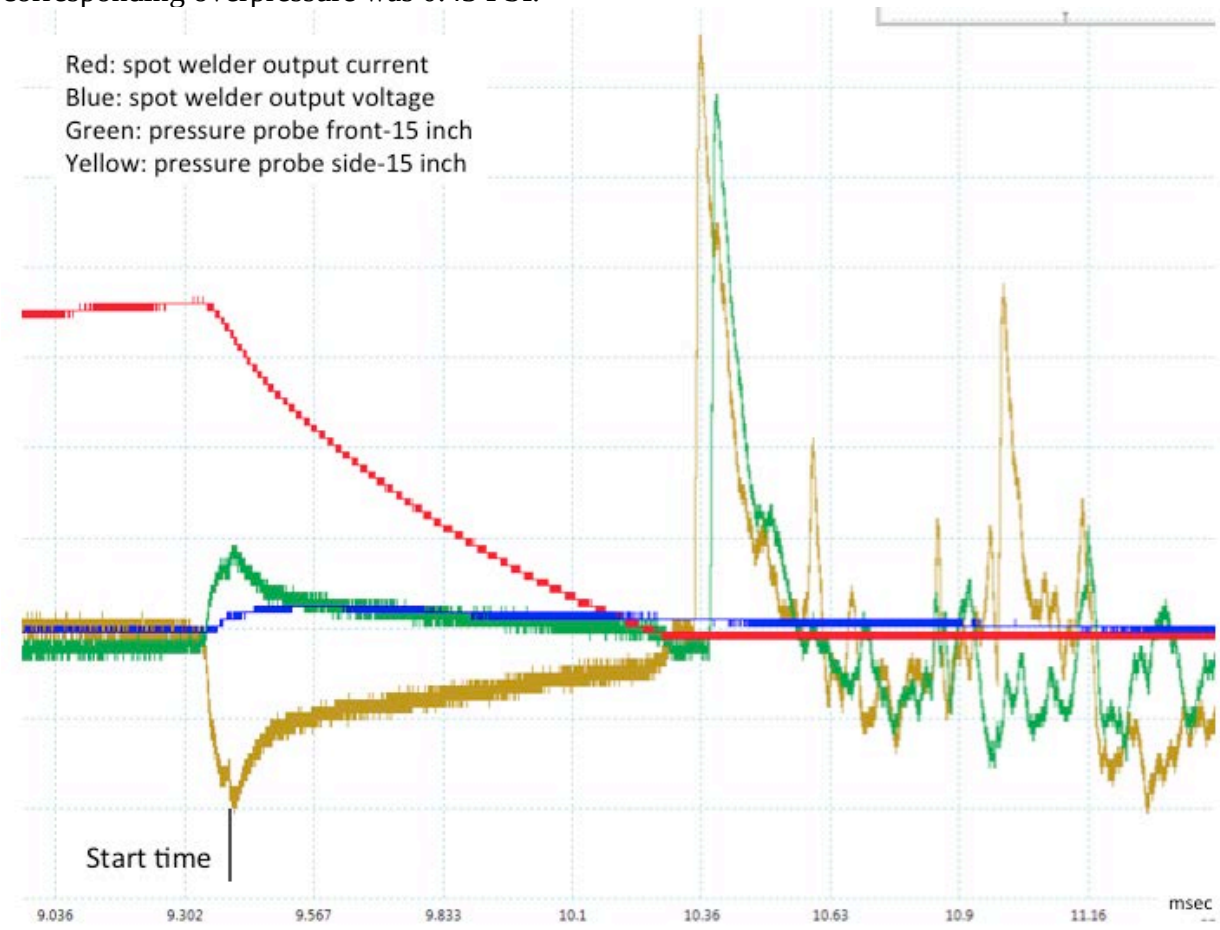

Figure 58. Welder trigger and pressure sensor data for sample NH_4NO_3 (58 mg/7.25 X 10^{-4} moles) in the Al DSC pan as a function of time showing the detonation shockwave that is faster than sound speed. A later reflected peak is also observed. The spot welder power output peak was used as the start time of the shockwave. The shockwave speed was 390 m/s and the corresponding overpressure was 0.44 PSI.

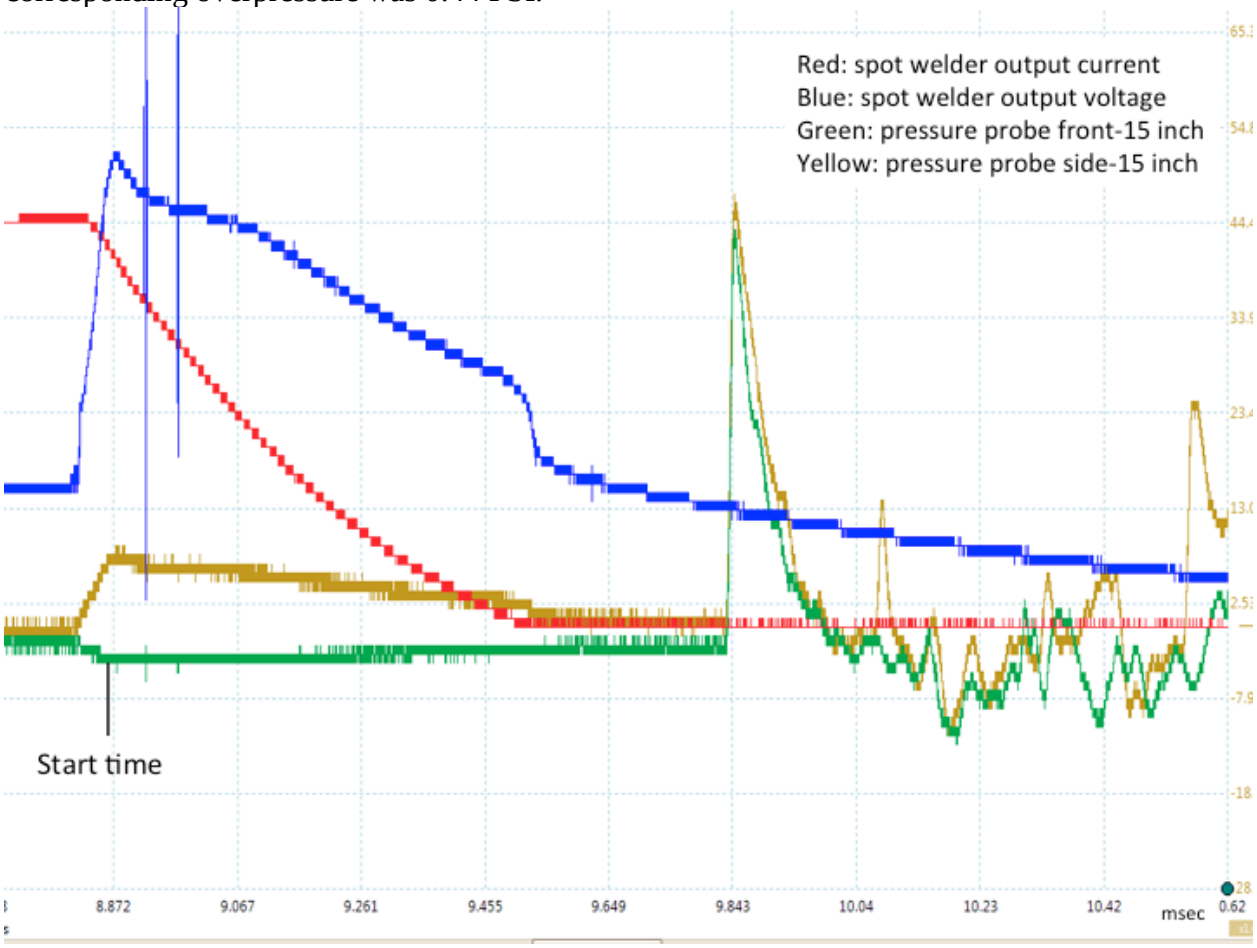

Figure 59. The Raman spectrum obtained on In metal foil exposed to the hydrino product gas. Using the Thermo Scientific DXR SmartRaman spectrometer and the 780 nm laser, the spectrum showed an inverse Raman effect peak at 1982 cm^{-1} that matches the free rotor energy of $H_2(1/4)$ (0.2414 eV) to four significant figures.

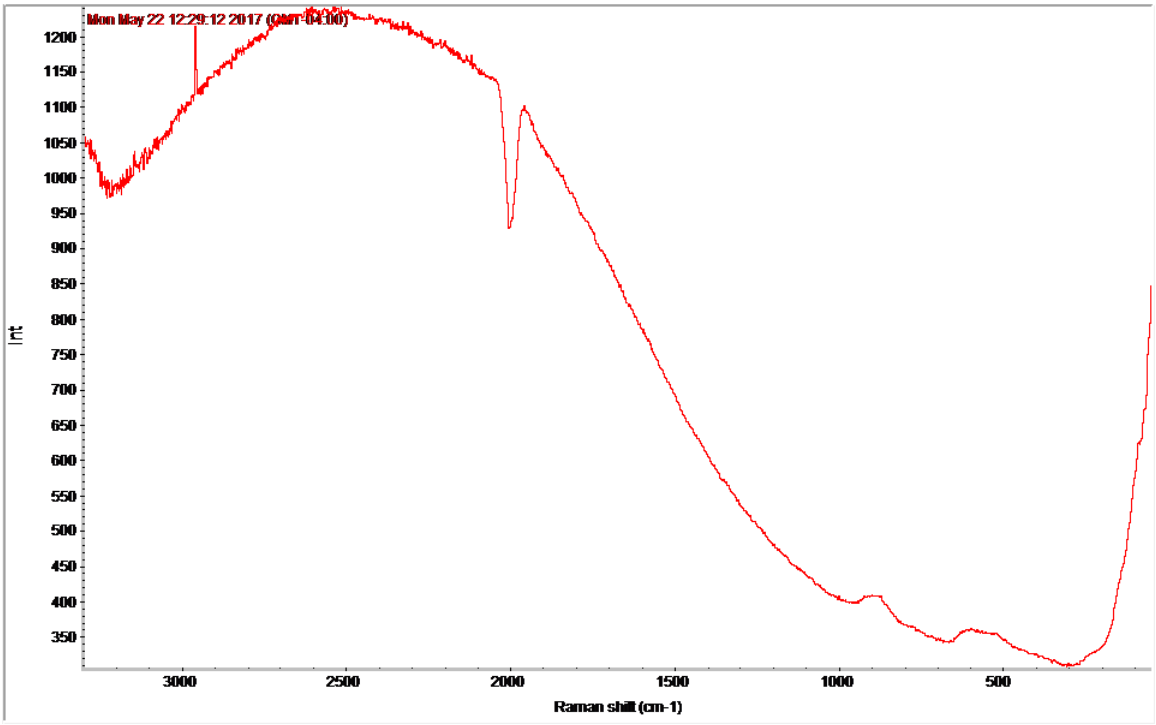

Figure 60. Raman-mode second-order photoluminescence spectrum of the NaOH-KCl (1:1 wt%) getter exposed to the hydrino product gases using a Horiba Jobin Yvon LabRam ARAMIS 325nm laser with a 1200 grating over a range of 8000-19,000 cm^{-1} Raman shift.

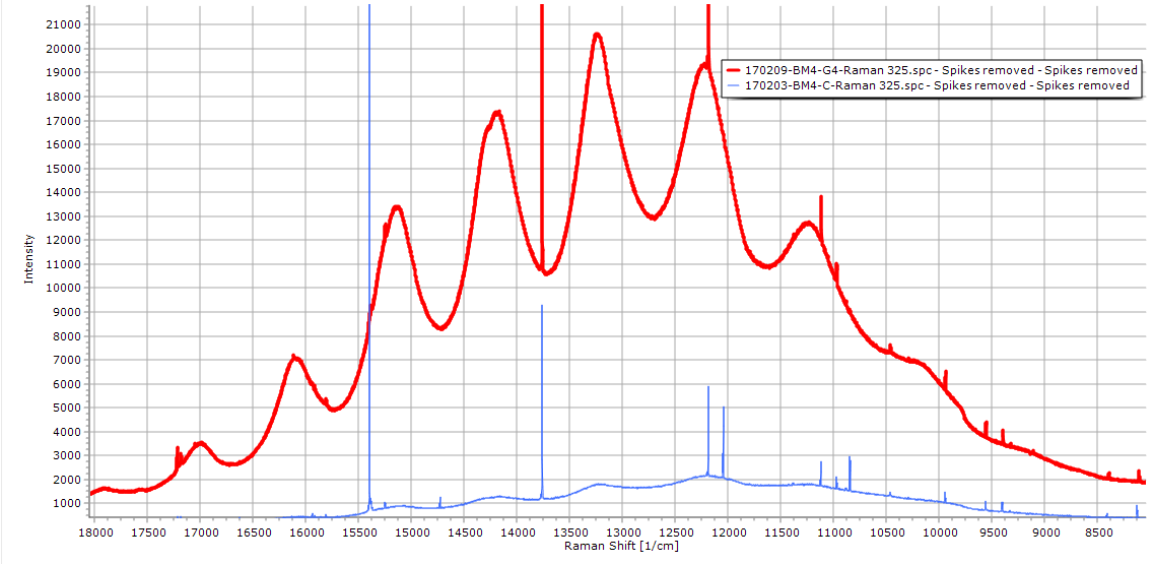

Figure 61. A plot comparison between the theoretical energies and assignments given in Table 4 with the observed Raman spectrum.

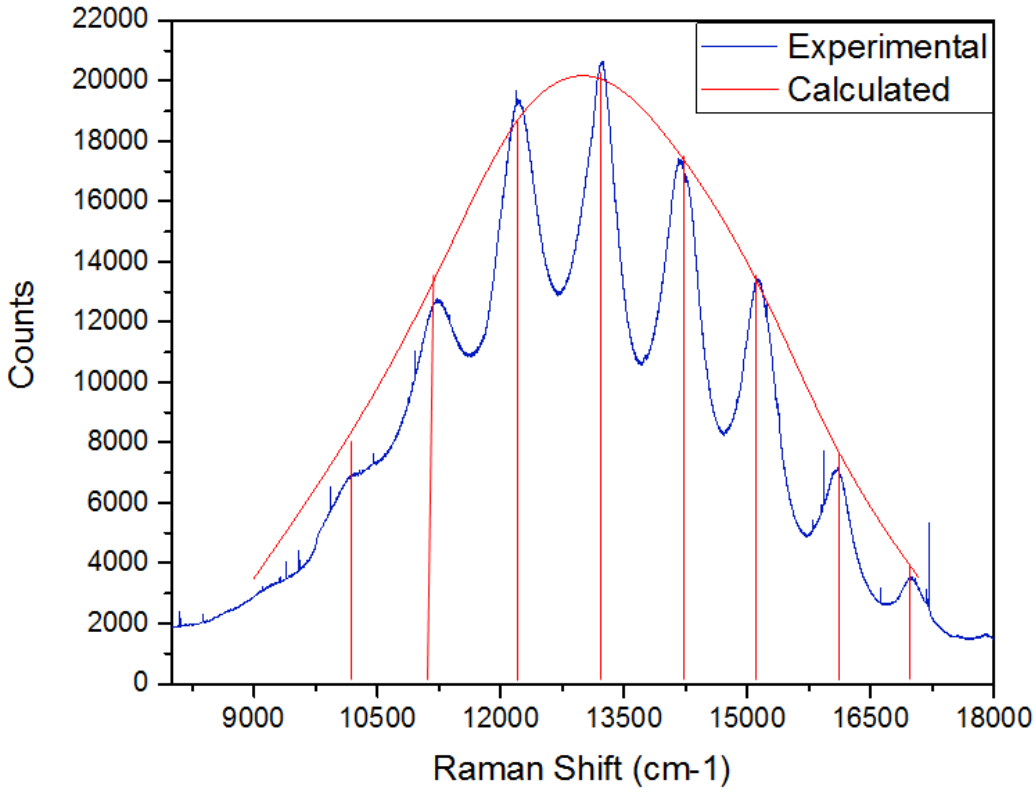

Figure 62. XPS spectra recorded on the indium metal foil exposed to hydrino product gas. A. A survey spectrum showing only the elements In, C, and O peaks were present. B. High-resolution spectrum showing a peak at 498.5 eV assigned to $H_2(1/4)$ wherein other possibilities were eliminated based on the absence of any other corresponding primary element peaks.

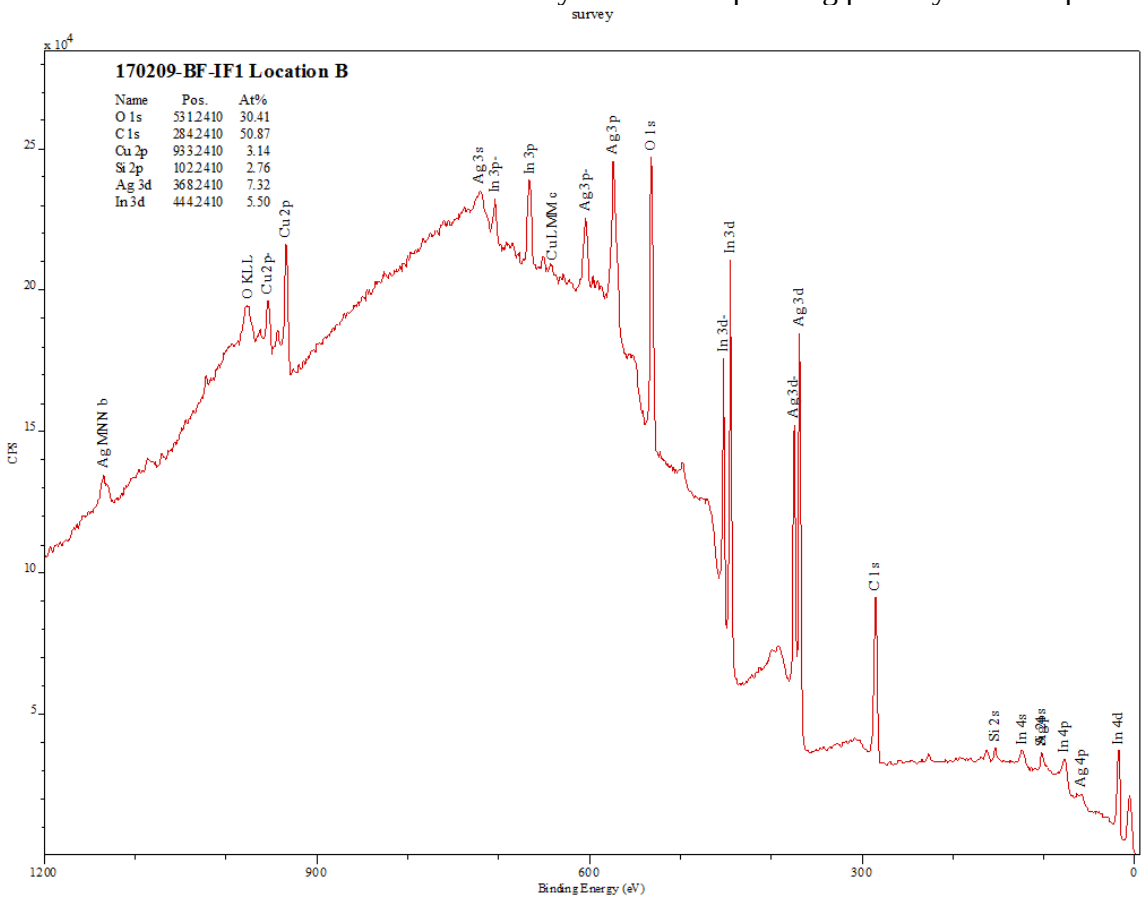

(A)

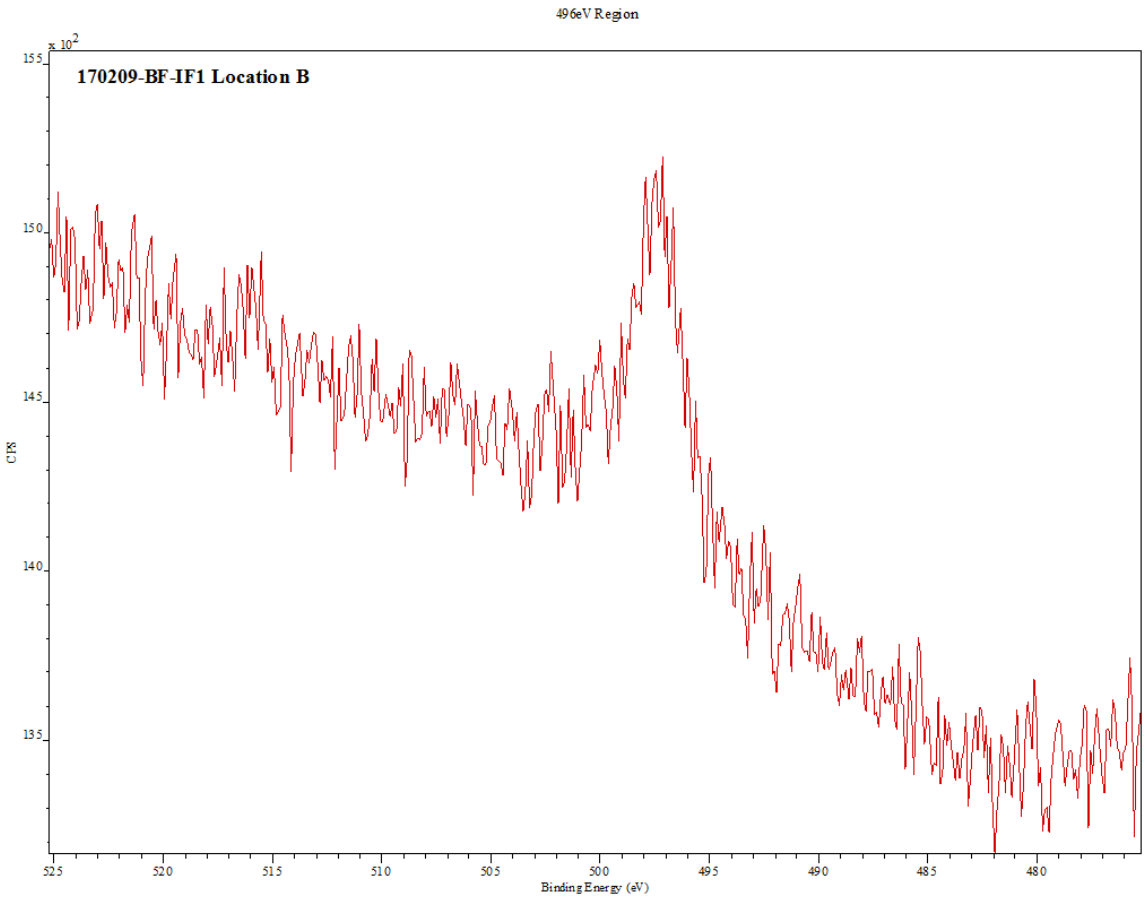
496eV Region
x 10^2
170209-BF-IF1 Location B
155
150
145
140
135
CPS
525
520
515
510
505
500
495
490
485
480
Binding Energy (eV)

(B)

Figure 63. MAS NMR spectrum relative to external TMS of the carbon getter exposed to gases from the ignition of silver shot that shows upfield shifted matrix peaks -7.7 ppm. The small symmetrically spaced peaks are spinning side bands.